# Stony Brook University

# Studies of Decoherence in rf SQUID Qubits

A Dissertation Presented

by

**Douglas A. Bennett**

to

The Graduate School

in Partial Fulfillment of the Requirements

for the Degree of

**Doctor of Philosophy**

in

**Physics**

Stony Brook University

December 2007

**Stony Brook University**

The Graduate School

## Douglas A. Bennett

We, the dissertation committee for the above candidate for the Doctor of Philosophy degree, hereby recommend acceptance of this dissertation.

Dr. James E. Lukens – Dissertation Advisor
Professor, Department of Physics and Astronomy

Dr. Konstantin K. Likharev – Chairperson of Defense
Distinguished Professor, Department of Physics and Astronomy

Dr. Thomas C. Weinacht
Assistant Professor, Department of Physics and Astronomy

Dr. Serge Luryi
Distinguished Professor
Department of Electrical & Computer Engineering

This dissertation is accepted by the Graduate School.

Lawrence Martin
Dean of the Graduate School

Abstract of the Dissertation

# Studies of Decoherence in rf SQUID Qubits

by

**Douglas A. Bennett**

**Doctor of Philosophy**

in

**Physics**

Stony Brook University

2007

Usually quantum mechanical behavior is associated with single elementary particles or a moderate size group of these particles such as atoms or molecules. However a distinctly macroscopic object such as a rf SQUID is capable of uniquely quantum mechanical behavior if it is sufficiently decoupled from its environment. A rf SQUID consists of a superconducting loop interrupted by thin insulating barrier, known as a Josephson junction. When the loop is externally biased with half a flux quantum, the potential energy forms a double well potential as function of the total flux, with the two wells representing circulating currents in opposite directions consisting of $10^9$ Cooper pairs. At low temperatures and for suitable junction parameters this system behaves quantum mechanically with a Hamiltonian analogous to a particle in this potential. The eigenstates of the system are ideal for tests of quantum mechanics on a macroscopic level and can be used as basis states for quantum computation.

These devices are realized using $Nb/AlO_x/Nb$ junctions that are patterned using electron beam lithography. The experimental setup

was carefully designed to reduce coupling of external noise sources to the rf SQUID. The setup was extensively tested to confirm that the external environment is not the dominant source of decoherence. Careful measurement of the system parameters allowed for the accurate calculations necessary to compare the measurements with theory. Coherent oscillations were observed between the ground and excited states within the same fluxoid state of the rf SQUID using pulsed microwaves to couple the states. The decay of these oscillations along with microwave spectroscopy and direct measurement of the lifetime of the excited state were used to characterize the source or sources of decoherence. There exists low frequency flux noise and a short lifetime for the excited state that are not consistent with known noise sources.

# Contents

# List of Figures

# List of Tables

# Acknowledgements

I would like to thank the many people who have helped me in many ways over many years. I have been extremely lucky in my colleagues and friends. Any undertaking of this magnitude must necessarily rely on the effort of many others. I would like to acknowledge my adviser Jim Lukens and thank him for his patience and encouragement. I would have been lost without his guidance and experience. I would also like to acknowledge Kostya Likharev and Dima Averin for their insight and theoretical support. I would like to thank TJ Walls for his help in many programming tasks. I would like to thank Shawn Pottorf, Pete Davis, Loraine Davis and Pernille Jensen for their assistance and support. This work would not be possible without Vijay Patel and Wei Chen who fabricated the samples and filters and contributed to the measurements and interpretation of the results. Finally I would like to acknowledge and thank Luigi Longobardi and Jaan Mannik for their immeasurable assistance in the measurements and analysis.

# Chapter 1

# Introduction and Background

## 1.1 Introduction

Quantum mechanics is weird! More specifically quantum mechanics is counter-intuitive (wave particle duality and spooky action at a distance) and at times unsatisfying (probabilistic). However, the unsatisfying aspects were historically restricted to particles and atoms. In other words, the quantum weirdness was only evident on a very small scale. On a macroscopic scale, a scale we feel we understand, the quantum nature of objects is obscured through coupling to everything else (the universe). However, there are systems where the quantum mechanical nature of things should be observable on a macroscopic scale. The rf SQUID (radio frequency superconducting quantum interference device), properly isolated from its environment, is an example of one such system. The discovery of quantum computing transforms the prospect of the "quantumness" of a rf SQUID from that of a scientifically interesting phenomenon to an immediately practical issue of potentially faster computation. This thesis details the experimental observation of quantum coherence in a large inductance rf SQUID and examines the mechanisms of the loss of its quantum coherence.

Quantum computing has dramatically increased the interest in the rf SQUID and other similar superconducting devices. In light of this motivation, this introduction will begin with a brief introduction to quantum computing. This is followed by a description of an rf SQUID with an emphasis on its quantum mechanical behavior and potential as a qubit. The last section of this chapter will briefly discuss a general theory for quantum two levels systems to introduce terminology and explain the general techniques that will be used to measure the quantum coherence of the rf SQUID.

The remainder of the thesis will focus on the various measurements. The

rf SQUID must be carefully isolated in order to observe quantum coherence. Chapter 2 details the design and setup that allows the necessary degree of isolation. Chapter 3 explains the various measurements that were used to determine the system parameters in order to fully characterize the Hamiltonian of the rf SQUID. Chapter 4 demonstrates the quantum nature of the rf SQUID and describes the measurements of the relevant decoherence times. Chapter 5 tries to put the measurements and analysis of Chapter 4 into context for the purpose of better understanding the causes of decoherence and improving future rf SQUID qubit designs. Finally, the appendices give details on specially designed filters and magnetometers that were used in these experiments along with concurrent studies of some of the materials and fabrication techniques that are used to realize the samples.

## 1.2 Quantum Computing

The basis for classical computation is the classical bit. Mathematically the bit has only two possible states, usually represented as 0 and 1. In classical computers, a bit is usually represented as high and low voltage states at the terminal of a transistor that behaves differently for the different states. Modern computers have developed rapidly based on improvements in the fabrication of transistors, but this rapid progress appears to have a limit due to effects of quantum mechanics [1]. Quantum effects are already important in devices on the order of a few nanometers [2] and are potentially debilitating below these sizes. There are a number of possibilities for progress beyond silicon MOSFETs. Some of these include new logic devices such as molecular transistors, single electron transistors and spin transistors while other involve completely different architectures such as quantum cellular automata, cellular nonlinear networks and biologically inspired architectures [1]. One possibility is to use quantum mechanics itself to perform certain algorithms at speeds much faster than is possible on a classical computer. The exploitation of quantum mechanics to perform calculations is known as quantum computing.

### 1.2.1 Quantum Bits versus Classical Bits

Quantum computers are based on quantum bits (qubits) instead of classical bits. Mathematically a qubit has states $|0\rangle$ and $|1\rangle$ that are similar to the classical states 0 and 1. It can also have a state which is a quantum superpositions of $|0\rangle$ and $|1\rangle$

$$|\psi\rangle = \alpha|0\rangle + \beta|1\rangle \tag{1.1}$$

where $|\psi\rangle$ represents the state of the qubit and $\alpha$ and $\beta$ are in general complex numbers and must satisfy $\alpha^2+\beta^2=1$. A useful representation of the state of a qubit is a point on the surface of a sphere called the Bloch sphere, introduced in Sec. 1.4.1.

In a classical computer the state of the bit is measured exactly and the result is 0 or 1 depending on the state of the bit. When a qubit is measured it also returns $|0\rangle$ or $|1\rangle$. However the measurement only returns $|0\rangle$ with a probability $\alpha^2$ and $|1\rangle$ with a probability of $\beta^2$. The probabilistic nature of quantum mechanics does not allow the measurement to uniquely determine the state of the system. The difference between the quantum observables of the qubit and information contained in the state of the qubit is a key concept in many quantum algorithms.

The qubit is most often realized experimentally via a quantum two level system. Since quantum mechanics is the fundamental basis of our world there exists many quantum two levels system in all branches of physics. Some examples of basic two state systems include the vertical and horizontal polarization of photons, the two spins states of spin 1/2 particles and the ground and excited states of atoms.

Two coupled qubits would have four computational basis states denoted $|00\rangle$, $|01\rangle$, $|10\rangle$ and $|11\rangle$. The general state is a superposition of the four states

$$|\psi\rangle = \alpha_{00}|00\rangle + \alpha_{01}|01\rangle + \alpha_{10}|10\rangle + \alpha_{11}|11\rangle \tag{1.2}$$

where the sum of coefficients squared must again give unity probability. A $n$ qubit system would require $2^n$ coefficients in order to specify the state of the system. For even small numbers of qubits the number of coefficients is quite large. This scaling is what makes it so hard to simulate even a moderate size quantum system on a classical computer. However a quantum computer uses nature itself to keep track of the coefficients. A collection of $n$ qubits has the potential to represent exponentially more data than $n$ classical bits. The problem is extracting the necessary information at the end of the calculation. The measurement projects the system with this vast hidden information onto a single basis state with a given probability.

The trick to quantum algorithms is to follow a superposition of computational paths and to produce a final state based on a quantum interference of all the computational paths [3]. The quantum entanglement of qubits allows the inputs to be coded into a multi-qubit superposition while quantum interference allows the qubit to interact in a prescribed way to produce the output. Quantum computers can be thought of as multi-particle interferometers in analogy to a Mach-Zehnder interferometer. First a photon goes through the first beam splitter creating a superposition of the path states. The phase is

shifted in one of the arms of the interferometer (a form of single qubit gate) and the components of the wavefunction are recombined at the second beam splitter, with each detector detecting the photon with a probability which is a function of the accumulated phase. All known quantum algorithms can be cast in terms of this idea of the entanglement of computational paths with enhancement of the correct path via quantum interference [3].

In 1982 Richard Feynman suggested that building computers based on the principles of quantum mechanics would avoid the difficulty of simulating a quantum system on classical computers [4]. Then in 1985 David Deutsch suggested via a simple example that quantum computers might have computational powers exceeding those of a classical computer [5]. However, the field of quantum computation exploded with Peter Shor's 1994 discovery of quantum algorithms for prime factorization and discrete logarithms that are exponentially faster than the best known classical algorithms [6, 7]. The idea that a quantum computer could provide such a dramatic improvement is strong motivation to try and build one. The exponential speed increase in factoring large numbers is especially enticing to those who wish to break the current standard encryption system (RSA) which is based on the difficulty of solving this problem. Grover's search algorithm [8] demonstrated another type of problem where a quantum computer could outperform a classical computer, although in this case the improvement is less dramatic. These algorithms along with the possibility of efficiently simulating quantum systems have led many experimental groups to pursue experimental realizations of a quantum computer.

### 1.2.2 Physical Qubits

There exist many two level quantum systems in nature but most are not suitable for large scale quantum computing. The standard criteria for judging the suitability of a specific qubit are codified in the DiVincenzo criteria [9]. They are organized into five requirements for the implementation of quantum computation.

1. A scalable physical system with well characterized qubits
2. The ability to initialize the state of the qubits to a simple fiducial state, such as $|000...i\rangle$
3. Long relevant decoherence times, much longer than the gate operation time
4. A universal set of quantum gates

5. A qubit-specific measurement capability

Simultaneously satisfying all five criteria seems to be very challenging. Although there are many two level quantum systems with well understood Hamiltonians, most of them are not scalable. However, in many cases the systems that are most scalable interact strongly with other qubits but also interact strongly with the environment. This is at odds with the third requirement, long relevant decoherence times. Also the last requirement, qubit-specific measurement, usually requires strong coupling to some part of the environment. The fourth requirement demands sufficient control over the qubit Hamiltonian possibly affecting decoherence through noise in the external control.

Despite these daunting criteria, many different physical systems are being pursued in relation to quantum computing. Probably the most successful qubit implementation thus far has been the nuclear magnetic resonance (NMR) approach using electron or nuclear spins in a static field manipulated by rf pulses. The natural interactions of the spins provide the coupling between qubits. A number of quantum algorithms have been tested using liquid-state NMR including the quantum Fourier transform [10] and Shor's algorithms [11] on 3 qubits. However there are severe limitations to the scaling beyond 10 qubits [12]. It might be possible to improve the scalability beyond 10 qubits using solid state NMR [13].

Another popular qubit implementation is that of cold ions interacting with laser light while moving in a linear trap [14]. The two computational states are associated with internal states of the ions such as the ground and first excited energy levels. The computation is performed on a superposition of these states in different ions coupled by the collective motion within the trap. The individual ions are addressed via interaction with the laser light. These systems are appealing because the decoherence of the individual ions is negligible. A 2 qubit c-NOT gate was demonstrated [15] not too long after the initial proposals. Currently these systems are limited by the collective motion of the trap. This method of coupling limits the gate speed and the collective motion becomes more complicated as more ions are added [16].

Neutral atoms are appealing candidates for qubits due to their weak interaction with their environment, implying long coherence times. However the weak interaction means they do not couple strongly to other qubits. The coupling is accomplished via modes of an appropriate cavity or by loading the atoms into an optical lattice and inducing a dipole-dipole interaction or cold collisions [16]. Problems with lattice implementations include the lack of a mechanism to address individual atoms and no error correcting codes suitable to the lattice geometry. Limitations to the cavities prevent scaling to large numbers of qubits, but their ability to couple to photons makes them

promising in terms of distributed quantum computing and quantum information [17].

The success of CMOS and the rapid progress in nanofabrication has inspired a large number of solid state approaches to quantum computing. Many of these approaches are based on methods of localizing spin or charge states of electrons or nuclei in solids. The localization is accomplished by a variety of techniques including quantum dots, impurity atoms and surface acoustic waves. Two of the more common physical systems are the nuclear spins of P donors in silicon and the electron spin in GaAs quantum dots. Most of the advantages in these devices relate to scaling but these devices have been slow to demonstrate the possibility of achieving suitable coherence times [17].

### 1.2.3 Superconducting Qubits

Superconducting qubits exploit the quantum nature of the superconducting ground state through the collective modes of the superconducting circuit elements. Unlike microscopic quantum systems such as spins and atomic ground states, these circuit elements are easily coupled through electric and magnetic fields. Superconducting qubits are potentially highly scalable since they are realized using lithography techniques similar to those of silicon transistors. The important question, and a major theme of this thesis, is whether the coherence in these circuits can be preserved long enough to use them as qubits.

All proposed superconducting qubits utilize the dissipationless non-linear behavior of Josephson junctions to engineer a quantum state suitable for quantum computing. The most common type of Josephson junction consists of an insulating tunnel barrier between two superconducting electrodes. It can be characterized by its Josephson energy ($E_J = I_c\Phi_0/2\pi$), where $I_c$ is the critical current of the Josephson junction and $\Phi_0$ is a flux quantum, and the Coulomb charging energy ($E_C = (2e)^2/2C$) where $e$ is the charge on the electron and C is the capacitance across the junction [18].

The major difference between the various superconducting qubits is the ratio of $E_J$ to $E_C$ and the quantized variable. Superconducting qubits are generally classified as either phase, flux, persistent current or charge. Phase qubits, $E_J \gg E_C$ are based on the difference of the superconducting phase across the Josephson junction. Flux qubits, $E_J \gg E_C$, are based on the quantized flux in a superconducting loop interrupted by a Josephson junction. Persistent current qubits, $E_J > E_C$, are based on circulating currents in a superconducting loop interrupted by 3 or 4 junctions with the inductance provided by these junctions. Charge qubits, $E_J \ll E_C$, are based on the number of cooper pairs on a superconducting island. An rf SQUID with a tunable, $E_J$, is especially flexible and can be used as either a flux qubit or a

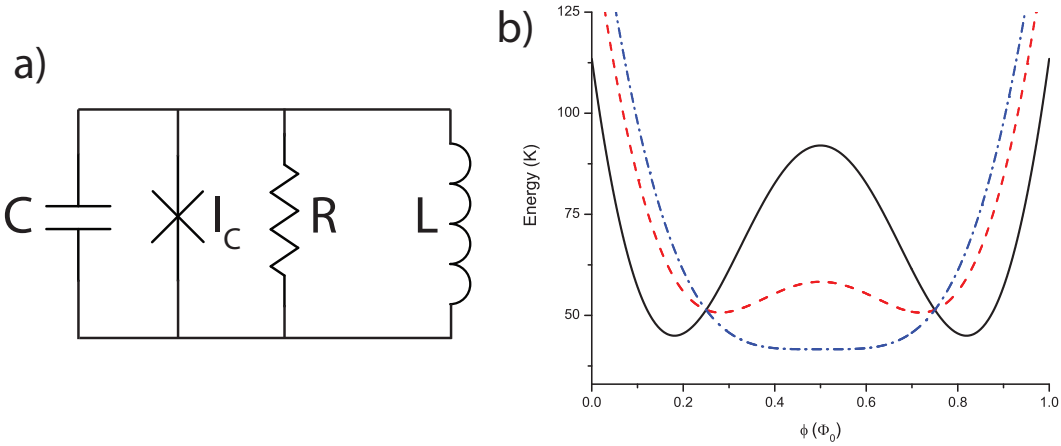


Figure 1.1: a) A schematic representation of a rf SQUID b) The potential energy of a rf SQUID at the symmetry point ($\phi_x = 1/2$) for L=189 pH and $\beta_L = 2.1$ (black solid), 1.4 (red dashed) and 1 (blue dash dot)

phase qubit.

The remainder of this thesis will focus on quantum coherence in a rf SQUID with the goal of understanding the mechanisms of its decoherence. The question of decoherence in these devices is important in both the context of quantum computing and the fundamental nature of quantum mechanics in macroscopic systems. The next section, will introduce the background of the rf SQUID necessary to discuss the experimental observations of Chapter 4. The final section of this chapter will provide a brief review the quantum two level system which is useful in understanding the experimental methods used to probe quantum coherence.

## 1.3 The rf SQUID Qubit

A rf SQUID is a superconducting loop interrupted by a single Josephson junction. A schematic of the equivalent circuit is shown in Fig 1.1 where L is the geometrical inductance of the loop, $I_c$ is the critical current of the junction, R is the normal resistance of the junction and C is the capacitance across the junction [19]. When an external flux ($\Phi_x$) is applied to the SQUID loop, it induces a screening current $I_s = -I_c \sin(2\pi\Phi/\Phi_0)$ where $\Phi_0 = \frac{h}{2e} = 2.068 \times 10^{-15}$ Wb is the flux quantum. The screened flux in the loop ($\Phi$) must satisfy, $\Phi = \Phi_x + LI_s$ [18]. The dynamics of this device are analogous to a particle of mass C with kinetic energy $\frac{1}{2}C\dot{\Phi}^2$ moving in a potential given by the difference between the loop's magnetic energy and the Josephson junctions

coupling energy [20, 21]

$$U(\varphi, \varphi_x) = U_0 \left[ \frac{1}{2}(\varphi - \varphi_x)^2 - \beta_L \cos(\varphi) \right] \tag{1.3}$$

where $U_0 \equiv \Phi_0^2/4\pi^2 L$, $\beta_L \equiv 2\pi L I_c/\Phi_0$ and $\varphi$ and $\varphi_x$ are $\Phi$ and $\Phi_x$ in units of $\Phi_0/2\pi$. Sometimes it is more convenient to use $\phi$ and $\phi_x$ which are also $\Phi$ and $\Phi_x$ in units $\Phi_0$. In many cases it interesting to vary the applied flux on a small scale around the symmetry point $\phi_x = 1/2$. In this case it is convenient to plot $\phi_{x[1/2]}$ relative to $\phi_x = 1/2$. The potential is plotted in Fig. 1.1b as a function of $\phi_x$ for L=189 pH and $\beta_L = 2.1$ (black solid line), 1.4 (red dashed line) and 1 (blue dash doted lined). The energy units are Kelvin using temperature as an energy via $E = k_B T$ where $k_B$ is Boltzmann's constant.

When $\phi_x = 1/2$ and $1 < \beta_L < 4.6$ the potential is symmetric about $\phi = 1/2$ with two wells separated by a potential barrier. The two local energy minima with respect to $\phi$ are given by minimizing Equ. 1.3 with respect to $\phi$ giving

$$\phi_{min} = \phi_x - \frac{\beta_L}{2\pi} \sin(2\pi\phi_{min}) \tag{1.4}$$

which must then be solved numerically for $\phi_{min}$. The two potential wells are different fluxoid states of the qubit and correspond to currents, approximately 3 $\mu A$ for our current samples, circulating in opposite directions around the loop. Changing $\phi_x$ to a value other than 1/2 tilts the potential as shown in Fig. 1.2. The screening current changes to try and compensate for the change in $\phi_x$ until it is no longer energetically favorable and the system moves to the next fluxoid state.

Experimentally it is very convenient to be able to adjust the height of the barrier of the double well potential independently of $\Phi_x$. However the height of the barrier is fixed by the critical current of the Josephson junction. The critical current can be adjusted if the single junction is replaced by two junctions in a small loop, a dc-SQUID, with inductance $\ell$. By applying flux to the small loop using $\Phi_{xdc}$, the critical current of the dc-SQUID is suppressed allowing the barrier of the double well potential to be modulated. The addition of the dc SQUID turns the potential into a two dimensional potential, one for the big loop ($\Phi$) and one for the small loop ($\Phi_{dc}$). If the $\beta_L$ for the small loop is much less then one and L is much bigger then $\ell$, then the potential can be treated as one dimensional potential with small corrections [22–24]. The $\beta_L$ in Equ. 1.3 can be replaced with

$$\beta_L(\Phi_{xdc}) = \beta_{L0} \cos\left( \frac{\pi \Phi_{xdc}}{\Phi_0} \right) \tag{1.5}$$

where the maximum ($\beta_{L0}$) occurs at integer values of applied flux.

### 1.3.1 Hamiltonian

The energy levels and wavefunctions are calculated directly from the Hamiltonian for the isolated rf-SQUID. For zero temperature and zero dampening the Hamiltonian is [21, 25]

$$H(\varphi, \varphi_x) = \frac{Q^2}{2C} + U(\varphi, \varphi_x) \tag{1.6}$$

where C is the capacitance and Q, the charge on the junction, is conjugate to the phase across the junction and therefore the flux through the loop $\varphi$ [19]. The conjugation relation is

$$\left[\frac{\Phi_0}{2\pi}\varphi, Q\right] = \imath\hbar \tag{1.7}$$

which when acted on test function [26] gives Q in terms of $\varphi$.

$$Q = \frac{\hbar}{\imath}\left(\frac{2\pi}{\Phi_0}\right)\frac{\partial}{\partial\varphi} \tag{1.8}$$

The Hamiltonian can be rewritten as

$$H = \frac{-\hbar^2}{2C}\left(\frac{2\pi}{\Phi_0}\right)^2\frac{\partial^2}{\partial\varphi^2} + \frac{1}{2}U_0\left(\varphi - \varphi_x\right)^2 + E_J\cos(\varphi) \tag{1.9}$$

where $E_J \equiv I_c\Phi_0/2\pi$.

This Hamiltonian is equivalent to a particle of mass $C\left(\frac{\Phi_0}{2\pi}\right)^2$ moving in the double well potential. The oscillation frequency at the bottom of one of the wells can be approximated as a harmonic oscillator. The energy is oscillating between the capacitance of the junction and the inductance of the loop. The frequency of oscillation is called the plasma frequency ($\omega_p$) and is calculated by Taylor expanding the potential about the minimum to get a quadratic term and dividing by the effective mass.

$$\omega_p = \left(\frac{1}{C}\left(\frac{2\pi}{\Phi_0}\right)^2\frac{\partial^2 U}{\partial\varphi^2}\Big|_{\varphi=\varphi_m}\right)^{1/2} \tag{1.10}$$

substituting the potential, Equ. 1.3,

$$\omega_p = \sqrt{\frac{1 + \beta_L \cos(\varphi_{min})}{LC}} \tag{1.11}$$

Equation 1.9 is very similar to the Hamiltonian for a harmonic oscillator. This similarity was exploited by Lapointe et al.[27] to numerically solve Equ. 1.9 to find its eigenstates and eigenfunctions. The Hamiltonian is first rewritten as a simple harmonic oscillator Hamiltonian plus a cosine term,

$$H = \frac{-\hbar^2}{2m}\frac{\partial^2}{\partial x^2} + \frac{1}{2}m\omega^2 x^2 - E_J \cos[2\pi(x + x_0)] \tag{1.12}$$

where $m \equiv C\Phi_0^2$, $\omega^2 \equiv 1/LC$, $x \equiv \phi - \phi_x$ and $x_0 \equiv \phi_x$. The cosine term is then expressed in terms of raising, and lowering operators of the simple harmonic oscillator. The resulting Hamiltonian is used to construct a matrix in the basis states of the simple harmonic oscillator. This matrix is diagonalized to find the eigenenergies and eigenstates of the rf SQUID. The average flux for a specific energy level can be found by applying the position operator to the corresponding eigenstate. For the simple harmonic oscillator basis this gives [28]

$$\langle\phi\rangle = \langle n'|\Phi|n\rangle = \frac{1}{\sqrt{2}\alpha}\left(\sqrt{i+1}\delta_{n',n-1} + \sqrt{i}\delta_{n',n+1}\right) \tag{1.13}$$

where $\delta$ is the usual Kronecker delta and $\alpha \equiv \sqrt{\frac{m\omega}{\hbar}}$.

This method of finding the energies and eigenstates was used extensively in the data analysis presented in this thesis. The accuracy of the calculation depends on the size of the matrix used. To calculate the energies of the first few levels, a matrix size of $70 \times 70$ is sufficient. For large barriers and large numbers of levels in the well, on the order of 50, larger matrices are necessary, i.e. $200 \times 200$.

### 1.3.2 Energy Levels and Wavefunctions

Figure 1.2 shows the potential with the first 15 energy levels and the corresponding values of the mean flux for a $\beta = 1.32$ and $\phi_x = 0.507$. At this $\phi_x$ value, the levels in different wells are not aligned. Below the barrier the levels are localized in either the left well or the right well. Deep in these wells the potential is similar to a simple harmonic oscillator, and the eigenenergies and wavefunctions can be approximated as those of the harmonic oscillator. The levels spacing is approximately that of the harmonic oscillator $\hbar\omega_p$, using $\omega_p$ from Equ. 1.11. However as the levels get closer to the top of the barrier, the

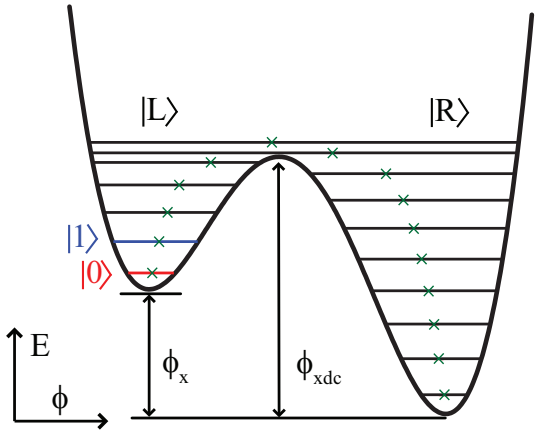


Figure 1.2: The potential of an rf-SQUID at a $\beta = 1.32$ and $\phi_x = 0.505$ showing localized energy levels and the corresponding value of mean flux (green x).

potential becomes more anharmonic, causing the level spacing to get smaller.

Figure 1.3a shows the wavefunction for a $\beta = 1.2$ with a $\phi_x = 0.5038$. Each eigenstate of the double well potential is a weighted sum of the harmonic oscillator wavefunctions and is plotted using the Hermite polynomials. The wavefunction localized in the right well are plotted using red dashed lines while those localized in the left well are plotted using blue solid lines. The levels above the barrier are shown using purple dashed dotted lines. Near the top of the barrier the wavefunctions begin to have some amplitude in the other well.

At certain values $\phi_x$ levels in opposite wells will approximately align and the eigenstates are no longer localized in individual wells. Figure 1.3b shows the wavefunctions for a $\beta = 1.2$ and $\phi_x = 0.5$. The symmetric wavefunctions are shown using a dashed red lines while the antisymmetric wavefunctions are shown using a solid blue line. The fluxoid states are not eigenstates of the system but superpositions of the eigenstates. If the system is initialized in one of the fluxoid states, it will not remain in the state but oscillate back in forth between the fluxoid states. The oscillations correspond to the system tunneling back and forth though the barrier.

Figure 1.4a shows the energy levels as a function of $\phi_x$ at a $\beta_L = 1.2$. The levels localized in the left well have positive slope while the levels localized in the right well have negative slope. At certain $\phi_x$ values the levels in the left well appear to cross levels in the right well. Due to the coupling between the two states the levels do not cross but instead have an anticrossing. The anticrossing between the first two levels is shown in Fig. 1.4b. The energy splitting at the crossing, $\Delta$, is a function of how close the level is to the top of

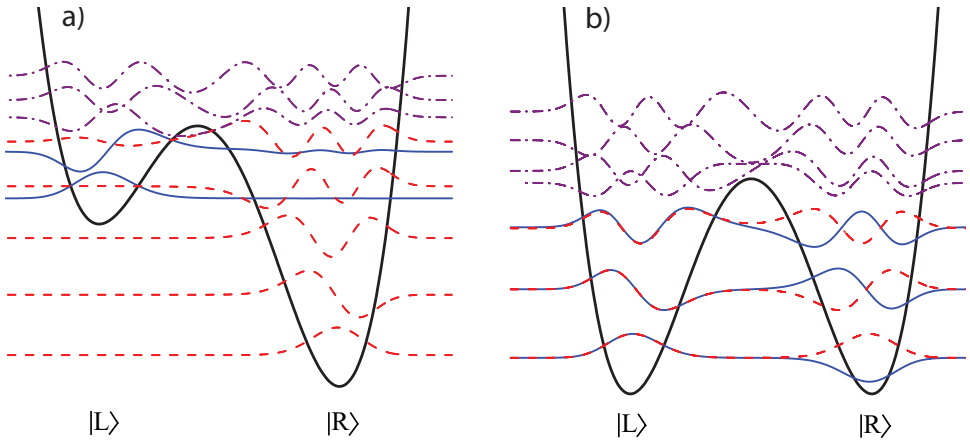


Figure 1.3: a) The potential of an rf-SQUID at a $\beta = 1.2$ and $\phi_x = 0.5038$ showing the eigenfunctions localized in the right well (red dashed line), left well (blue solid line) and above the barrier (purple dashed dotted line). b) The potential of an rf-SQUID at a $\beta = 1.2$ and $\phi_x = 0.5$ showing the eigenfunctions of the coupled symmetric (red dashed line) and antisymmetric (blue solid line) states and also states above the barrier (purple dashed dotted line)

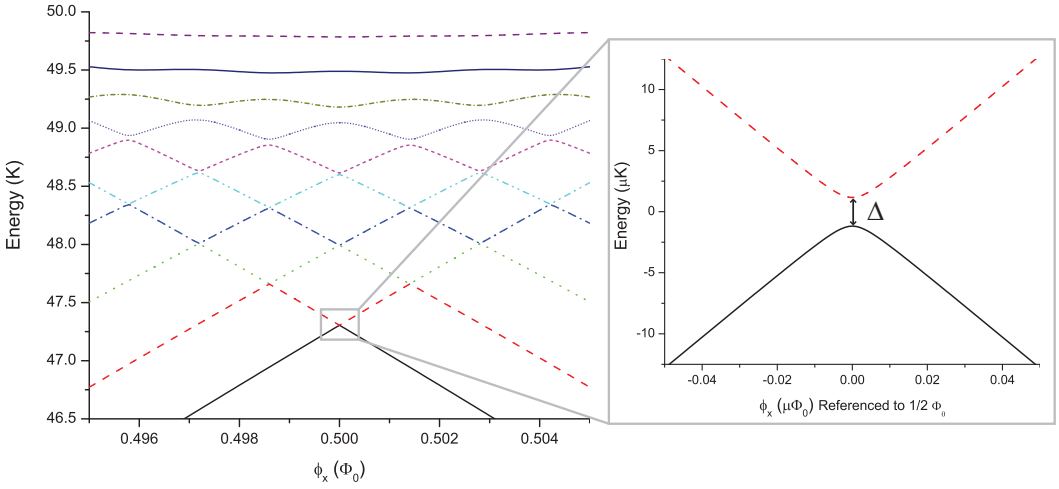


Figure 1.4: a) The first 10 energy levels of an rf-SQUID as a function of $\phi_x$ at a $\beta = 1.2$. b) A detailed view of the energy splitting between the ground state and first excited state.

the barrier. The higher energy levels near the top of the barrier show larger splittings. Friedman et al. [20] have observed the splitting between states close to the top of the barrier in an rf SQUID.

### 1.3.3 Quantum Tunneling

Since the flux states are not eigenstates of the system, there is a non-zero chance of tunneling from one fluxoid state to the other. For the majority of the measurements shown in this thesis, the temperature of the rf SQUID is low enough that quantum tunneling though the barrier is much more likely than thermal excitation overtop the barrier, $kT \ll \hbar\omega_p$. Quantum tunneling through a potential barrier has been studied theoretically and experimentally in both Josephson junction systems [29–31] and rf SQUIDs [25, 32, 33]. The escape rate out of a potential well into a continuum at zero temperature in the absence of dissipation can be calculated for a cubic barrier (i.e. $\Delta U \gg \hbar\omega_p$) using the WKB approximation [30, 34] and is

$$\Gamma_{escape} \propto \exp\left(-7.2\frac{\Delta U}{\hbar\omega_p}\right) \tag{1.14}$$

where $\Delta U$ is the effective barrier height.

For the rf SQUID, the tunneling rate depends on both the initial and final states. Rouse et al. [25] have observed tunneling between quantized states though the barrier of a rf SQUID. They observe an enhancement of the escape rate from one fluxoid state to the other fluxoid state when the lowest energy level from one well approximately aligns with energy levels in the other. When the energy difference between the levels ($\varepsilon$) in opposite wells is much less than $\omega_p$ the two states couple strongly and can be described using a two state Hamiltonian [35]

$$H_0 = \frac{1}{2}\left[\varepsilon(|0\rangle\langle 0| - |1\rangle\langle 1|) - \Delta(|0\rangle\langle 1| + |1\rangle\langle 0|)\right] \tag{1.15}$$

where $\Delta$ is the tunneling amplitude. If the energy relaxation is assumed to be greater then the interwell relaxation and the qubit initially starts in the left well in the lowest energy level, then the dynamics depend on $\Gamma_n$, the relaxation rate of the $n_{th}$ level in the right well. If $\Gamma_n$ is much less than the oscillation frequency $\Omega = \sqrt{\varepsilon^2 + \Delta^2}$, the system exhibits damped coherent oscillations between the fluxoid states followed by a relaxation in the right well. As $\Gamma_n$ increases the coherent oscillations become incoherent jumps of the flux into the right well followed by a rapid decay. The escape rate from the left well is

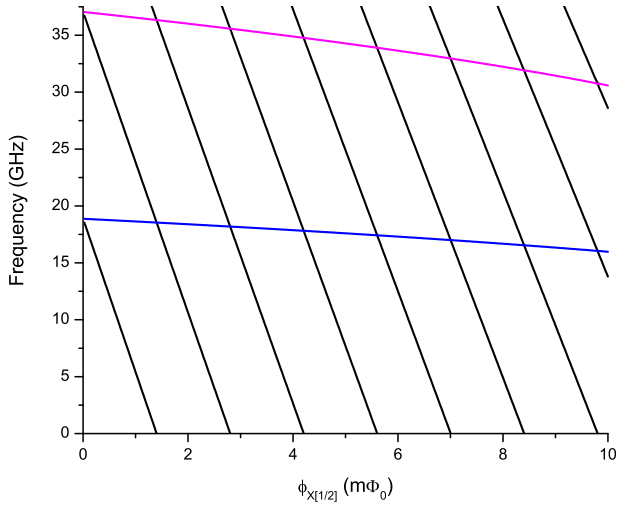


Figure 1.5: The energy levels of an rf SQUID as a function of $\phi_x$ referenced to the energy of the lowest energy level in the left well at a $\beta_L = 1.33$. The coupling between states is ignored in order to show the relevant microwave frequencies of the localized states. The blue and magenta horizontal lines are the first and second excited states respectively in the left well while the black lines are the levels in the right well.

then [35]

$$\Gamma_{esc} = \frac{\Delta^2 \Gamma_n}{2\Delta^2 + \Gamma_n^2 + 4\varepsilon^2} \tag{1.16}$$

### 1.3.4 Applied Microwaves

A rf signal applied to the qubit at frequencies close to the energy difference between two levels can drive transitions between these levels. Experimentally the rf signal is inductively coupled to the qubit from a high frequency transmission line. For the parameters of these rf SQUIDs, the frequency difference between consecutive energy levels in same well is a function of both $\phi_x$ and $\phi_{xdc}$; from 40 GHz to 10 GHz for a $\beta_{L0} \approx 2.2$. The resonant frequency to the second excited state is approximately twice that to the first excited state. The microwaves can also cause transitions between coupled energy levels in different flux states with the minimum frequency determined by the coupling between the states. The energy of the eigenstates relative to the ground state in the left well is shown in Fig. 1.5 as a function of $\phi_x$ at a $\beta_L = 1.33$. The coupling between states is ignored in order to show the relevant microwave frequencies of the localized states. The microwaves are useful to study the qubit via spectroscopy and tunneling. It is also important to use pulsed microwaves

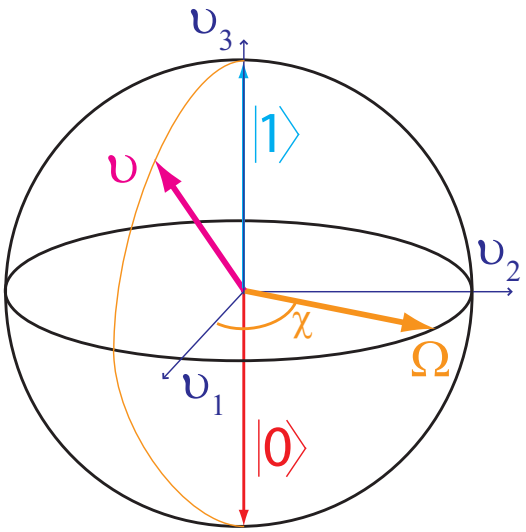


Figure 1.6: The Bloch sphere representing all the possible quantum states of a two level system. The Bloch vector $\boldsymbol{\upsilon}$ (magenta) representing the quantum state at a given moment is time, rotates around the torque vector $\boldsymbol{\Omega}$ (orange). The occupation of the energy states is represented by the projection of the Bloch vector on to the $\upsilon_3$ axis.

for state preparation and gate operation during qubit operations. The microwave excitation is discussed further in the following sections in terms of a two state system.

## 1.4 The Quantum Two Level System

The lowest two levels in a given well provide a convenient basis to measure the decoherence in this system. The energy difference between these levels is engineered to be between 10 and 40 GHz, within the frequency range of the inductively coupled transmission lines. The decoherence can be probed using techniques commonly used to analyze spin systems in magnetic resonance experiments [36] and optical resonance in two-level atomic systems [37].

### 1.4.1 Bloch Equations

The generalized Bloch equations describes a two level system driven by a resonant transverse field [38]. The equations are in terms of a pseudospin vector $\boldsymbol{\upsilon}$ where $\upsilon_3$ depends on the difference between the population of the ground and excited states and $\upsilon_1$ and $\upsilon_2$ characterize the coherence between

states. In a reference frame rotating at the driving frequency $\omega$, the Bloch equations are

$$\begin{aligned} \dot{v_1} &= -\delta(t)v_2 - \frac{v_1}{T_2} \\ \dot{v_2} &= \delta(t)v_1 - \frac{v_2}{T_2} + a_{rf}(t)v_3 \\ \dot{v_3} &= -\frac{v_3 - v_{3eq}}{T_1} - a_{rf}(t)v_3 \end{aligned} \tag{1.17}$$

where $\delta(t) = \omega(t) - \omega_0$ and $a_{rf}(t)$ is the amplitude of the applied microwaves. $T_1$ and $T_2$ are phenomenological decay constants describing the longitudinal and transverse relaxation times. The longitudinal relaxation corresponds to energy loss to the environment and the transverse relaxation corresponds to loss of coherence caused by dephasing.

The pseudospin vector can be be visualized as a point on a sphere, called the Bloch sphere, Fig. 1.6, that is a representation of all the possible states of the two level system. The ground state is the south pole and the excited state is the north pole. All of the points in between represent a possible state representing the population in the excited state and a quantum phase. In this model, the motion on the Bloch sphere is determined by a "torque" vector given by

$$\mathbf{\Omega} = (-a_{rf}, 0, \delta) \tag{1.18}$$

The torque vector is a function of the driving amplitude and the detuning.

In the analysis in Chapter 4, Equ. 1.17 are solved numerically in order take into consideration the finite rise times of the microwave pulses and to allow for time dependent detuning. The numerical solutions also allow different types of noise to be included in the calculations.

### 1.4.2 Coherent Oscillations "Rabi Oscillations"

There exists an analytic solution for the population of the excited state to Equ. 1.17 for constant amplitude rf pulses. Assuming no decoherence and that the system starts in the ground state at time zero

$$v_3(t, \delta) = -1 + \frac{2a_{rf}^2}{a_{rf}^2 + \delta^2} \sin^2(\Omega_{Rabi}(\delta)t/2) \tag{1.19}$$

where

$$\Omega_{Rabi}(\delta) = \sqrt{\delta^2 + a_{rf}^2} \tag{1.20}$$

This solution, shows that when driven with microwave power, the population

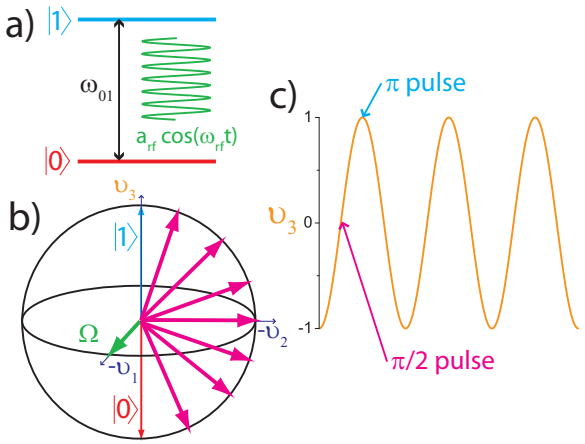


Figure 1.7: The relevant energy levels a) defining the parameters for Rabi oscillations shown on b) the Bloch sphere and c) as a projection on the $\upsilon_3$ axis as a function of time. A $\pi$ pulse sends the Bloch vector from the south pole to the north pole in the plane $\upsilon_1 = 0$

of the excited states oscillates back in forth in time, demonstrating the phenomenon of Rabi oscillations (Fig. 1.7c). The observation of Rabi oscillations are considered one of the important steps in developing solid state qubits. Rabi oscillations have been demonstrated in a number of different superconducting qubits [39–43]. The frequency of the oscillations ($\Omega_{rabi}$) is proportional to the amplitude of the microwaves excitation $a_{rf}$ when on resonance. This proportionality is often cited as experimental proof that the observed oscillations are Rabi oscillations as opposed some other type of population oscillation.

Using a microwave pulse on resonance for half a Rabi period, known as a $\pi$ pulse, the qubit coherently moves from the ground state to the excited state with unity probability. By using a pulse half as long, know as a $\pi/2$ pulse, it is possible to put the qubit into a coherent equal superposition between the ground and excited state. More generally, any state of the qubit can be initialized and all single qubit gates can be performed using only microwave pulses.

On the Bloch sphere, Rabi oscillations are rotations around the sphere along the axis perpendicular to the direction of the torque vector, which is set by the detuning and the phase of the microwaves. For this discussion, the phase will be chosen such that the torque points along the $\nu_1$ axis. On resonance, the Bloch vector, travels in the $\upsilon_1 = 0$ plane, passing through the poles. The system returns to its initial state every period of the Rabi frequency. Detuning tips the vector away from the equatorial plane which causes the Bloch vector to move in a non-polar orbit. The result of the detuning is that the Rabi

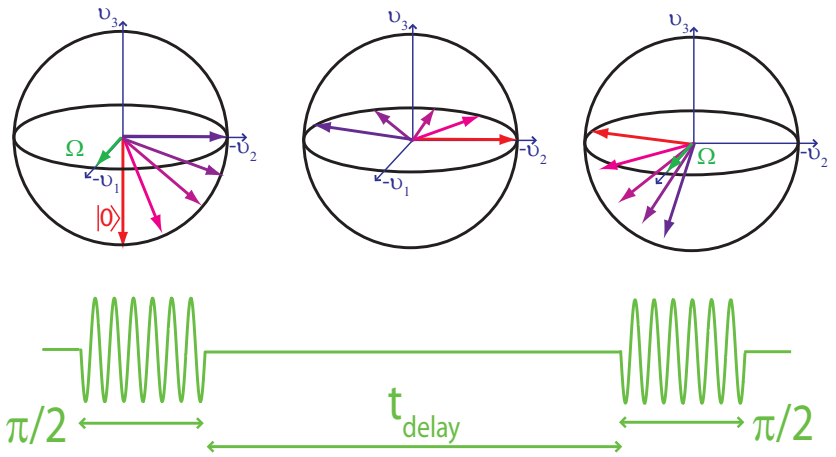


Figure 1.8: A schematic representation of the Bloch sphere for the Ramsey pulse sequence shown at the bottom. The three spheres show the Bloch vector during a) the first $\pi/2$ pulse, b) the free decay between microwave pulses and c) the second $\pi/2$ pulse. The passage of time is depicted as the color of the Bloch vector, red being earlier and blue later.

frequency increases and the amplitude of the oscillation decreases.

The Rabi oscillations damp out with a decay time limited by the decoherence. The exact form of the decay of the oscillations depends on the nature of the decoherence. The phenomenological decay constants used in Equ. 1.17 cause the Rabi oscillations to decay exponentially. These decay constants are often used to compare the levels of decoherence in different qubits. However in many cases, including some of the data from Chapter 4, the decay of the coherent state is not exponential and cannot be described using only the phenomenological decay constants.

### 1.4.3 Free Evolution

The Rabi oscillations take place in a basis of the two level system coupled to the microwave field. A more direct probe of the dephasing would be to measure the decay of the state when the microwaves are off, or the equivalent measurement to the free induction decay in NMR and the Ramsey pulse sequence in a two level "atom" [37].

The measurement consists of giving a $\pi/2$ pulse to put the system in a equal superposition of the ground and excited states, followed by some delay in which the state evolves freely before another $\pi/2$ pulse projects it towards either the ground or excited state, depending on the phase accumulated during

the delay. In terms of the Bloch sphere, the $\pi/2$ pulse causes the Bloch vector to travel along the $\upsilon_2 = 0$ arc up to the equatorial plane, $\phi = 0$. While the microwaves are off the vector rotates around $\upsilon_3$ axis in the equatorial plane at the detuning frequency. It rotates at the detuning frequency because we chose a reference frame that is rotating at $\omega_{rf}$. If the vector is pointing along the $-\upsilon_2$ axis when the second $\pi/2$ pulse arrives it will be projected into the excited state. However if it lies along the $\upsilon_2$ axis, it will be projected into the ground state. Anywhere in between, it will be projected into the excited state or ground state with the probability determined by the angle of the vector projected on to the equatorial plane and $\nu_2$.

This process is repeated many times as a function of the delay between the $\pi/2$ pulses. The probability of ending up in the excited state oscillates at the detuning frequency $\delta$. When the decay constants are included the result is a decaying oscillation that provides information about dephasing. Spin Echo consists of a similar pulse sequence but with a $\pi$ pulse between the $\pi/2$ pulses that can reduce the effect of low frequency noise. A number of groups have observed Ramsey fringes [40, 41, 43] or the spin echo decay [44, 45] in superconducting qubits.

# Chapter 2

# Experimental Setup

The fragile nature of quantum coherence in superconducting qubits places strict requirements on the design of the qubit, its readout and the experimental apparatus. This chapter carefully details the experimental setup giving special attention to aspects of the design that help preserve the coherence of the qubit and the novel features of the setup.

## 2.1 Superconducting Qubit Fabrication

All superconducting qubits, including the rf SQUID qubit, are made possible by the development of robust Josephson junction fabrication technologies. The majority of superconducting quits are $Al/AlO_x/Al$ junctions fabricated using two angle shadow evaporation [41, 42, 46, 47]. Other groups using $Al/AlO_x/Al$ junctions use a process of ion-mill cleaning followed by thermal oxidation [48, 49]. A few groups, including this group, fabricate $Nb/AlO_x/Nb$ junctions using Nb trilayer technologies capable of producing large-scale superconducting circuit applications [50, 51]. The trilayer process is more suitable for large scale circuits than the shadow evaporation process and therefore more practical for large scale quantum computing. Niobium films are also more robust due to aluminum junctions's relatively short lifetime when they are not stored under vacuum.

The various materials and fabrication steps can affect the coherence times of the qubit. A thorough explanation of the fabrication process is necessary in order to accurately compare qubits made using a different process or different materials. The trilayer process used for these samples [52, 53] is designed to minimize the number of steps shortening the turn around time and simplifying characterization of decoherence due to the process and the materials. The process is based on self-aligned lift-off (SAL) of the dielectric and uses both

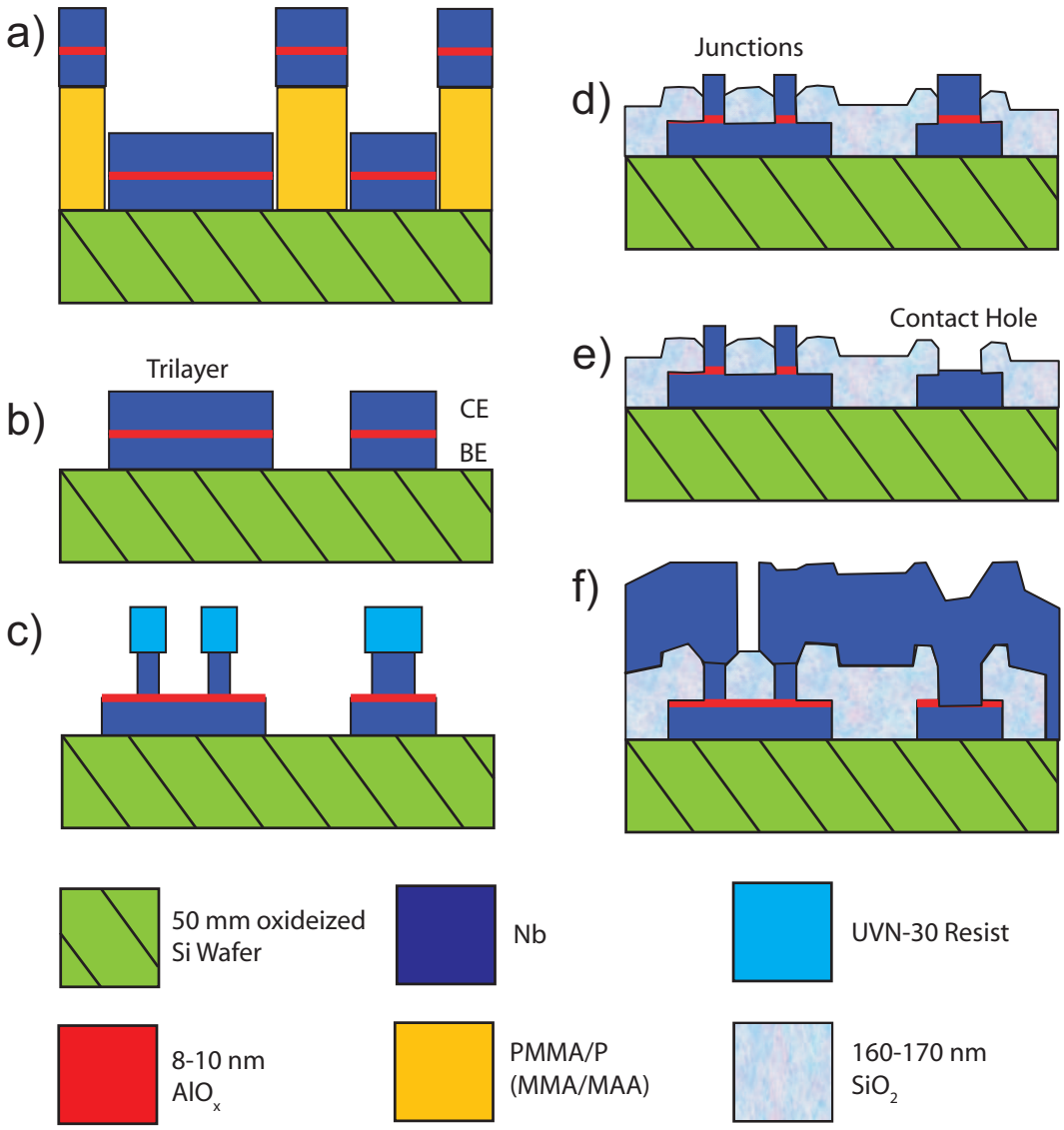


Figure 2.1: Process flow for the SAL-EBL fabrication shown at various stages a) after trilayer deposition, b) after trilayer liftoff, c) after RIE of CE, d) after deposition of $SiO_2$ and stripping of resist, e) after RIE and wet etch to define contact holes and f) after liftoff of wiring layer

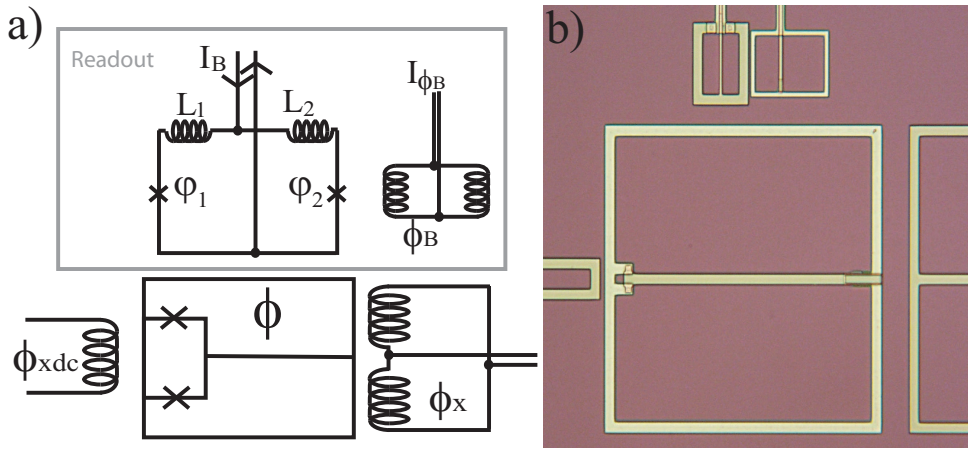


Figure 2.2: a) Schematic and b) photograph of rf SQUID qubit and the readout magnetometer.

UV and electron beam lithography (EBL). The EBL allows for junction sizes as small as 0.15 $\mu m$ x 0.15 $\mu m$.

The SAL process, shown in Fig. 2.1, starts with the patterning of the $Nb/AlO_x/Nb$ trilayer via a lift-off to minimize the steps requiring reactive ion etching (RIE) of the Nb which can cause damage. The substrate for these samples is a 50 mm oxidized Si wafer. It is coated with a PMMA/P (MMA/MAA) bilayer which is then patterned by both UV lithography for large structures and EBL for small structures. The $Nb/AlO_x/Nb$ trilayer is deposited at a base pressure of $1 \times 10^{-7}$ Torr. The base electrode (BE) and counter electrode (CE) are 150 nm thick and deposited using DC magnetron sputtering. The Al interlayer, 8-10 nm thick, is also deposited using DC magnetron sputtering and oxidized by thermal oxidation using dry $O_2$ at 103-104 Torr-min. These parameters give critical current densities ($J_c$) for the junctions of 50-150 $A/cm^2$. After liftoff, the CE is patterned using the UVN-30 resist and defined by RIE in $SF_6$ plasma followed by a 160-170 nm thick layer of RF sputtered $SiO_2$ dielectric. Finally the UVN-30 resist is stripped, exposing the Nb CE and completing the self-aligned liftoff. The contact holes are defined similar to the junctions and formed by a $SF_6$ RIE of the CE followed by an Al wet etch. Finally the 250 nm thick Nb wiring layer is formed by liftoff.

## 2.2 Experimental Design and Setup

### 2.2.1 Qubit Design

The qubit design shown in Fig. C.1a is based on a previous rf-SQUID design [25] that uses a large gradiometric loop, $\phi$, in series with a small loop, $\phi_{dc}$ containing the Josephson junctions. As explained in Sec. 1.3, flux applied to the large loop tilts the potential while flux though the small loop modulates the effective critical current, lowering the barrier. The qubit loop is $150\mu m$ $\times$ $150\mu m$ with a 5 $\mu m$ wide trace, giving $L \approx 215pH$. The small loop is $5\mu m$ $\times$ $5\mu m$ giving $\ell \approx 10pH$. The inductances are calculated using the 3D-MLSI software package [54] and consistent with the measurements from Chapter 4. The size of the junctions varies from sample to sample depending on the desired parameters and is $1.45\mu m$ $\times$ $1.45\mu m$ for the majority of the data shown. The sizes of the junctions are consistent with the design size minus the known undercut and is verified by diagnostic devices on the same wafer. The current density for these devices, designed to be $J_c \approx 100$ $A/cm^2$, is also estimated from measurements of the diagnostic devices along with the junctions in the magnetometer.

The $\phi_x$ ($\phi_{xdc}$) bias coil is shown on the right (left) of Fig C.1a. The $\phi_x$ bias coil is designed not to couple to the $\phi_{dc}$ loop. There is a small coupling between $\phi_{xdc}$ and the $\phi$ loop but this can be measured and compensated. Both $\phi_x$ and $\phi_{xdc}$ couple to the magnetometer but this coupling can be compensated by the magnetometer's bias coil, $\phi_B$, which is designed not to couple to the qubit.

The flux is measured using a hysteretic dc SQUID magnetometer shown at the top of Fig C.1a. The magnetometer is designed so that its bias current $I_B$ does not couple to the qubit to first order hence fluctuations in $I_B$ do not reach the qubit. A detailed description of this design is the subject of Appendix A. The measured mutual inductance between the qubit and the magnetometer is 5 pH, consistent with the design value of 4.3 pH. The junctions of the magnetometer are 2.15 x 2.15 $\mu m$ and 2.85 x 2.85 $\mu m$ giving a maximum critical current of $10.8\mu A$. The operation of the magnetometer is explained in Sec. 2.4.

### 2.2.2 Pulse Chip

The purpose of the pulse chip is to couple fast flux pulses and microwaves pulses into the qubit. The pulse chip, shown in Fig 2.3, is suspended overtop of the qubit chip and allows time domain measurements of coherence times on nanosecond time scales. By fabricating the high frequency lines on a separate

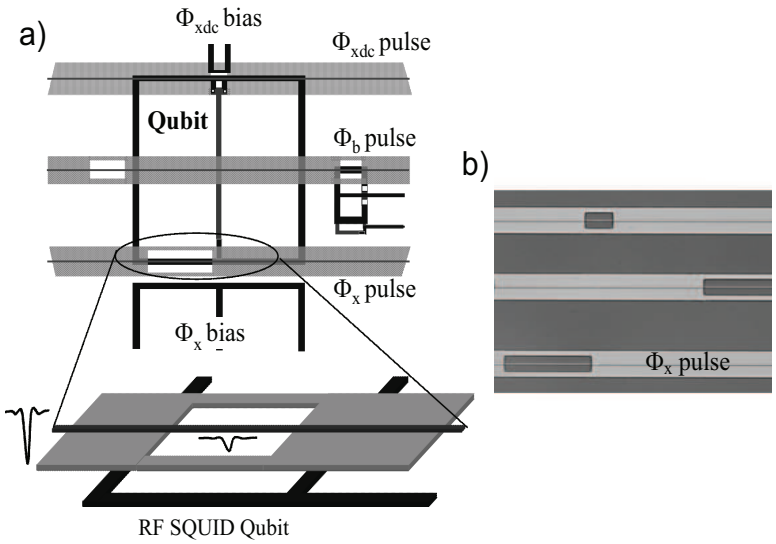


Figure 2.3: a) A drawing of the qubit chip with the superimposed pulse chip and b) a picture of the pulse chip showing both the microstrip lines and the ground plane holes.

chip, the qubit sample can be changed without changing the pulse lines. This removes the need to characterize the transmission lines every time the qubit chip is changed. The pulses are coupled through holes in the ground plane of superconducting microstrip transmission lines. The pulses coupled to the qubit have rise times less than 1 ns.

The pulse chips are fabricated on 2" fused quartz wafers. The coplanar waveguides and microstrip lines are formed by dc-sputtering 200 nm Nb films patterned using a combination of deep-UV and e-beam lithography. A 350 nm thick $SiO_2$ film is then rf-sputtered followed by etching contact vias which are subsequently filled with 250 nm of Nb. Next a 200 nm Nb film is deposited to form the microstrip ground planes. Finally 60 nm of gold is evaporated for the contact pads. The signal conductor of the microstrip is 1 $\mu m$ wide while the ground plane is 25 $\mu m$ wide.

The pulse chip and the qubit chip are aligned using precision translation stages while viewing "on chip" alignment marks under a microscope. With our present setup, the two chips can be aligned to better than one micron. The separation and hence the coupling between the chips is controlled by Kapton spacers. The mutual inductance between the $\phi_x$ pulse line and the qubit is $\sim$ 0.5 pH for a spacing of 25 microns (1 mil). A two micron misalignment reduces the coupling to $\sim$ 0.4 pH. The coupling between pulse chip and qubit chip is verified at 4.2 K by replacing the qubit with a dc-SQUID magnetometer.

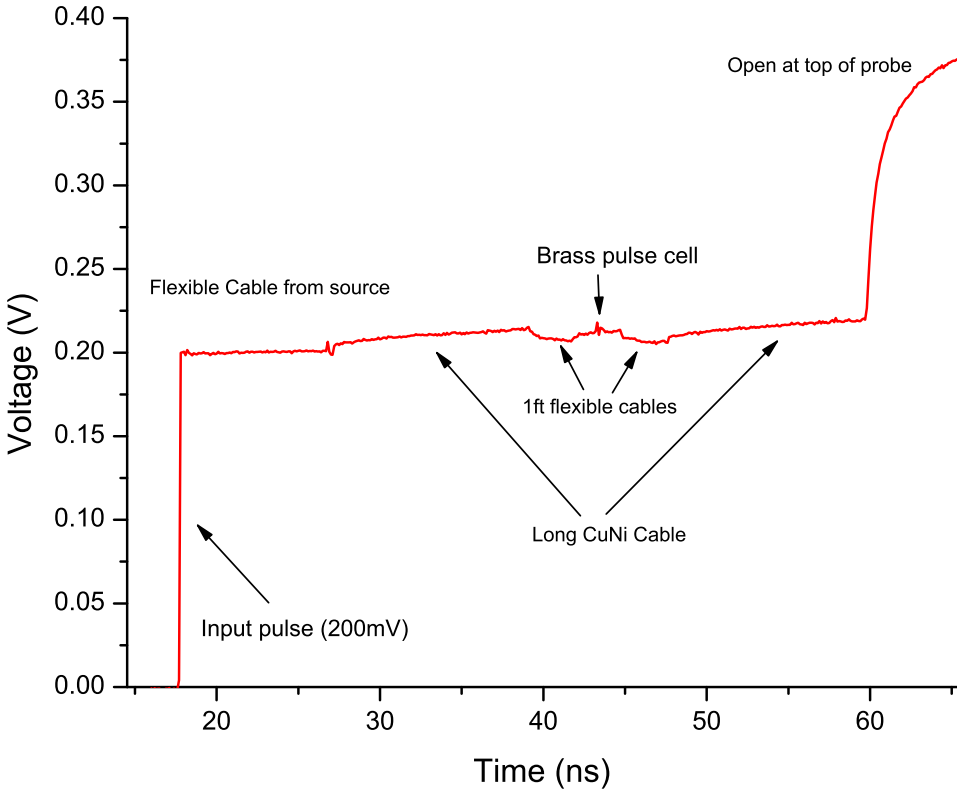


Figure 2.4: Time Domain Reflectometry measurement of the pulse chip mounted in sample cell. The sample cell is mounted in a dip probe immersed in liquid He at 4.2 K

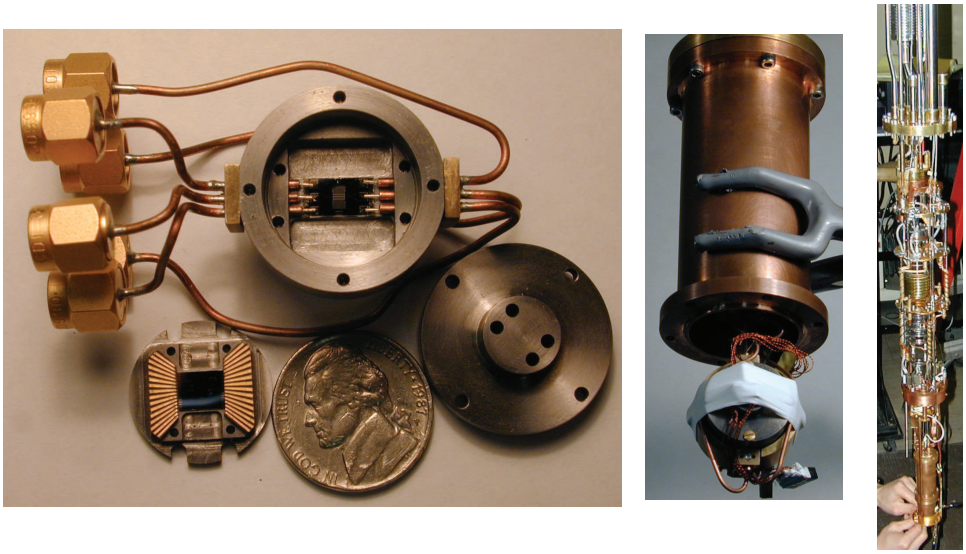

Figure 2.5: Photographs of a) the NbTi sample cell, b) the sample cell mounted in the outer sample can and c) the sample can mounted in the dilution refrigerator.

One advantage of using separate chips for the high and low frequency lines is that the same transmission lines can be used for many different qubit samples. Once the pulse chip is in place the transmission lines can be tested and characterized and do not need to be re-characterized for a new qubit design. Both the microstrip and the coplanar waveguide are designed to have a 50Ω impendence [55] and are simulated using high frequency simulation software, Sonnet [56, 57]. The pulse chip was carefully tested at 1.2 K using time domain reflectometry, shown in Fig. 2.4, and by measuring the transmitted microwave power through the pulse chip as a function of frequency up to 20 GHz. These measurements show that there are no mismatches greater than 3Ω at any of the transmission line transitions.

### 2.2.3 Sample Cell

The qubit chip and all the necessary wires and cables are housed in a sample cell mounted inside an outer sample can. The sample cell is a superconducting NbTi can that acts as a magnetic shield below its transition temperature around 10 K. The NbTi cylinder is shown in Fig. 2.5a. The pulse chip is mounted in the bottom of the cell using GE varnish. Copper ribbons are soldered to gold pads on the pulse chip to connect them to 0.047 inch semi-rigid coaxial cables with copper inner and outer conductor and a PTFE dielectric.

The qubit chip is varnished to a custom built NbTi chip carrier. The chip carrier contains bonding pads patterned on a set of 1/32 inch thick PC boards made of FR-4. The qubit chip is wire bonded to the bonding pads which are soldered to copper wires that come through the back of the carrier and then exit the cell through a hole in the lid.

The pulse cell is designed so that the two chips can be aligned to within 1 $\mu m$. The chips are aligned in a special setup that allows the chips to be moved relative to each other while viewing the alignment from hole in the bottom of the cell. There are two set of verniers patterned on each chip during fabrication. Since the pulse chip is fabricated on a quartz substrate, its vernier can be viewed from the back of the chip while the qubit chip can be manipulated by a post screwed into a tapped hole on the back of the qubit chip carrier. The pole is attached to a series of micrometers that control the x, y and z axis motion while the sample cell is held in a modified mirror mount which can be used to cancel rotations. A microscope is attached to a CCD camera to view the chips while they are manipulated by the control system. Four set screws lock the two chip into position once the chips are aligned.

Once the chips are aligned the sample cell can be assembled. The lid slides into position down Teflon tubes that protect wiring from any kinking or sharp edges. All holes are designed so that the radius is more then ten times smaller then the length [21]. This stops flux changes from penetrating into the cell by attenuating the flux changes down to insignificant levels.

The NbTi sample cell acts as a magnetic shield only when the temperature is below the $T_c \approx 10K$ of NbTi. If there is a magnetic field present when the cell goes through its transition, it tends to trap the flux in the cell. In order to avoid flux trapping and to provide more protection from magnetic fields, a double layer Cryoperm shield is mounted to the mixing chamber of the dilution refrigerator outside the outer sample can. The Cryoperm shield is demagnetized below 77 K when its magnetic shielding is optimum but above the $T_c$ of the sample cell.

### 2.2.4 Outer Sample Can

The NbTi sample cell is designed to mount inside a vacuum tight sample can, shown in a drawing in Fig. 2.6 and in a picture without its bottom in Fig 2.5b. The sample can has two chambers separated by an rf tight block housing specially designed high frequency microstrip filters. The NbTi cell mounted in the bottom chamber is protected from rf signals by the filter block. Coaxial cables and twisted pairs enter the cell through vacuum tight epoxy feedthroughs (Stycast 2850 FT) mounted in the lid. The lid and bottom can are sealed to the center can using indium o-ring seals.

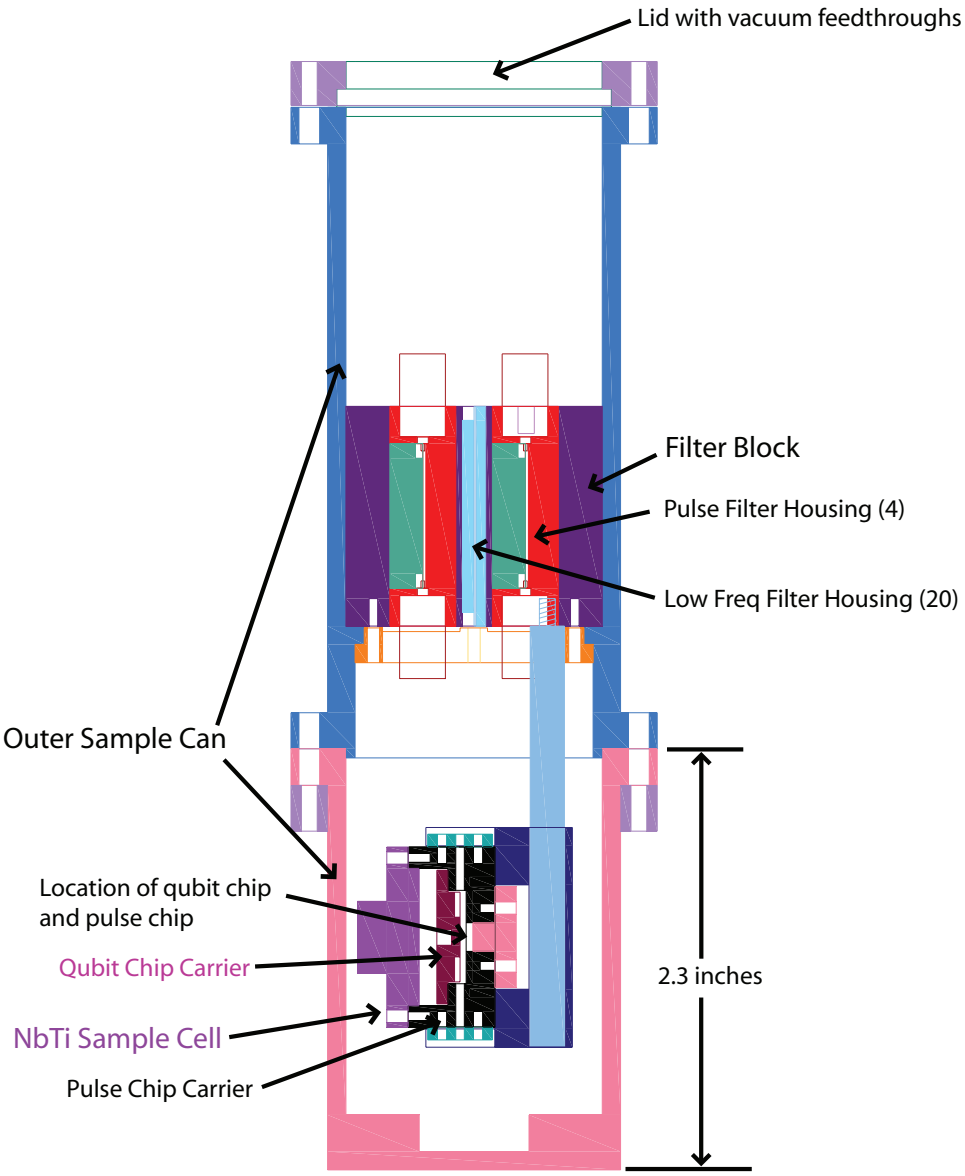


Figure 2.6: Drawing of a cross-sectional view of the assembled outer sample can and NbTi sample cell

The sample can is mounted on the sample stage of a dilution refrigerator, shown in Fig 2.5c, capable of reaching a loaded base temperature of 5 mK. The sample can is vacuum tight, so that it can be filled with $He^4$ which goes superfluid at low temperature and should provide thermalization of the qubit chips and microstrip filters similar to an exchange gas.

## 2.3 Bias and Control

The room temperature circuits have been optimized to control and measure the qubit while protecting it from noise. Timing between the various sources is critical to the operation and readout of the qubit. The measurement and control lines can be broken down into the low frequency lines and the high frequency transmission lines. The low frequency connections include the magnetometer control and measurement and the three flux biases; magnetometer ($\phi_B$), $\phi_x$ and $\phi_{xdc}$. The high frequency control lines are on a separate chip suspended over the qubit chip and supply further control of $\phi_x$ and $\phi_B$.

### 2.3.1 Grounding and rf Shielding

In order to avoid ground loops and noise pick up, the whole experiment is designed to have a single ground [58, 59]. All connections to the chip are floating and are only capacitively coupled to ground though the filters. All current paths are designed to be symmetric with respect to the chip to reduce the effect of common mode noise [59]. All grounded signal sources pass through battery powered unity gain isolation amplifiers that effectively disconnects this signal from the earth ground. These amplifiers are designed with 100 $M\Omega$ of resistance between their inputs and the common of the battery circuit [59]. This allows for sufficient decoupling from the ground while keeping the amplifier from saturating due to charging by providing a return current path. The amplifiers use OPA111 [60] low noise Difet operational amplifiers and a INA105 output stage. Connections from these "isolated sources" to the connection box are made using shielded twin-axial cables. The connections from the connection box to the EMI filters at the top of the dilution refrigerator are also well shielded. All signals entering the fridge are isolated, shielded and filtered allowing the dilution refrigerator itself to act as an rf-shield for the cold portion of the experiment.

### 2.3.2 Filtering

In order to see effects such as quantum coherence and Rabi oscillations, the qubit must be well isolated from the environment. All measurement and control lines must be heavily filtered to reduce the level of noise from room temperature electronics. The low frequency lines are filtered by EMI filters at room temperature, followed by cascaded RC filters anchored at 1 K, followed by specially designed microstrip filters at base temperature. The high frequency lines (both pulse and microwave) are filtered by a series of attenuators at 1.4 K (20 dB), 600 mK (10 dB) and at base temperature (10 dB) followed by microstrip filters that cutoff around 1 GHz.

Common RC filters only work up to some resonant frequency (usually less than 1 GHz) due to the parasitic inductance of the capacitor [61]. Appendix B gives details on filters specially designed to cutoff strongly and work to much higher frequencies. They consist of a thin film of chromium deposited on a substrate and diced into long narrow chips. When the chips are placed in a brass housing, which acts as a ground plane, they form a lossy microstrip transmission line. The filters that must pass dc current also have a Nb meander line to pass the low frequency control currents without heating the filter assembly.

### 2.3.3 Magnetometer Bias and Readout

The flux state of the qubit is readout using an on-chip hysteretic dc SQUID magnetometer. The flux from the qubit couples to the magnetometer changing the switching current. The details of the design and operation of the magnetometer are described in Appendix A. The switching current measurements require the ability to bias the magnetometer at various currents, ramp the magnetometer with a controlled linear ramp, reset the magnetometer by going to zero bias and be synchronized with the qubit operations. This is accomplished using an arbitrary waveform generator, Tektronix AWG430. The AWG430 supplies a programmable waveform of up to 16,200,000 points at clock frequency up to $200 \times 10^6$ samples per second with 16 bit voltage resolution corresponding to 75 $\mu V$ steps. With our bias resistors, this gives 0.75 nA step size for the current ramps. The signal from the AWG goes though an isolation amplifier to the bias box, which consists of biasing and sensing resistors. The bias resistors, usually 100 $k\Omega$ are used to limit the current to the range necessary to observe the switch to the voltage state, on the order of 10 $\mu A$. The sensing resistor, also 100 $k\Omega$, is chosen to give the maximum current sensitivity while keeping the voltage below the 1 V maximum input of our sense amplifiers. The sense amplifiers for all bias currents are Stanford

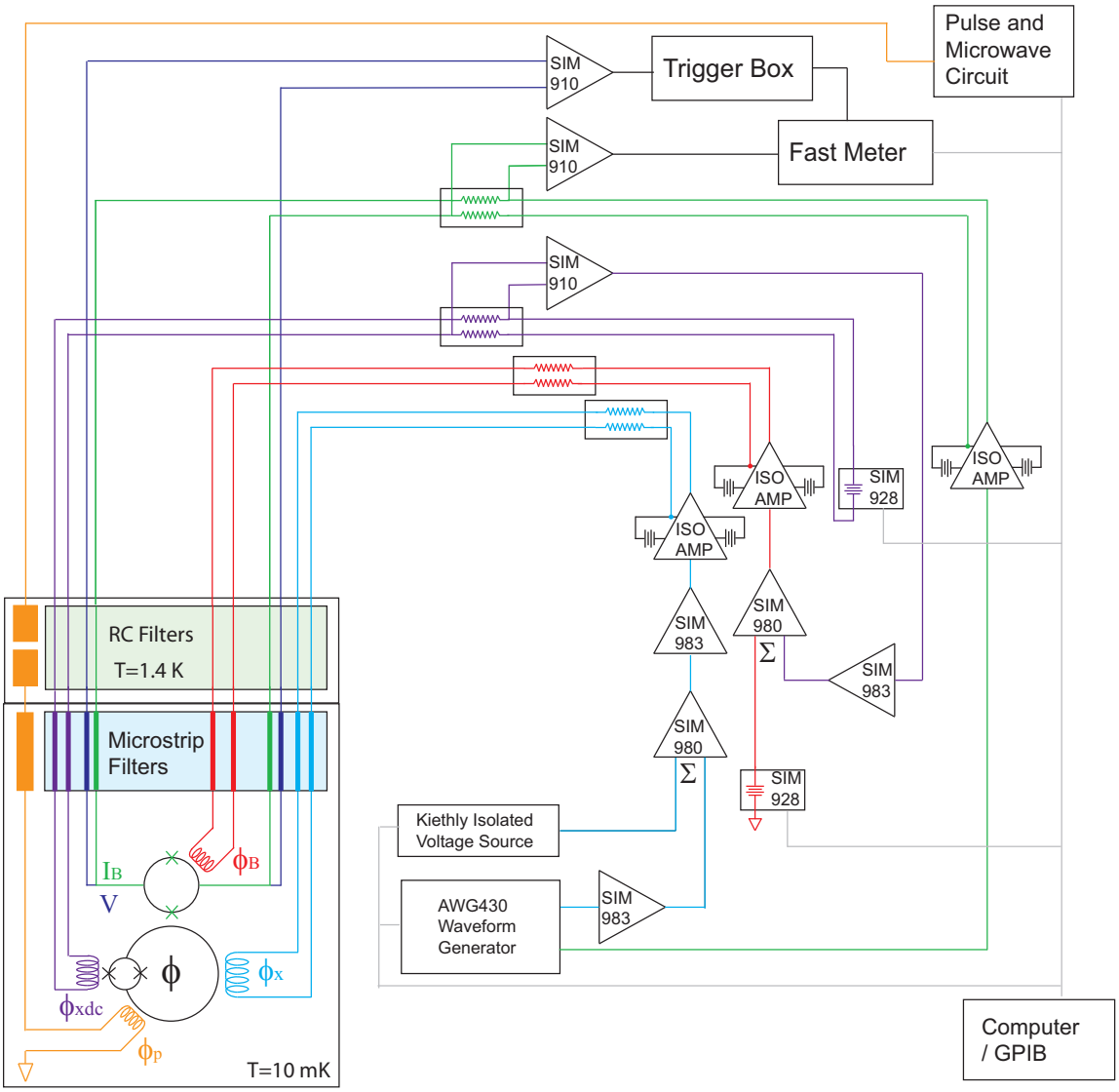


Figure 2.7: Schematic of measurement electronics

Research Systems SIM910 JFET amplifiers operated in differential mode. Besides providing gain, these amplifiers isolate measurement electronics, such as voltmeters and oscilloscopes, from the bias circuitry. These amplifiers were chosen because they are programmable and reasonably priced while having sufficient bandwidth, DC to 1 MHz, and sufficiently low input noise, $4nV/\sqrt{Hz}$ at 1 kHz.

The voltage from the sensing amplifier is measured using a fast multimeter (HP 3458A). This multimeter is used for its ability to measure with high precision at a fast rate when triggered. For a resolution of 1 $\mu V$ the integration time is 10 $\mu s$ with a trigger bandwidth of 5 MHz corresponding to current sensitivity of approximately 20 nA at a current bias ramp rate of 2 mA/s. The voltage value is retrieved by the computer from the multimeter via the GPIB. When the magnetometer switches to the voltage state it is sensed by a threshold detector. One of the sensing amplifiers is used to bring the voltage into a comfortable range for the threshold detector and to isolate the magnetometer from the threshold detector. The signal from this amplifier is also used to observe the current versus voltage characteristic of the the magnetometer. The digital pulse from the threshold detector triggers the multimeter measuring the switching current.

### 2.3.4 $\phi_{xdc}$ Flux Bias

The barrier between the two fluxoid states is adjusted by applying flux using $\phi_{xdc}$. The source is a programmable battery powered isolated voltage source, Stanford Research Systems SIM 928. The voltage is applied directly across bias resistance of 1 $k\Omega$. The current is measured by recording the voltage through a sensing amplifier across the 250 $\Omega$ sense resistor. This voltage from the sense resistor is also added to the magnetometer flux bias to compensate for the coupling between $\phi_{xdc}$ and the magnetometer.

### 2.3.5 Magnetometer Flux Bias

The switching current of the magnetometer is modulated by passing current through the magnetometer's flux bias ($\phi_B$). The circuit basically consists of a programmable voltage source, an isolation amplifier and the bias resistors. However as mentioned in the previous section, if $\phi_{xdc}$ is changed then $\phi_B$ must be adjusted to compensate. This is accomplished by taking the voltage from the $\phi_{xdc}$ sensing amplifier, scaling it to the necessary voltage using a Stanford Research System SIM 983 and summing it with the programmable voltage using Stanford Research System SIM 980. The gain of the scaling amplifier

is adjusted until there is no change in the switching current for an arbitrary change in $\phi_{xdc}$.

### 2.3.6 Qubit Flux Bias

The qubit flux bias ($\phi_x$) requires the ability to accurately set and step the current while providing fast accurate pulses to measure the escape rate. In order to accomplish both these tasks a Keithley 213 voltage source is used for the dc bias while one of the channels of the Tektronix AWG 430 is used to create the necessary pulses. The voltages from these two sources are summed using Stanford Research System SIM 980. The signal from the AWG 430 is attenuated using a SIM 983 scaling amplifier in order to use the largest range, hence the most voltage steps of the AWG. The initialization of the qubit does not require accurate timing and can be programmed into the voltage output of the Keithley 213. A SIM 983 scaling amplifier is used after the summer to provide an adjustable offset. The composite signal is sent into a isolation amplifier and finally into the bias box. A pulse from a different channel of the Keithley is used to synchronize the Keithley and the AWG 430 while the Keithley is software triggered.

### 2.3.7 High Frequency Qubit Flux Bias

Due to the heavy filtering on the flux bias lines, microwaves and fast flux pulses are coupled to the qubit using a separate chip suspended over the qubit chip with high frequency transmission lines. The signals are transmitted from room temperature to the cell using semi-rigid coaxial cables. The filters and attenuators are explained in Sec 2.3.2 and Appendix B.

In some of the measurements, flux pulses and microwaves need to be used on the same bias line at the same time. A directional coupler, Agilent 8730C, is used to combine the microwave pulses with the fast flux pulses. The fast flux pulses are input through the directly coupled port, known as the output port. The microwaves are coupled through the -10 dB indirectly coupled port. This port only couples to the other ports when the signal is between 1 and 26 GHz. The directivity of the coupler allows the signals to be combined without reflections distorting the pulses. The combined signal is output through the final port, usual called the input port.

The fast flux pulses are produced by a Tektronix Data Timing Generator (DTG 5274). The DTG can produce very short pulses with rise times as short as 200 ps and voltages as large as 2.7 V. The microwave filters and the lossy semi-rigid coaxial cable are the limiting factor for the length of the pulse that can be coupled to the qubit. The attenuators and filters reduce the voltage

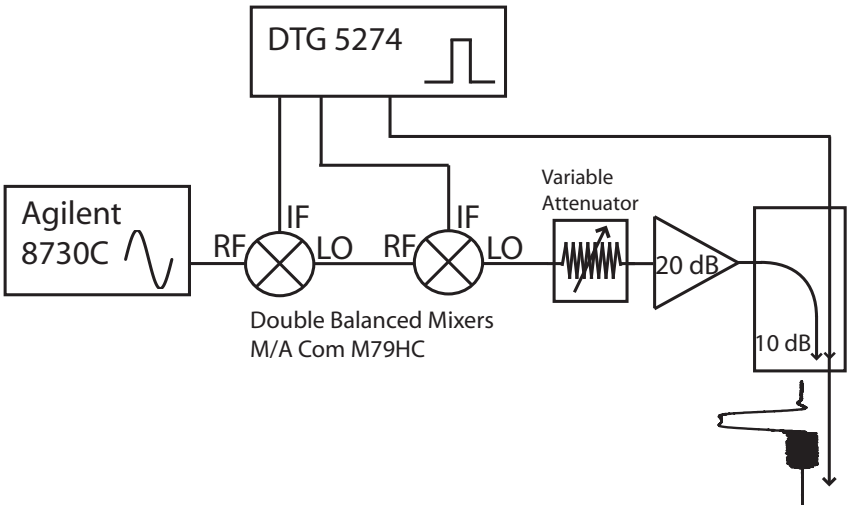


Figure 2.8: Schematic of the microwave components used to create the microwave pulses and combine them with the fast flux pulses.

by a factor 55 dB by the time the pulse crosses the microstrip line. The 50 Ω coaxial terminator at the end of the line is made from a $NiCr$ alloy, which does not go superconducting in the range of these measurements (10 mK). The flux coupled to the qubit is calibrated with respect to $\phi_x$ by comparing how the signals affect the qubit.

The measurement of Rabi oscillations requires short well controlled pulses of microwaves at the frequency of the energy splitting between levels. These microwave pulses are created by using double balanced mixers to shape pulses from a continuous microwave carrier at the desired frequency [62]. The amount of signal passing through the mixer from the RF port to the local oscillator (LO) port is a function of the current at the intermediate frequency (IF) port [63]. Maximum attenuation occurs when no current passes through the IF port. The attenuation decreases with increasing current until the mixer is saturated. Rise times less then 1 ns can be achieved using double-balanced mixers. The RF and LO ports must be coupled in the frequency range of the carrier while the IF port must be coupled all the way down to dc. The 1 dB conversion point of the mixer determines the maximum microwave power.

Figure 2.8 shows the setup for creating and combining the microwave and flux pulses. Microwaves from 1 to 20 GHz with power up to +15 dBm are created using a Agilent 8730C. The envelope pulse with amplitudes as large as 1.2 V is generated by a data timing generator, DTG 5274. The two signals are combined using a M/A Com M79HC heterodyne mixer. A second identical mixer is used to increase the ratio of the "off" to "on" state of the mixer.

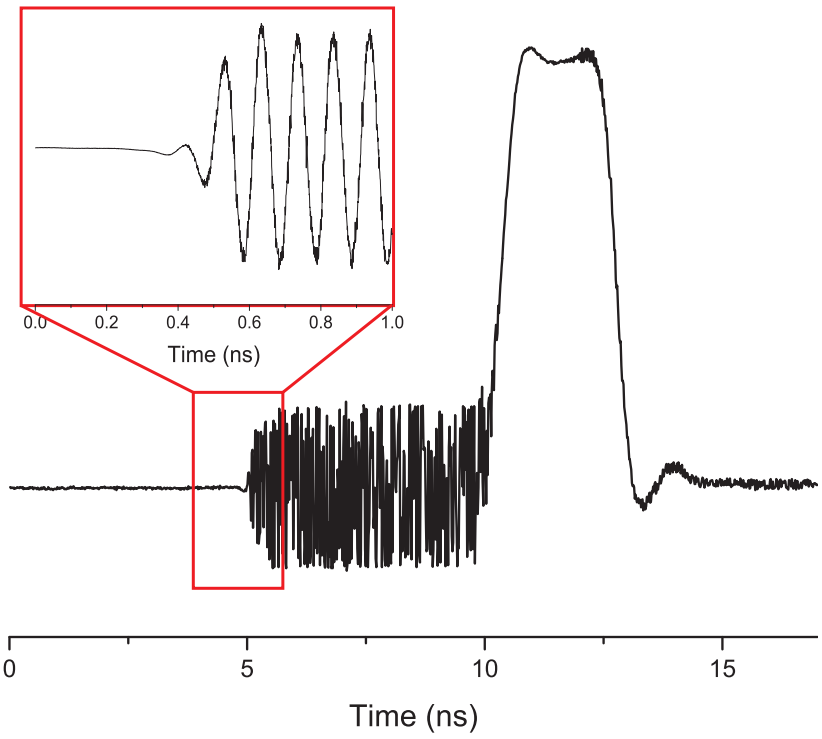


Figure 2.9: Measurement of the combined microwave pulse and fast flux pulse after the directional coupler. The variation of the microwave pulse is caused by the sampling rate at the larger time step of the scope. The inset shows the beginning of the microwave pulse at a higher sampling rate with the microwave generator and scope synchronized. The rise time of the microwave pulse is around 200 ps.

The envelope pulse of the second mixer is delayed until the optimum pulse is archived as observed using a Agilent Infinium DCA-J 86100C sampling scope. The delay compensates for the time difference between when the pulse was created in the first mixer and the time when it enters the second mixer. The voltage of the envelope pulses is adjusted until the cleanest pulse is achieved. A dc block is used after the mixers to eliminate any potential dc signal. Variable attenuators are used to adjust the amplitude of the microwave pulse. The combinations of the two variable attenuators gives steps of 1 dB between 0 dB and -81 dB. A microwave amplifier (Miteq AMF-3D-020180-60-15P) increases the microwave amplitude by 20 dB. The gain flatness of the amplifier is $\pm$ 1.5 dB and must be considered when performing frequency sweeps. After the amplifier, the microwave pulses are combined with fast flux pulses through the indirectly coupled port of the directional coupler. The microwave pulse and fast flux pulse are shown together in Fig 2.9.

## 2.4 Measurement Process

### 2.4.1 Introduction

A problem arises when it comes time to measure the flux state of the qubit. Measurement of the qubit requires that it is coupled to some measurement device. However by definition the measurement device is part of the environment and therefore a source of decoherence. A hysteretic dc SQUID magnetometer is used for the measurement because it represents a reasonable compromise between accurate measurement of the flux state and low back action onto the qubit. The magnetometer is in its supercurrent state until the measurement is performed. After the state is measured, the magnetometer produces a large amount of quasiparticles destroying the coherence of the qubit. However once the measurement is performed the state of the qubit is irrelevant.

It is possible to perform dispersive measurements that do not completely destroy the coherent states of the qubit. These measurements have the potential for higher fidelity and open up the possibility of quantum non-demolition measurement. One of these methods uses rf techniques to measure the difference in the inductance of the dc SQUID magnetometer while in the supercurrent state, for different flux states of the qubit [64]. Alternatively, Schoelkopf's group at Yale has shown improved measurement fidelity by capacitively coupling their charge qubit to a transmission line resonator and measuring the phase shift of microwave photons passing though the resonator [43]. They have been able to perform experiments analogous to those of cavity quantum electrodynamics. It should be possible to apply a similar technique to readout

flux qubits. However these techniques usually require many measurements to determine the state of the qubit and have not significantly improved qubit coherence times.

The large flux difference between the fluxoid states allows weaker coupling hence less back-action than some other qubit designs, for example the three junction persistent current qubit. As explained in detail in Appendix A, the magnetometer used for these measurements was specifically designed to further reduce noise due to fluctuations in the necessary bias current. Appendix A will focus on the specifics of this design while this section will explain how the magnetometer is used to measure the fluxoid state of the qubit. The last sections of this chapter will describe how the magnetometer is used with a fast $\phi_x$ pulse to measure the escape rate out of a metastable flux state, which can be used to measure the occupation of an excited state in a given well.

### 2.4.2 Switching Current Measurement

The flux state of the qubit is measured using the hysteretic dc SQUID magnetometer [65, 66]. The switching current of the SQUID is a function of the flux through the SQUID loop. By inductively coupling the magnetometer to the qubit, a change of flux in the qubit results in a corresponding change in the switching current.

The exact parameters of the magnetometers change from sample to sample but they are all fairly similar. This description will focus on a representative magnetometer that was used for a majority of the measurements. The fabrication of the junctions is described in Sec 2.1. The inductance of the magnetometer is calculated to be 56 pH [54]. A schematic of the voltage across the junctions as a function of the bias current, for a typical dc SQUID magnetometer is shown in Fig. 2.10.

The bias current of the magnetometer is ramped from zero to some bias current higher than $I_{sw}$. When the current reaches $I_{sw}$ the voltage goes from zero to some finite value determined by the shunt resistance. The shunt resistance is added to stop the magnetometer from switching to the superconducting gap, creating excess quasiparticles. The voltage is sent to a threshold detector, also known as trigger box, with the trigger level set at some voltage between zero and the voltage value corresponding to the shunt resistance at $I_{sw}$. The trigger box then sends a signal to trigger a fast volt meter that records the voltage across a current bias resistor. The $I_{sw}$ is measured many times in order to get enough statistics to extract the mean and first moment of the distribution. Figure 2.11a shows typical raw data for half a million switches with a ramp rate of 2 mA/s taken every 10.0 ms at a $\phi_x$ such that the qubit has equal probability of being in left well or the right well. Figure 2.11b shows a histogram

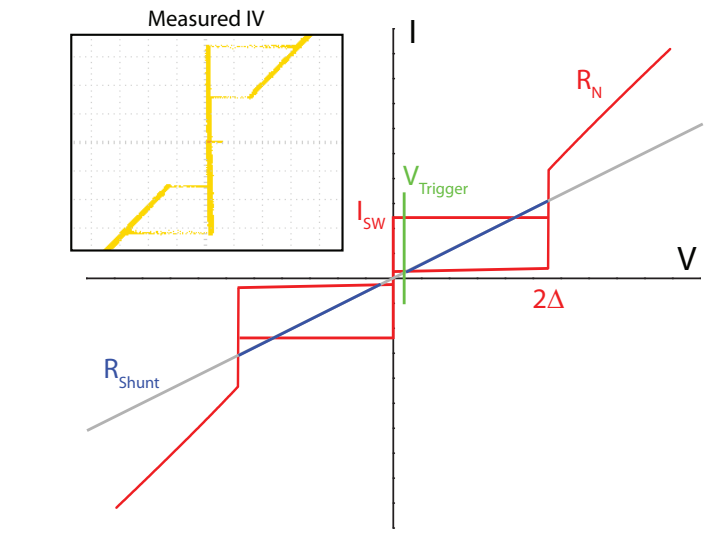


Figure 2.10: A schematic representation of a the bias current (I) versus voltage (V) across a hysteretic dc SQUID magnetometer. The red line is the IV without the shunt resistor while the blue line shows the effect of the shunt resistor. The inset shows the measured IV of the magnetometer for bias currents close to zero.

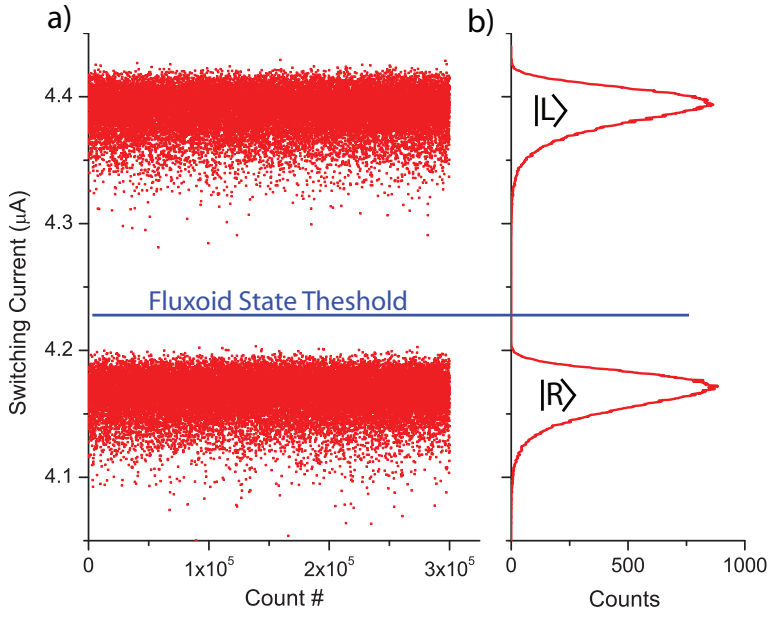


Figure 2.11: a) Example of switching current measurement repeated every 10 ms. b) A histogram of the data showing the separation of the distribution corresponding to the different flux states.

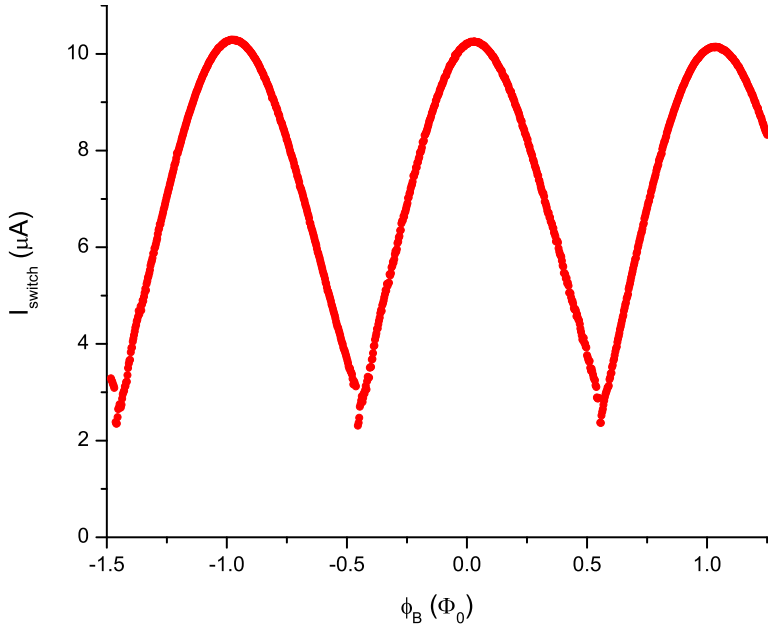


Figure 2.12: The measured mean switching current of the magnetometer as a function of flux applied from $\phi_B$.

of the data demonstrating the difference in switching current between the two flux states. At this $\beta_L$ the state of the qubit is determined in a single measurement by checking if the switching current is a above or below the threshold value set between the two states.

The measured switching current of the magnetometer as a function of flux applied from $\phi_B$, known as a transfer function, is shown in Fig. 2.12. The maximums of the transfer function are separated by one flux quantum. This data can be used to convert switching current measurements to flux through the SQUID loop. When the magnetometer is operated in a linear section of the transfer function, the switching current of the magnetometer is proportional to the flux though the magnetometer loop and therefore proportional to the flux change in the qubit.

### 2.4.3 Measuring Flux in the Qubit

All of the information about the qubit is obtained via measurements of its flux. For some measurements it is important to know the mean flux of the qubit. For other measurements the flux is only used to determine if the qubit is in the right well or left well of the potential. In either case the, flux is the macroscopic observable that allows measurement of the quantum mechanical

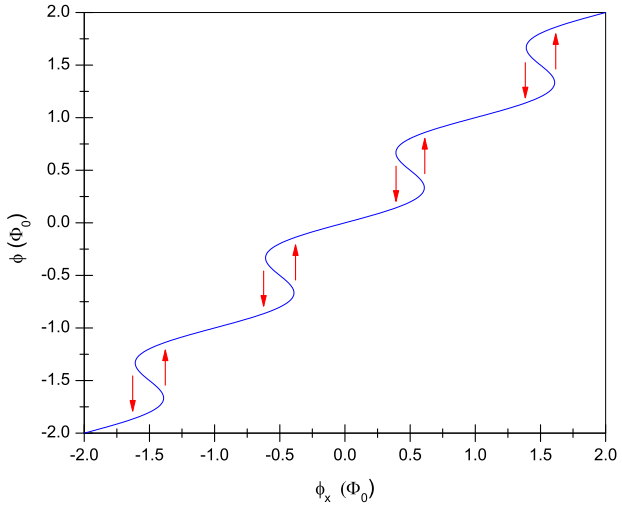


Figure 2.13: A calculation of $\langle\phi\rangle$ as a function $\phi_x$ for $\beta_L = 2$.

state. For an rf SQUID, the total flux in the loop is given by [65].

$$\phi = \phi_x - \beta_L \sin(\phi) \tag{2.1}$$

where $\phi$ and $\phi_x$ are referenced to zero flux quantum. This equation is plotted in Fig 2.13 with a $\beta_L = 2$. The portions of the curve with negative slope are unstable. In these regions the qubit has two possible states, given by two different branches with positive slope. The flux value the qubit chooses depends on its previous history. The size of the resulting hysteresis loop for the $\phi(\phi_x)$ curve is a function of $\beta_L$ and therefore $\phi_{xdc}$.

Figure 2.14 shows an example of the measured average switching current in the magnetometer as a function of the external flux applied to the qubit. The switching current is proportional to $\phi$ at a given $\phi_x$. The separation between consecutive loops corresponds to a flux quantum in the qubit. This is used to convert from current in the $\phi_x$ loop to flux applied to the qubit. The loops are measured by pulsing $\phi_x$ in one direction outside the loop for a 1 ms to initialize the state of the qubit. The flux is measured before the system can hop over the barrier due to temperature or noise. For the other branch, $\phi_x$ is pulsed the other way to initialize it in the other branch. Chapter 3 goes into detail on how measurements of the mean flux can be used to determine the parameters of the qubit.

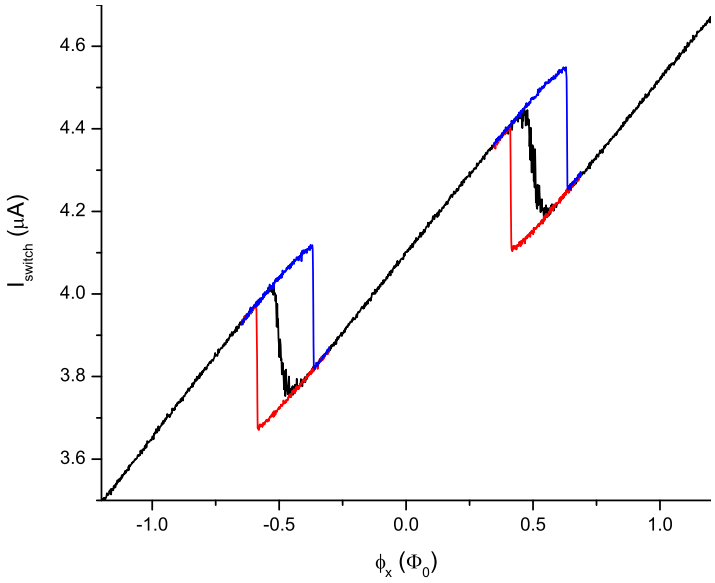


Figure 2.14: A measurement of the mean switching current ($I_{switch}$) of the magnetometer as a function $\phi_x$. $I_{switch}$ is proportional to the $\langle\phi\rangle$. The black line is for no initialization while the red (blue) lines are for an initialization pulse to right (left) to a point outside the loop.

## 2.5 Measuring Escape Rates

The dynamics of the qubit between flux states in different wells of the double well potential are probed by measuring the escape rate out of a metastable state in one well into the other. The metastable state is not the ground state of the system, but the ground state within a given potential well. Depending on the size of the barrier separating these two states, the lifetime of the metastable state can be much longer than any time scale in these experiments. The rate of escape from this state can be measured by pulsing the flux to $\phi_x$ at which the escape rate is to be measured and leaving it there for some time $t_m$, in which it has some reasonable probability of tunneling though the barrier into the other flux state. If the state that the system tunnels into is not the ground state then it can either relax to a lower state in the same well or tunnel back though the barrier. If the relaxation rate is much faster than the tunneling rate, then the system will relax to the ground state in the new flux state and remained trapped.

The measurement process is shown in Fig. 2.15 along with a cartoon representing the potential at that point. The system starts with a symmetric potential with a barrier high enough that the tunneling rate between wells is

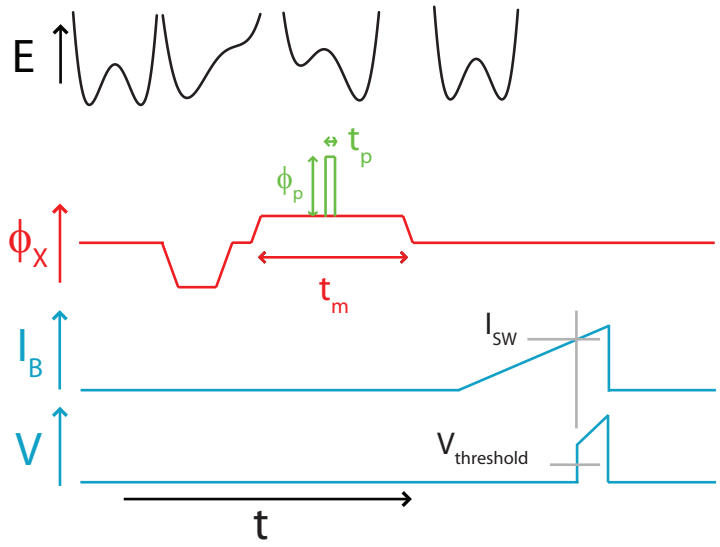


Figure 2.15: Measurement process of escape rates utilizing the flux pulse from the microstrip transmission line. The combined $\phi_x$ signal is shown along with the resulting qubit potential. The fluxoid state is measured by recording the value of bias current ($I_B$) at which the magnetometer switches to the voltage state.

much longer then the duration of the measurement. First the qubit is initialized by tilting the potential, fixing the flux state in the left well. The potential is then tilted the other way, far enough that there is some probability of tunneling through the barrier to the right well. The potential is left there for time $t_m$ and then tilted back to a symmetric potential. The system is trapped in the state it was in while the magnetometer's bias current is ramped to measure the state of the system. This is repeated a few thousand times for each value of tilt. The escape rate $\Gamma_{escape}$ is determined from the probability of a transition, $P(\phi_x)$, for a given $t_m$, as a function of the tilt of the potential by

$$\Gamma_{escape}(\phi_x) = \frac{1}{t_m} \ln\left(\frac{1}{1 - P(\phi_x)}\right) \tag{2.2}$$

Due to its heavy filtering, the $\phi_x$ bias line does not support pulses faster then 0.5 ms. To measure rates faster then $10^4$, an extra pulse $\phi_p$ is coupled to the qubit using the high frequency transmission line. The pulse generator has larger voltage steps than the minimum $\phi_x$ step, so the two bias lines are used together. The $\phi_x$ pulse length is adjusted so that it does not affect the probability of tunneling and only serves to change the $\phi_x$ added to the pulse.

Figure 2.16 shows typical data for the escape rate as a function of $\phi_x$ using

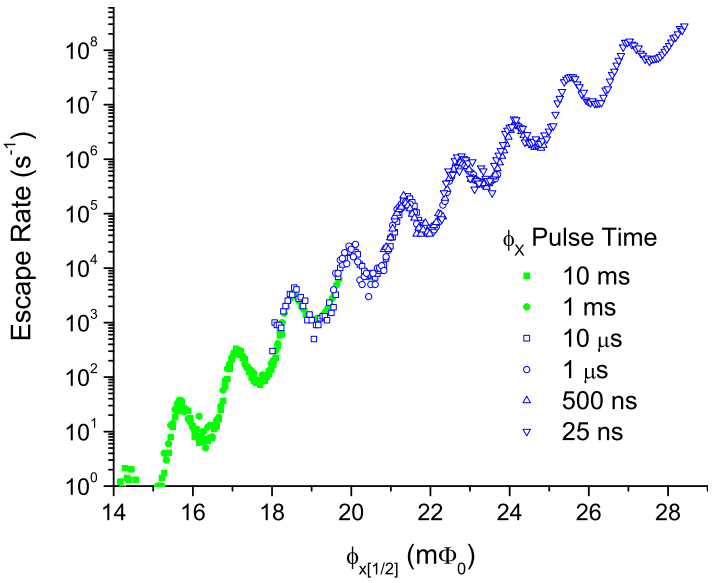


Figure 2.16: Measured escape rate from the ground state as a function of qubit flux bias, obtained with a flux pulse from the transmission line (blue open symbols) or from the bias coil (green filled symbols). The lengths of the flux pulses range from 25 ns to 10 ms.

pulses ranging from 25 ns to 10 $\mu s$ for a $\beta_L = 1.4$. The green filled points are taken just using the $\phi_x$ pulse while the blue open points are taken use both pulses. The peaks correspond to the lowest energy level in the left (upper) well crossing successive excited states in the right well (lower).

Figure 2.17 shows the escape rate as a function of $\phi_x$ for 10 ns flux pulses of different amplitudes. The data show that the fast flux pulse from the transmission line combines linearly with the flux from the bias coil. This allows for a calibration of the fast flux pulse relative to the $\phi_x$ bias coil. The bias coil is easily calibrated since it can provide several $\Phi_0$ of flux to go through multiple periods in $\phi_x$. The ability to control the amplitude of the flux pulse over a large range of $\phi_x$ allows the amplitude of the pulse to be used to compensate for changes $\phi_x$ in order to keep the background escape rate constant, which is useful for measurements in Chapter 4.

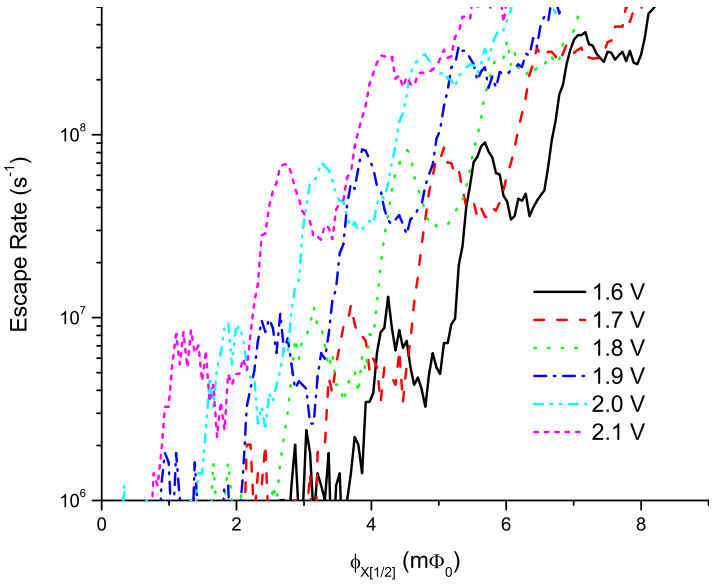


Figure 2.17: Measured escape rate into the other fluxoid state during a 10 ns flux pulse as a function of $\phi_x$ for different pulse amplitudes.

## 2.6 Measuring the Occupancy of the Excited State

In order to study the coherence between two states in the same well we need to be able to measure whether the system is in the ground or excited state. In order to accomplish this, a fast flux pulse is used to tilt the potential to a point where it has a high probability to tunnel into the other flux state during the pulse if it was in the excited state and a low probability to tunnel if it was in the ground state. Then by measuring the escape rate, as explained in the previous section, we can extract the occupation of the excited state. This technique is analogous to the current pulses successfully used to readout phase qubits [67, 68] and flux pulses used in current biased dc-SQUID qubits [69] in which the pulse tilts the potential and causes a transition to the voltage state for the excited state and not for the ground state.

The pulse needs to be short enough that the measurement occurs before the qubit has a chance to relax back into the ground state. For 5 ns pulses, the potential must be titled to the point where the barrier height is $\sim 1.1$ K. At this point, the escape rate from the excited state is 460 times that of the ground state. However if the lifetime of the excited state is long enough so that the readout pulse can be increased to 10 ns, this ratio of escape rates increases to 950 improving the fidelity to $\eta = 0.992$.

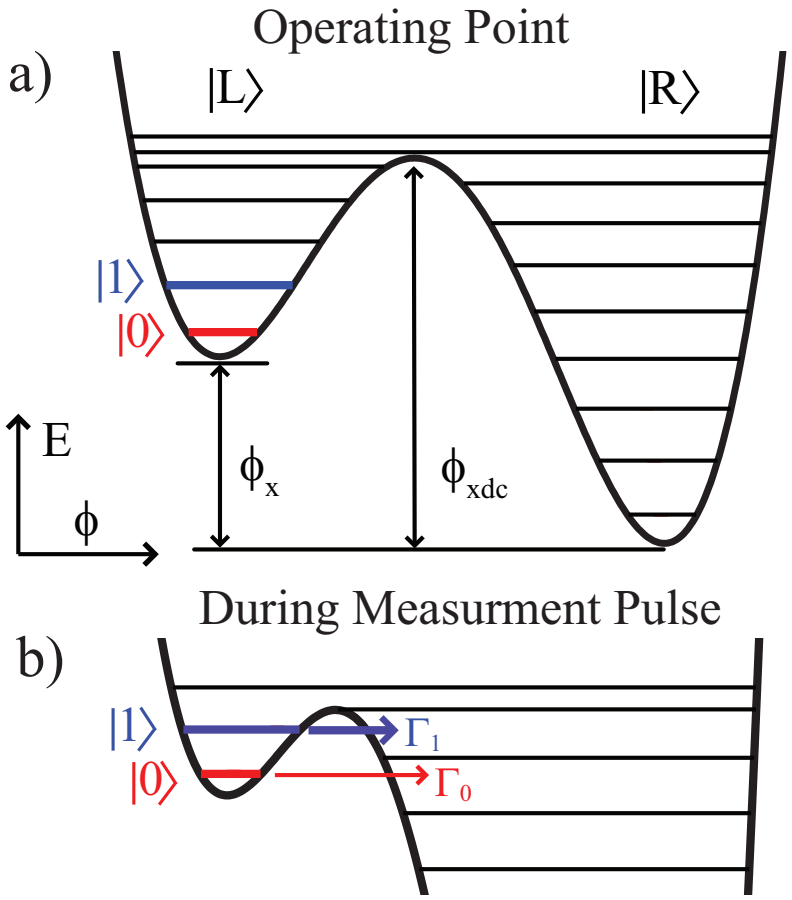


Figure 2.18: The potential and energy levels of a rf-SQUID qubit as a function of flux at a) the operating point and b) during the measurement pulse.

# Chapter 3

# Determining System Parameters

## 3.1 Introduction

Before proceeding with coherence measurements, various other measurements must be performed in order to accurately characterize the qubit. These measurements also serve as checks on our understanding of the qubit's Hamiltonian. Some of these measurements act as calibrations for the various controls of the qubit behavior while other measurements are used to determine the fundamental parameters of the qubit that are then used for calculations and data analysis.

The calibrations for $\phi_B$, $\phi_x$ and $\phi_p$ have been described in Chapter 2 and the calibration of $\phi_{xdc}$ is explained in Sec 3.2. The qubit parameters $\beta_L$, L and C were introduced in Chapter 1 and are calculated from various measurements described in the remainder of this chapter. Sec 3.4 explains the measurement of two other parameters, the ratio of the inductance of the qubit loops ($\gamma$) and the asymmetry of the qubit junctions ($\delta_{Ic}$), which are needed in order to make small corrections to calculations.

## 3.2 $\phi_{xdc}$ Calibration

Ideally $\phi_{xdc}$ would be calibrated like the other flux biases, by measuring the amount of current required to see a period of the modulation corresponding to a flux quantum in the loop. This could be accomplished by measuring the change in current between the two maximum widths of the qubit's hysteresis loop (Sec. 2.4.3). However since the coupling between the $\phi_{xdc}$ loop and its bias coil is smaller then the coupling for the other bias coils, its requires too much current to see a whole period of the modulation. The approximately 8 mA required would cause significant heating in the filter resistors, raising

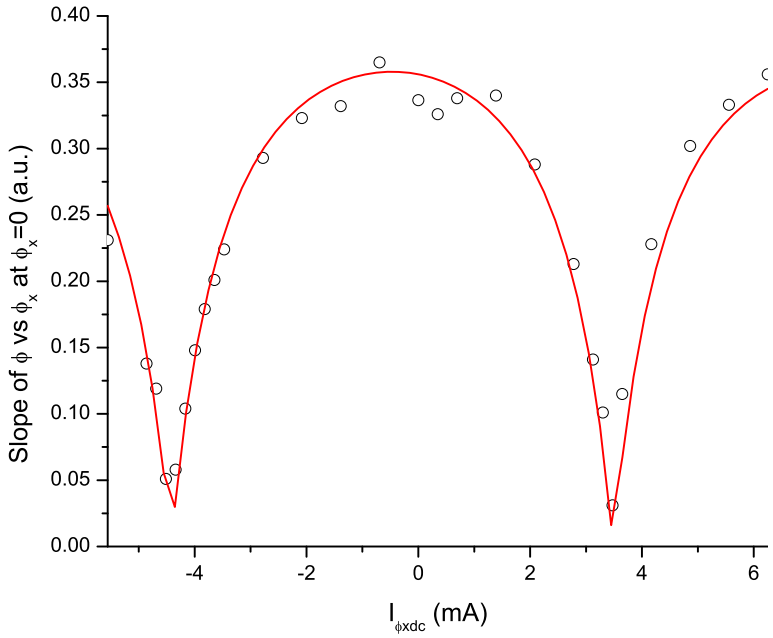


Figure 3.1: The slope of $\phi$ with respect to $\phi_x$ at $\phi_x = 0$ for various currents in the $\phi_{xdc}$ bias coil.

the temperature of the dilution refrigerator. Instead $\phi_{xdc}$ is calibrated by measuring the average $\phi$ as a function $\phi_x$. Equ. 2.1 gives the relationship between $\phi$, $\phi_x$ and $\beta_L$. Around $\phi_x = 0$, the small angle approximation is valid and equation Equ. 2.1 becomes

$$\varphi = \left(\frac{1}{1+\beta_L}\right)\varphi_x \tag{3.1}$$

Equ. 1.5 gives the relationship between $\beta_L$ and $\phi_{xdc}$. Inserting this into Equ. 3.1 and reorganizing we find

$$\varphi - \varphi_x = \left(\frac{1}{1+\beta_{L0}\cos(\phi_{xdc})} - 1\right)\varphi_x \tag{3.2}$$

The slope, term in parentheses, of this function at $\phi_x = 0$ is compared with the measured value to obtain the $\phi_{xdc}$ calibration.

Fig. 3.1 shows the slope of the measured $\phi$ as a function of $\phi_x$ at $\phi_x = 0$ in arbitrary units as a function of current in the $\phi_{xdc}$ bias coil. Since we are primarily interested in calibrating $\phi_{xdc}$ there is no need to convert the switching current of the magnetometer into flux. The magnetometer is operated in a linear region so that the flux in the qubit is proportional to the switching

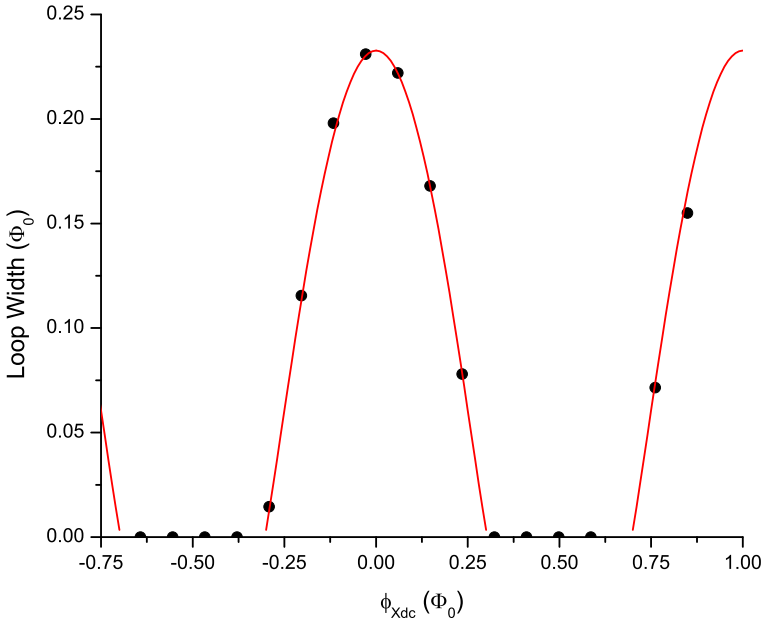


Figure 3.2: The measured width (black circles) of the hysteresis loop of the qubit as a function of flux from the $\phi_{xdc}$ bias loop along with the calculated width (red line) for $\beta_L = 2.29$ and $\Delta U = 5.4K$.

current. $\phi$ is measured over a couple of periods of $\phi_x$ in order to estimate the linear portion of the otherwise oscillatory function. The data is fit with the slope of Equ. 3.2 (solid line) with extra parameters to account for a shift in $\phi_x$ caused by trapped flux and an amplitude to account for the conversion from switching current to flux. The period of the modulation is found to be $7.89 \pm 0.04\ mA/\Phi_0$ with and offset of $-0.47 \pm 0.02$ mA. The scatter in the data is likely caused by error in the subtraction of the linear portion in the curve. This data can also be used to estimate $\beta_{L0} \approx 2.3$ but the uncertainty in this value is quite large since it depends strongly on another free parameter, the amplitude.

## 3.3 Size of Qubit Hysteresis Loop

$\beta_{L0}$ can be determined by measuring the width of the qubit's hysteresis loop, Sec 2.4.3, as a function of $\phi_{xdc}$. This analysis is based on the assumption that the fluxoid state of the qubit switches on average from the metastable state to the other state at the same barrier height. The timing between the initial pulse and the ramp of the bias current of the magnetometer is constant

and the ramp rate of the bias current is constant giving a constant sampling time in which the system can switch to the other flux state. The system switches on average at a barrier height that corresponds to a escape rate that would give a significant probability of switching.

For a given $\beta_{L0}$, the barrier height can be calculated using Equ. 1.3 for the $\phi_x$ value corresponding to the transition to the other fluxoid state. This value should be constant as a function of $\phi_{xdc}$ if the correct value of $\beta_{L0} = 2.29 \pm 0.09$ is used. Fig. 3.2 shows the measured values of loop width along with the widths calculated for a $\beta_{L0} = 2.29$ and a barrier height ($\Delta U$) of 5.4 K. The inductance only enters as a scale factor and does not have a noticeable effect on the determination of $\beta_{L0}$. This value is consistent with the value calculated using the design size and the critical current of cofabricated junctions.

## 3.4 Mean Flux

The effects of $\delta\beta$ and $\gamma$ are most clearly seen at values of $\beta_L < 1$ where there are no metastable states to complicate the issue. The system quickly relaxes to an equilibrium state independent of prior states. The potential parameters can be determined by measuring the mean $\phi(\phi_x)$ curve over a flux quantum for different $\beta_L$ [24] and fitting with calculations of the equilibrium value of $\phi$.

The mean flux is calculated by finding the minimum in the two dimensional potential of the modified rf SQUID. In terms of flux through the two loops the potential is given by [22]

$$\begin{aligned} U(\phi, \phi_{dc}) &= U_0[2\pi^2(\phi - \phi_x)^2 + 2\pi^2\gamma(\phi_{dc} - \phi_{xdc})^2 \\ &\quad +\beta_{L0}\cos(\pi\phi_{dc})\cos(2\pi\phi) - \delta_{Ic}\beta_{L0}\sin(\pi\phi_{dc})\sin(2\pi\phi)] \quad (3.3) \end{aligned}$$

where $\phi_{dc}$ is the flux in the dc SQUID loop, $\gamma \equiv L/\ell$ is the ratio of the inductances of the rf and dc SQUID loops and $\delta_{Ic} \equiv (I_{c2} - I_{c1})/(I_{c2} + I_{c1})$ is the junction asymmetry. For $\beta_L$ of the small loop much less than 1 and large $\gamma$, Equ. 3.3 reduces to the one dimensional potential with $\phi_{dc} = \phi_{xdc}$.

Figure 3.3 shows a measurement of $\phi - \phi_x$ as a function of $\phi_x$ for various values of $\phi_{xdc}$. The lines are the calculations using the minima of Equ. 3.3 with $\beta_{L0} = 2.2$, $\gamma = 19$ and $\delta_{Ic} = 0.016$. These parameters give the best fit of all the curves simultaneously over multiple periods of $\phi_x$. The largest sources of error arise from the subtraction of the linear portion of the curve and imperfect compensation for the switching current of the magnetometer due to direct coupling between $\phi_x$ and the magnetometer. The generally good fit between the calculations and the measurements are strong indications that Equ. 3.3 accurately describes the potential for this device.

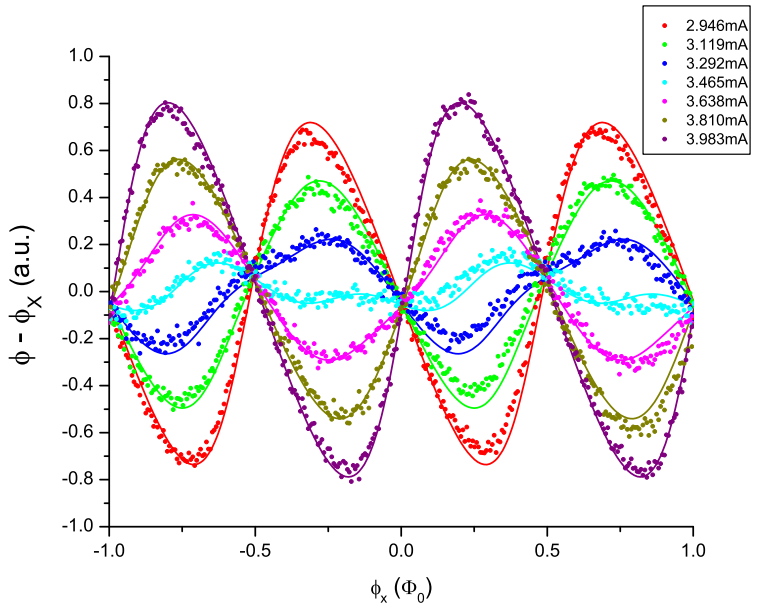


Figure 3.3: A measurement of $\langle\phi\rangle - \phi_x$ as a function $\phi_x$ at 7 different $\phi_{xdc}$ values. The lines are calculated by finding the minimum of Equ. 3.3 with $\beta_{L0} = 2.2$, $\gamma = 19$ and $\delta\beta = 0.016$.

The effect of changes in the different parameters manifest themselves differently in the mean flux. $\gamma$ provides the tilt of the curves away from a sinusoidal behavior and as it is increased it has less and less effect since the potential becomes more and more one dimensional. Since there is not much change in the potential for values of $\gamma$ greater then 16 the exact value of $\gamma$ is not known, but it is clearly in the one dimensional regime. The effect of $\delta_{Ic}$ is most obvious in the shift of the crossings of $\phi(\phi_x)$ for the different $\beta_L$ away from zero in one direction for integer values of $\phi_x$ and the other direction for half integer values. The $\delta_{Ic} = 0.016 \pm .005$ is consistent with the spread in junction size due to the fabrication process [53]. The $\beta_{L0} = 2.2 \pm 0.1$ is chosen to simultaneously fit all of the data using the $\phi_{xdc}$ values from the calibration in Sec. 3.2. The error in this value is partly due to the conversion of the switching current to flux in the qubit causing similar behavior to $\beta_{L0}$.

## 3.5 Escape Rates in Thermal Regime

The qubit inductance (L) can be estimated and $\beta_{L0}$ further refined by measuring the escape rate in the thermal regime where the slope of the rates as a function of $\phi_x$ depend on both the temperature and the height of the

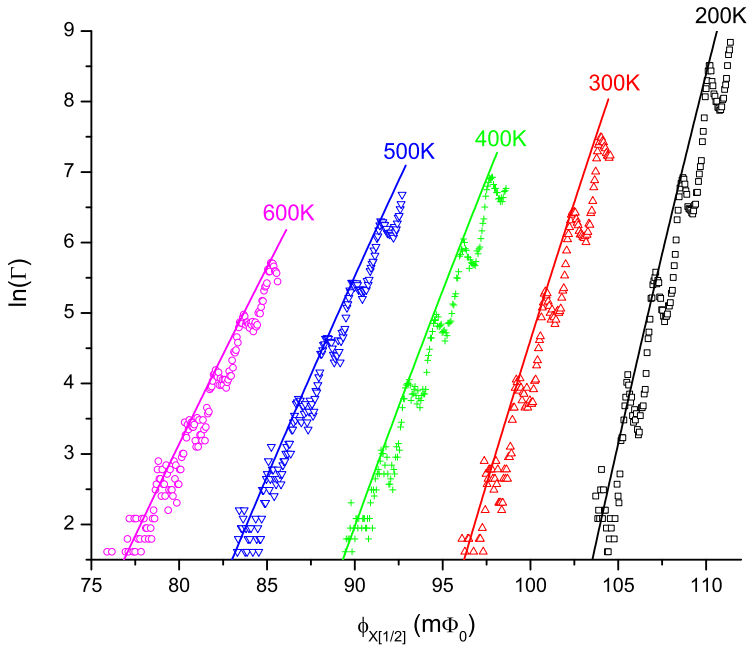


Figure 3.4: The natural log of the measured (points) and calculated (lines) escape rates as a function of $\phi_x$ at 5 different temperatures. The parameters for the calculated rates are $L = 188.5$ pH and $\beta_{L0} = 2.21$.

barrier between flux states. Kramers found that thermal activation over a potential barrier in a one dimensional potential has the form of Arrhenius law [70].

$$\Gamma = a_t \frac{\omega}{2\pi} \exp\left(\frac{-\Delta U}{k_B t}\right) \tag{3.4}$$

where $\Delta U$ is the barrier height, $a_t$ quantifies the dampening and $k_B$ is the Boltzmann constant. $\Delta U$ can be calculated as a function of $\phi_x$ using Equ. 3.3.

Figure 3.4 shows the natural log of the measured escape rates as a function of $\phi_x$ for 5 different temperatures; 200, 300, 400, 500, 600K. The temperatures are taken from a calibrated $RuO_x$ thermometer attached to the mixing chamber of the dilution refrigerator. For this temperature range, the mixing chamber temperature should be very close to the sample temperature. Also shown are the calculated thermal escape rates over the barrier at the various temperatures for $L = 189$ pH and $\beta_{L0} = 2.21$. The dampening parameter, $a_t$, mostly gives a vertical shift and therefore does not have much affect the slope. The oscillations in the data are level crossing between energy levels in different flux states of the double well potential. These level crossings can be

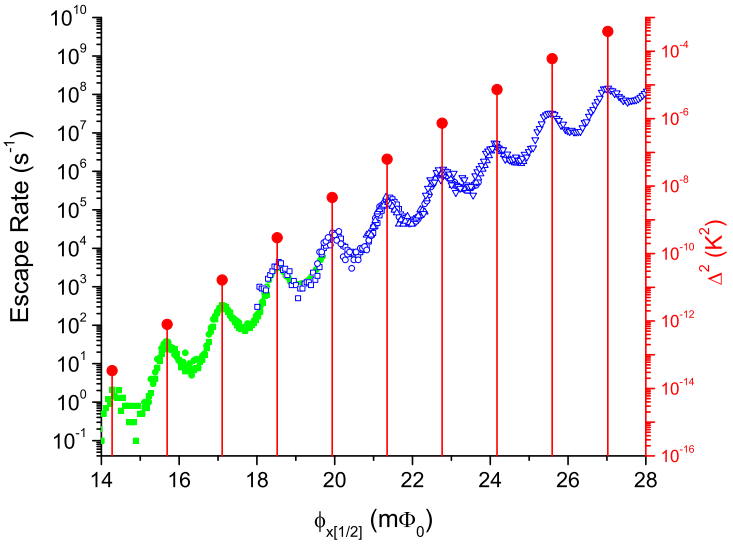


Figure 3.5: The blue open and green filled points(left axis) are the measured escape rates as a function of $\phi_x$. The red circles with the vertical lines (right axis) are the squared amplitudes of the calculated anticrossings between the ground state in the left well and successive excited states in the right well for $\beta_L = 1.412$ and $Z = 29.5$.

observed well above the crossover temperature between the quantum and thermal regime [21] but the overall slope does not appear to be affected. The fits to the data are consistent with the previously measured $\beta_{L0}$ and give $L = 189 \pm 15$ pH.

## 3.6 Z from Macroscopic Resonant Tunneling Peaks

The $\phi_x$ values where the resonant tunneling peaks occur depend strongly on $\beta_L$ and $Z = \sqrt{L/C}$. Using the previously measured values of $\beta_{L0}$, the measured escape rates can be compared to the level crossing calculated as explained in Sec. 1.3.2. Figure 3.5 shows measured escape rates, explained in Sec. 2.5, as a function of $\phi_x$ for the ground state in the left well crossing successive excited states in the right well starting at the 10th and going through the 19th energy level. The red circles correspond to the calculated level splitting squared at each crossing displayed on the right axis. The splittings are calculated by finding the successive local minimums of the energy difference between the anti-crossing eigenstates.

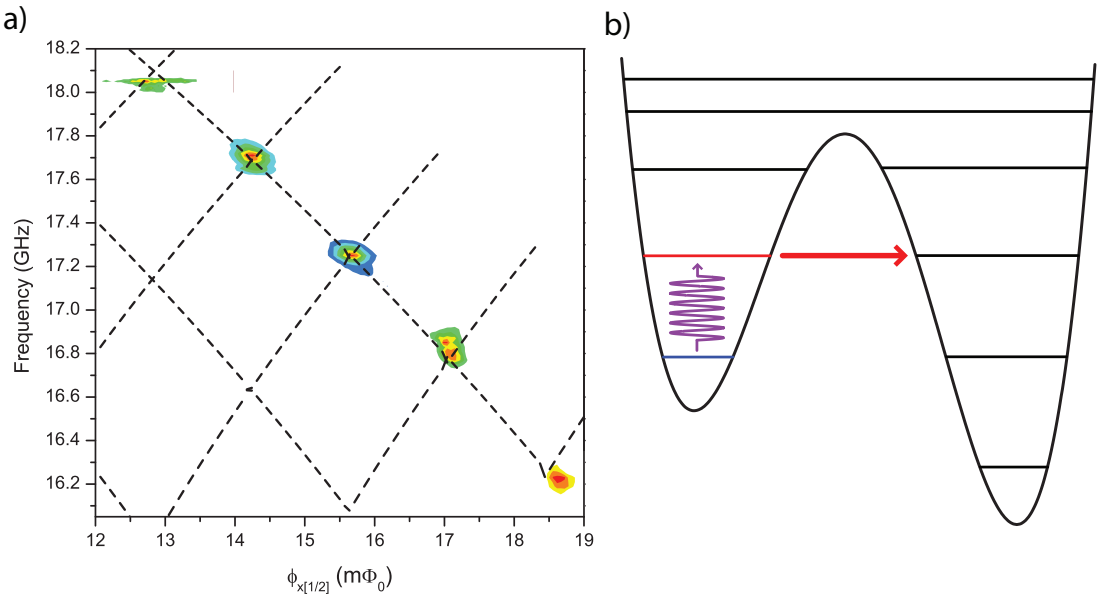


Figure 3.6: a) The measured escape rates of the PAT peaks shown as color contours (blue the lowest and red the largest) as a function of both $\phi_x$ and microwave frequency. The dashed lines are the calculated energy differences between consecutive eigenstates localized in the same well for $\beta_L = 1.412$, $Z = 29.5\ \Omega$ and $\omega_Q = 1.57 \times 10^{11} s^{-1}$. b) An energy level diagram showing the levels involved in photon assisted tunneling.

For a given $\beta_L$ there exists a Z that best matches the level spacing. However, due to the anharmonicity of the potential wells, the levels crossing are closer together near the top of the barrier. Hence the anharmonicity contains independent information on the value $\beta_L$. The $\beta_L = 1.412$ is consistent with both $\beta_L$ calculated from $\phi_{xdc}$ and $\beta_{L0}$ and the anharmonicity of this data. At this $\beta_L$, the best fit to the level crossing gives $Z = 29.5 \pm 0.4\ \Omega$.

## 3.7 $\omega_Q$ from Photon Assisted Tunneling

Photon assisted tunneling (PAT) refers to the use of continuous microwaves to pump the system into an excited state in the left well from which it can tunnel into the right well when the excited level aligns with one of the excited levels in the other well. The rate of tunneling into the other well is strongest when both the levels are aligned and the microwave frequency matches the level spacing between the ground and excited state in the left well. The level spacing between the ground and excited state strongly depends on $\omega_Q = (LC)^{-1/2}$ and

Table 3.1: Qubit Parameters

| **Parameter** | Value | Error | Primary Measurements |
|---|---|---|---|
| $\beta_{L0}$ | 2.21 | $\pm.08$ | Sec 3.4 and 3.5 |
| L | 189 pH | $\pm 9$ pH | Sec 3.6 and 3.5 |
| C | 217 fF | $\pm 8$ fF | Sec 3.7 and 3.6 |
| $\gamma$ | 19 | $-2, +4$ | Sec 3.4 |
| $\delta\beta$ | 0.016 | $\pm 0.005$ | Sec 3.4 |

$\beta_L$.

Figure 3.6 shows the PAT peaks as color contours as a function of both $\phi_x$ and frequency. The colors represent the measured tunneling probability with blue being the lowest and red being the highest. Using the values and uncertainties previously determined for the other parameters, the best fit to the data gives $\omega_Q = 1.57 \pm 0.1 \times 10^{11} s^{-1}$. The dotted lines give the calculated energy difference between consecutive eigenstates localized in the same well for $\beta_L = 1.412$, $Z = 29.5$ and $\omega_Q = 1.57 \times 10^{11} s^{-1}$. The positive sloping lines are the difference between energy levels in the right well while the negative sloping lines correspond to the left well. The PAT peaks should occur at the intersection between the top most negative sloping line and consecutive positive sloping lines. The peak around 18.05 GHz is cutoff due to the frequency constraints of some of the microwave components.

The calculation shows good agreement with the data and suggests that the measured parameters accurately describe the qubit Hamiltonian. The final parameters, shown in Table 3.1 are generally consistent with all the various measurements. Since different measurements are more sensitive to different parameters the measurements were used iteratively until a consistent set was found that showed the best overall agreement. Due to the iterative process and the many different types of measurement, it is hard to exactly predict the error associated with each parameter. The uncertainties in Table 3.1 are conservative estimates and could be further refined with more measurements over a larger range of flux bias.

# Chapter 4

# Measuring Coherence Times

## 4.1 Introduction

There are a number of different ways of characterizing the different coherence times in our flux qubit. Experimentally, the simplest method of probing the decoherence involves measuring the lineshape of macroscopic resonant tunneling between fluxoid states. However the dynamics that determine the tunneling process are complicated, especially when the width of the peaks are not much smaller than the spacing between them. The measurement flux pulse discussed in Sec. 2.6 makes it possible to measure the occupancy of the excited state and study intrawell dynamics. This along with controlled microwave pulses makes possible a direct measurement of the lifetime of the excited state and the observation of Rabi oscillations. Measurements on the coherence time between two states in the same well are less sensitive to flux noise and by measuring coherence times for these sates we can learn more about the type and level of noise affecting all levels.

## 4.2 Lifetime of the Excited State

The intra-well decay rate ($\Gamma_1$) provides an upper limit on the coherence of the qubit since all coherence is lost when the system decays. This rate can be measured directly by measuring the lifetime of the first excited state in a given well. This measurement is accomplished using microwaves to excite the qubit into the first excited followed by a fast flux pulse to readout the occupation of this state as a function of time. A long, 80 ns, microwave pulse is used in order to insure a consistent mixture of the ground and excited state. If enough microwave power is used this mixture would be close to half excited and half ground. However at these powers there is some chance of populating

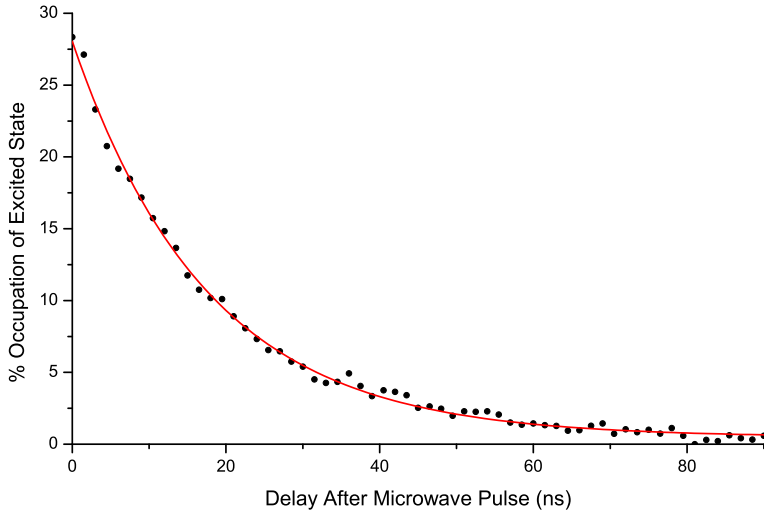


Figure 4.1: The measured occupation of the excited state as a function of delay between the long microwave pulse and the readout pulse. The line is a fit to the exponential decay used to extract $T_1$

the second excited state which should have approximately half the lifetime. Lower powers and hence less population in the excited state are used in order to avoid confusion in measuring the lifetime.

Figure 4.1 shows the occupation of the excited state as a function of delay between the end of the microwave pulse and the readout pulse. The microwave frequency of 17.9 GHz was on resonance with the energy difference between the ground and excited state at a $\phi_x = 0.05\ m\Phi_0$. The solid line is a fit to the data for an exponential decay with a lifetime of 20 ns. The fit shows good agreement with the data at this bias position.

The lifetime of the excited state is similar to lifetimes measured in a number of other superconducting qubits operated in the phase basis (energy eigenstates in the same potential well). Paik et al. have observed decay times in dc SQUID phase qubits [71] around 13 ns for a $Nb/AlO_x/Nb$ junctions and 20 ns for $Al/AlO_x/Al$ junctions. Martinis et al. observed a lifetime of 20 ns in a large area current biased $Nb/AlO_x/Nb$ Josephson junction [42]. They were able to improve the lifetime to 500 ns [72] by reducing the size of the junction, $\sim 10\mu m^2$, switching to Al junctions, and changing to $SiN_x$ for the wiring insulation layer instead of $SiO_2$.

## 4.3 Intrawell Spectroscopy

Further information on the decoherence can be obtained by studying the lineshape of microwave spectroscopy between the ground and excited states in the same well. The lineshape of the resonant peak at equilibrium with the microwave driving field is dependent on the intrinsic lifetime of the excited state and the detuning noise in general. The microwave radiation is applied for a period long enough that any coherent effects between the states have had time to damp out.

### 4.3.1 As a function of $\phi_x$

Figure 4.2 show the occupation of the excited state as a function of detuning for 3 different attenuator settings; 33, 36 and 39 dB. At these values, the microwave amplitude should be in a range where the width is not dominated by power broadening. A 10 ns readout pulse is used to measure the occupation immediately following a 100 ns microwave pulse. This pulse is much longer then the lifetime of the excited state measured in Fig. 4.1 so that the qubit reaches an equilibrium mixture of the ground and excited state. The detuning is accomplished by changing $\phi_x$, not by changing the frequency. This is more reliable since there are some variations in the power transmitted to the qubit as a function of the frequency. The conversion to frequency detuning is $\delta = 1.70 \times 10^9 s^{-1}/m\Phi_0$ at this $\phi_{xdc}$ in the range of $\phi_x$ in Fig. 4.2. The conversion is taken from spectroscopy in Fig. 4.5 as function of both frequency and $\phi_x$ and is consistent with calculations using the measured parameters.

The lines are fits to the data for the equilibrium values of the occupation state assuming extra noise at frequencies much lower then either $\Gamma$ or $\Omega_{Rabi}$. The line shape is Lorentzian

$$\langle \rho_{11}(t=\infty) \rangle = \frac{\Omega_{Rabi}^2}{\nu^2 + \Omega_{Rabi}^2/2 + \Gamma^2/4} \tag{4.1}$$

where $\Omega_{Rabi}$ is the Rabi frequency, $\Gamma$ is the decay rate from the excited state to the ground state and $\nu$ is the detuning from resonance. The intrinsic Lorentzian lineshape is convoluted with Gaussian detuning noise.

$$\langle \rho_{11}(t=\infty) \rangle = \frac{\Omega_{Rabi}^2}{4\sqrt{2\pi}\sigma} \int_{-\infty}^{\infty} e^{-\nu'^2/(2\sigma^2)} \frac{1}{(\nu+\nu')^2 + \Omega_{Rabi}^2/2 + \Gamma^2/4} d\nu' \tag{4.2}$$

where $\sigma$ is the root mean square value of the low frequency noise and the amplitude of the microwaves is in terms of $\Omega_{Rabi}$. The best fit to the data for all the powers simultaneously, occurs for $\sigma = 2.35 \pm 0.1 \times 10^8 s^{-1}$ and

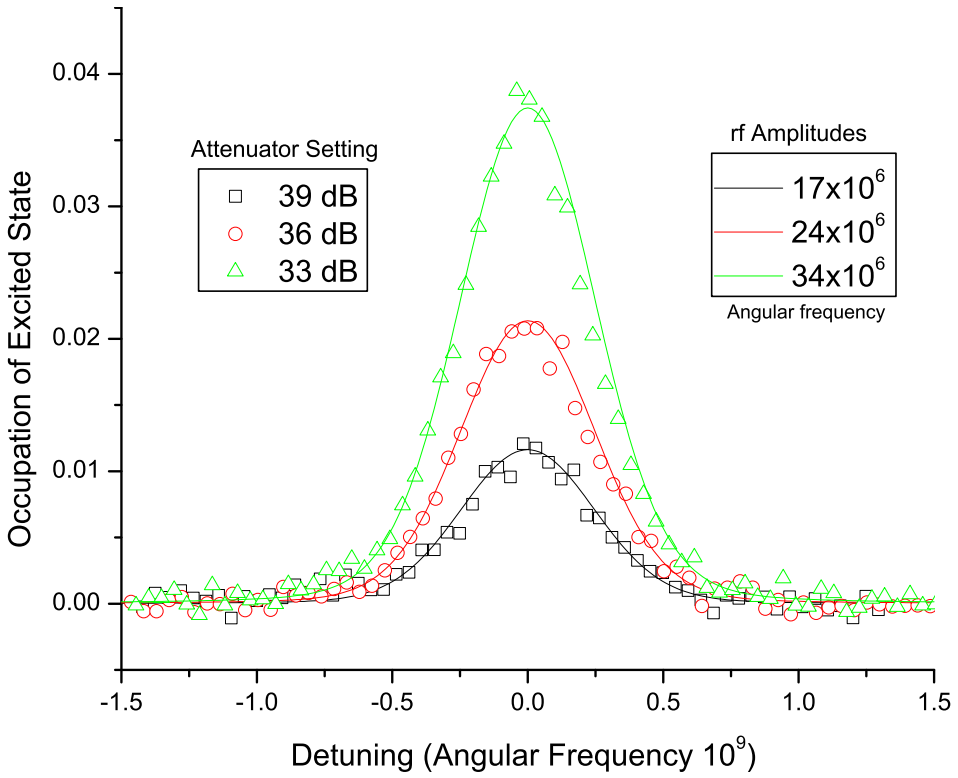


Figure 4.2: The occupation of the excited state as a function of detuning for microwave powers corresponding to attenuator settings of 39, 36, 33 dB. Lines are fits using Equ. 4.2 for microwave amplitudes corresponding to the measured Rabi frequency for each attenuator setting (Equ. 1.20) with $\Gamma = 5.5 \times 10^7 s^{-1}$ convoluted with static Gaussian noise with $\sigma = 2.35 \times 10^8 s^{-1}$ at the angular frequencies of the Rabi oscillations that correspond to these microwave powers

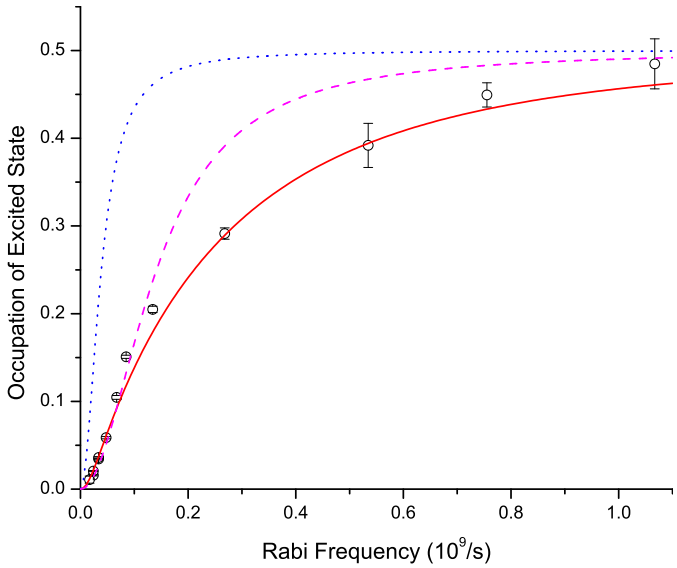


Figure 4.3: The occupation of the excited state on resonance versus microwave amplitude in units of the corresponding Rabi frequency. The lines are calculations for the following parameters; red solid $\Gamma = 5.5 \times 10^7 s^{-1}$ and $\sigma = 2.35 \times 10^8 s^{-1}$, blue dotted line $\sigma = 0$ with $\Gamma = 5.5 \times 10^7 s^{-1}$, purple dashed line $\sigma = 0$ and $\Gamma = 2.0 \times 10^8 s^{-1}$.

$\Gamma = 5.5 \pm 0.5 \times 10^7 s^{-1}$. The low frequency detuning noise can be distinguished from the lifetime of the excited state because the effect of the detuning noise is reduced on resonance where the derivative of energy level spacing as a function of detuning goes to zero in the dressed state picture.

Figure 4.3 shows the maximum of the spectroscopic peak as a function of microwave amplitude under the same conditions. The microwave amplitude is in units of Rabi frequency. The maximum value is taken from Gaussian fits to the data. The red solid line is a fit to the peak amplitudes using Equ. 4.2 at zero detuning with $\Gamma = 5.5 \times 10^7 s^{-1}$ and $\sigma = 2.35 \times 10^8 s^{-1}$. The blue dotted line is a calculation with the same parameters except that $\sigma = 0$ with $\Gamma = 5.5 \times 10^7 s^{-1}$ while the purple dashed line shows $\sigma = 0$ and $\Gamma = 2.0 \times 10^8$ that gives the best fit to the data without considering low frequency noise. Figure 4.4 shows the width of the peaks as a function of microwave amplitude for the same data and the red solid line for the same parameters. The green dashed line is the width for $\Gamma = 5.5 \times 10^7 s^{-1}$ and the blue dotted line $\Gamma = 5.85 \times 10^8 s^{-1}$ and no low frequency noise. The static Gaussian noise is required in order to obtain a reasonable fit to the overall lineshape of the data. The data presented above for this qubit show that compared to the relaxation rate, the detuning noise can be considered static

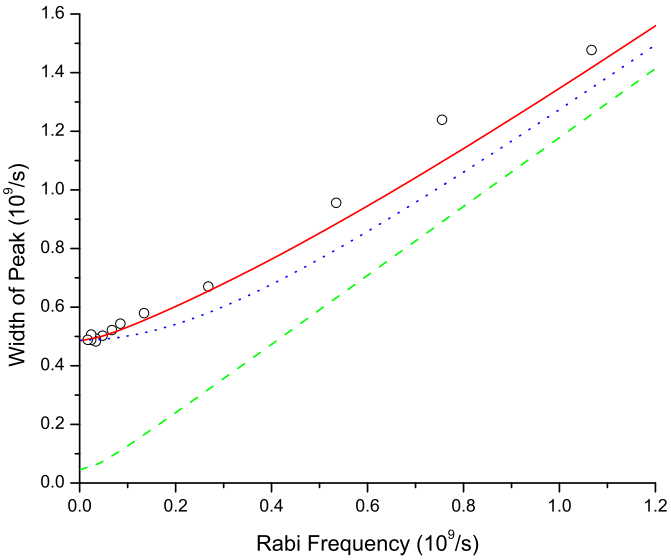


Figure 4.4: The width of the spectroscopic peak from the Gaussian fits as a function of microwave amplitude in units of Rabi frequency. The lines are calculations for the following parameters; red solid $\Gamma = 5.5 \times 10^7 s^{-1}$ and $\sigma = 2.35 \times 10^8 s^{-1}$, green dashed line $\sigma = 0$ with $\Gamma = 5.5 \times 10^7 s^{-1}$, blue dotted line $\sigma = 0$ and $\Gamma = 5.85 \times 10^8 s^{-1}$.

and characterized entirely by its rms value.

### 4.3.2 As a function of frequency and $\phi_x$

The data in Sec. 4.3.1 was taken at a fixed frequency over a narrow range of $\phi_x$. Figure 4.5 shows the occupation of the excited state as function of both frequency and $\phi_x$ at a $\phi_{xdc}$ value corresponding to a $\beta_L = 1.288$. The color contours are proportional to occupation of the excited state, blue being lower occupation and red being the highest occupation. The curving ridge running diagonally from the top left to the bottom right corresponds the resonance between the ground and excited states. The solid lines correspond to the energy difference between the nearest eigenstates of the qubit in the same well of the potential, as a function of $\phi_x$ for the measured values of L and C. The ridge corresponding to the resonance between the ground and excited states can be used to verify the relationship between $\phi_x$ and the resonant frequency used in Sec 4.3.1.

The gaps in the spectroscopy most likely correspond to coupling to two level fluctuators in the dielectrics that have also been observed by other groups investigating superconducting phase qubits [49, 72, 73]. Johnson et al. [74]

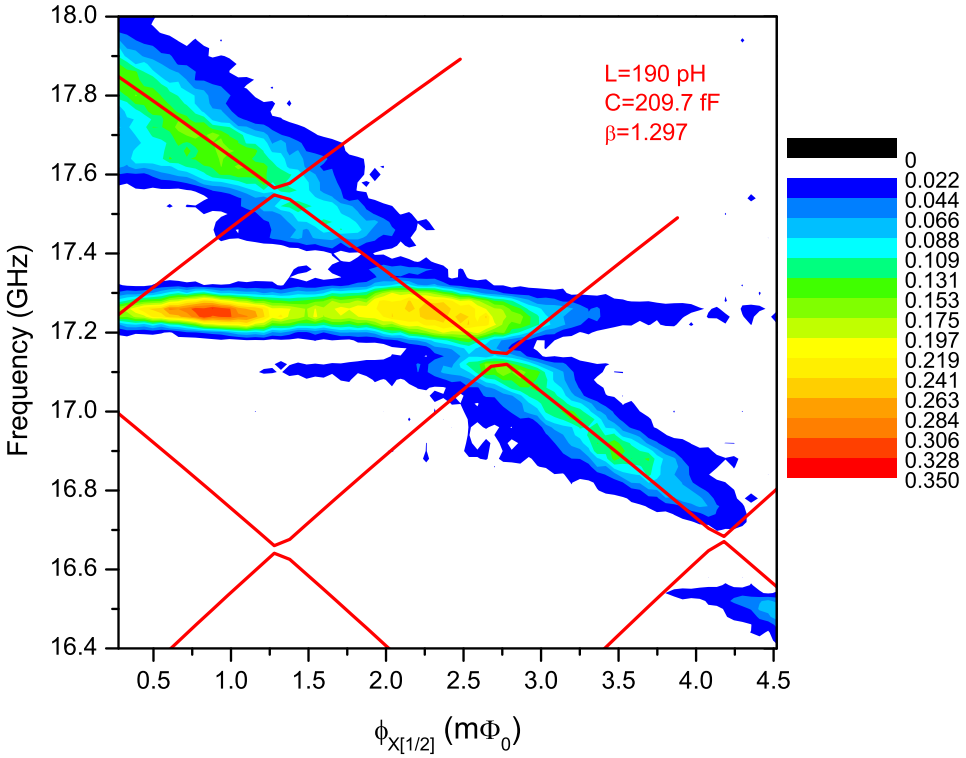


Figure 4.5: The measured occupation of the excited state after a long microwave pulse expressed as color contours (blue being lowest and red being the highest) as function of both frequency and $\phi_x$. The solid lines are calculations of the energy level spitting between consecutive eigenstates states in the same well for $\beta = 1.30$, $L = 190$ pH and $C = 209.7$ fF.

suggests that some of the splittings in reference [49] could be caused by macroscopic resonant tunneling (MRT) into states in the other well. They work with a severely tilted potential where there are hundreds of levels in the right well. This makes it hard to calculate and observe the MRT peaks. However this is not the case for our data in which we are working close to symmetry and know exactly the $\phi_x$ values for MRT. The avoided crossing of the eigenstates show where the MRT peaks would occur. It is possible that some of the splittings are affected by these peaks but there are other splittings that are clearly not related to the MRT.

There are a few other prominent features in the spectroscopy. The most obvious is the horizontal line corresponds to a large cavity resonance at a frequency of 17.25 GHz. The second peak of the cavity resonance, not along the resonance between the ground and excited state, corresponds to a two photon resonance to the second excited state. The frequency is in the range of the lowest order cavity modes of the sample cell, but most of these modes should be suppressed due to the extremely short dimensions ($\sim 1mm$) of the cell in the z direction.

### 4.3.3 Lifetime As a Function of frequency and $\phi_x$

Figure 4.6a shows the occupation of the excited state, using color contours, as a function of delay between the microwave pulse and the flux readout pulse and as a function of $\phi_x$. The microwave frequency is adjusted as a function of $\phi_x$ in order to remain on resonance. The bias value for the measurement of the lifetime of the excited state in Sec. 4.2 would be in the extreme left side of the plot.

At a number of bias points, the decay of the excited states is not exponential. In the region near the gaps in the spectroscopy, there are peaks in the decay of the excited states. Figure 4.6b shows slices of Fig. 4.6a at $\phi_x = 0.767$ $m\Phi_0$ (black squares), 2.078 $m\Phi_0$ (blue triangles) and 5.464 $m\Phi_0$ (red circles). At $\phi_x = 0.767$ $m\Phi_0$ decay is similar to that of Fig. 4.1 while at the other two $\phi_x$ values the behavior is clearly not exponential. The occupation of the excited state actually increases with time and reaches a local maximum at a non zero delay. This is not possible in an isolated two state system without some kind rf power driving the system back to the excited state. However if this were the case there would be an overall increase in the occupation of the excited state which is not observed. Instead it appears that the qubit is coupled strongly to two level fluctuators which was the case for Cooper et. el. [68] in their investigation on current biased phase qubits. They observed an oscillation superimposed on the decay of the excited state near one of these splitting in the spectroscopy similar to the results shown in Fig. 4.6.

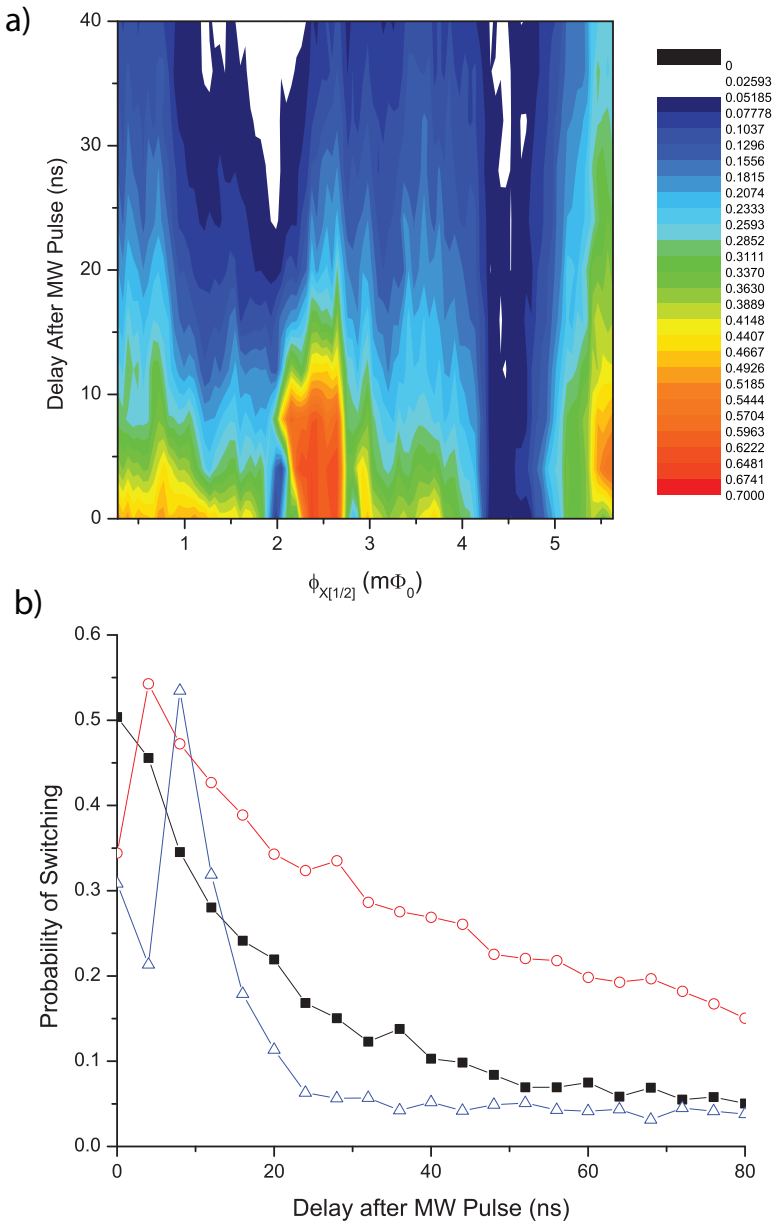


Figure 4.6: a) The measured occupation of the excited state after a long microwave pulse expressed as color contours (blue being lowest and red being the highest) as function $\phi_x$ and the delay between the end of the microwave pulse and the beginning of the readout pulse. b) Slices of the contour plot at $\phi_x = 0.767\ m\Phi_0$ (black squares), $2.078\ m\Phi_0$ (blue triangles) and $5.464\ m\Phi_0$ (red circles). The lines are just to help guide the eye.

## 4.4 Rabi Oscillations

In all the data in the previous sections, there is no evidence of quantum coherence. The measurements were performed using microwave pulses long enough that the qubit had time to reach equilibrium. However quantum coherence between two states is the defining feature of a qubit [75]. The prototypical demonstration of quantum coherence is the observation of Rabi oscillations, discussed previously in Chapter 1.

### 4.4.1 Rabi Oscillations on Resonance

The measurement sequence for coherent oscillations is very similar to the measurement sequence for the lifetime of the excited state except the duration of the microwave pulse is varied and the microwave pulse is immediately followed by the readout flux pulse. The signal for the high frequency line is illustrated in the inset in Figure 4.7. Usually this sequence is repeated 4 times per initialization and readout sequence in order to increase the statistics. The lifetime measurements of Sec. 4.2 are performed in region that show fewer splittings. The cleanest section of the spectrum is at frequencies between 17.6 GHz and the frequency limit of 18 GHz. This is the best region to try and observe coherent oscillations between the ground and excited states.

Figure 4.7 shows a typical example of the Rabi oscillations when the microwave frequency, 17.9 GHz, is on resonance with the transition between the ground and excited state in the same well. Each point corresponds to repeating the measurement process a few thousand times and the data set represents many hours of measurements. The data is fit with a solution to the Bloch equations (Equ. 1.17) exactly on resonance assuming a $0.5ns$ rise time for the microwave pulse. The Rabi frequency $f_{rabi} = 119MHz$ and decay time of the oscillations, $\widetilde{T}_2 = 16.6ns$ are extracted from the fit.

The decay constant, $\widetilde{T}_2$, for Rabi oscillations on resonance takes on a simple form within the Bloch-Redfield theory where the dynamics of a two-level system in a rotating frame are described by two decay rates, longitudinal relaxation $\widetilde{\Gamma_1}$ and transverse relaxation $\widetilde{\Gamma_2} = 1/\widetilde{T}_2$. The transverse relaxation is[76]

$$\widetilde{\Gamma_2} = \frac{3}{4}\Gamma_1 + \frac{1}{2}\Gamma_\nu \tag{4.3}$$

where $\Gamma_\nu$ is the is the spectral density of the noise at the Rabi frequency. In Equ. 4.3 the low frequency noise does not effect the decay of the Rabi oscillations to first order since $\widetilde{\Gamma_2}$ only depends on noise at the Rabi frequency. When the microwaves are exactly on resonance, the derivative of level spacing with respect to $\phi_x$ goes to zero in the dressed state picture. In Equ. 1.19 when

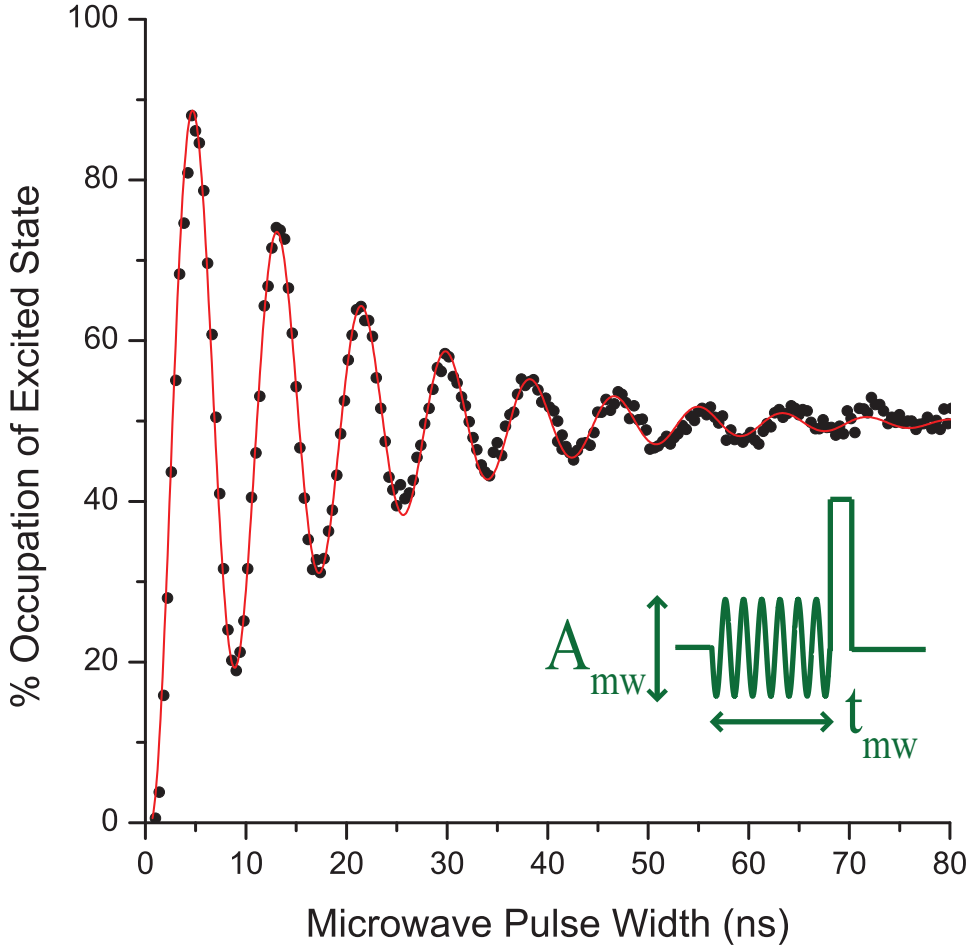


Figure 4.7: The occupation of the excited state as a function of the length of the microwave pulse demonstrating Rabi oscillations. The line is a numerical solution to the Bloch equations exactly on resonance with $f_{rabi} = 119MHz$ and decay time $\tilde{T}_2 = 16.6ns$.

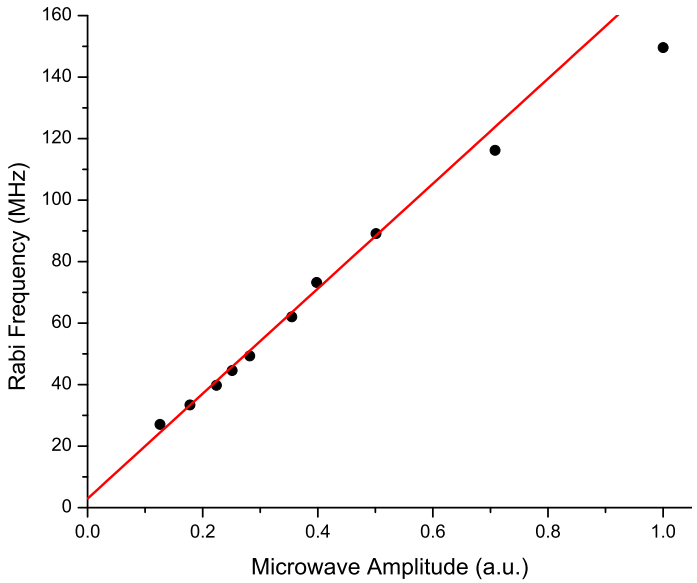


Figure 4.8: The measured Rabi frequency as a function of amplitude of applied microwaves in arbitrary units. The line is a linear fit to the lower microwave amplitude data.

$\delta \ll a_{rf}$, the amplitude and frequency of the Rabi oscillations are not sensitive to the low frequency noise. If the driving amplitude is large compared to the detuning then small low frequency detuning noise does not affect the sum $a_{rf}^2 + \delta^2$. This is why it is possible to have a $\widetilde{T_2} = 16.6ns$ despite the large level of low frequency flux noise. At the Rabi frequency $(119MHz)$, $\Gamma_\nu = 4 \times 10^7 s^{-1}$ using the $T_1 = 20ns$ measured in Sec. 4.2.

Figure 4.8 shows the Rabi frequency extracted from Rabi oscillation measurements at different microwave amplitudes. The microwave amplitudes are in arbitrary units such that the lowest attenuator setting (0 dB) has a microwave amplitude of one. At low powers the Rabi frequency is linear with microwave amplitude as expected from Equ. 1.19. This is additional evidence that the oscillations in Fig. 4.7 are Rabi oscillations and not some other type of classical oscillation. Knowing the correspondence between Rabi frequency and microwave attenuator setting makes it possible to use Rabi frequency as the units for microwave amplitude instead of the unsatisfying arbitrary units.

At higher powers the Rabi frequency begins to saturate. There is evidence that at these power levels there is a small probability of excitation to the second excited state. However since the second excited state has orders of magnitude higher escape rate, this small probability can be significant.

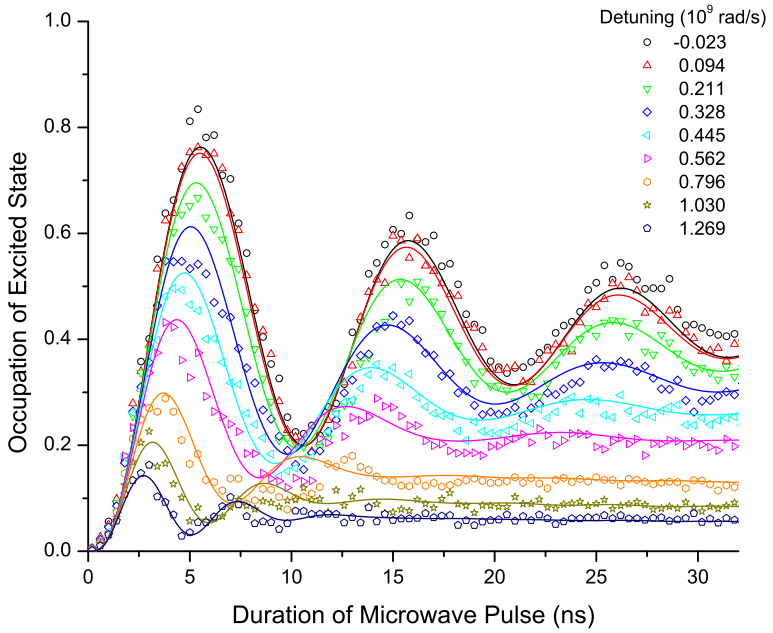


Figure 4.9: Rabi oscillations for various detunings with the corresponding fits using $\Gamma = 7.5 \times 10^7 s^{-1}$ and $\sigma = 2.2 \times 10^8 s^{-1}$

### 4.4.2 Detuned Rabi Oscillations

The Rabi oscillations have their maximum amplitude and lowest frequency on resonance ($\delta = 0$ or $\omega_{rf} = \omega_0$). Equ. 1.19 shows that as the detuning gets larger the amplitude of the oscillations decrease and the Rabi frequency increases. As the detuning gets to be of similar magnitude to the driving field, the Rabi oscillations loose their immunity to the driving noise.

Figure 4.9 shows Rabi oscillations at various detunings towards greater tilts over a range of 0.5 $m\Phi_0$. At long microwave pulse times (not shown) the occupation of the excited state reaches the equilibrium values discussed in Sec 4.3. The Rabi frequency and the decay rate of the oscillations are increasing as expected with increasing detuning.

The data can not be fit to Equ. 1.19 only using the phenomenological decay constants. As a first approximation to the low frequency noise, the cutoff frequency is assumed to be much lower than $\Gamma$ or $\Omega_{Rabi}$ such that it assumed to be constant for a given measurement. The Rabi oscillation is simulated using the Bloch equations at a $\delta_0 + \delta_{lf}$ where $\delta_{lf}$ is a random value taken from Gaussian distribution of width $\sigma$. This process is repeated and the results averaged enough times that Rabi oscillations are averaged over the static Gaussian noise.

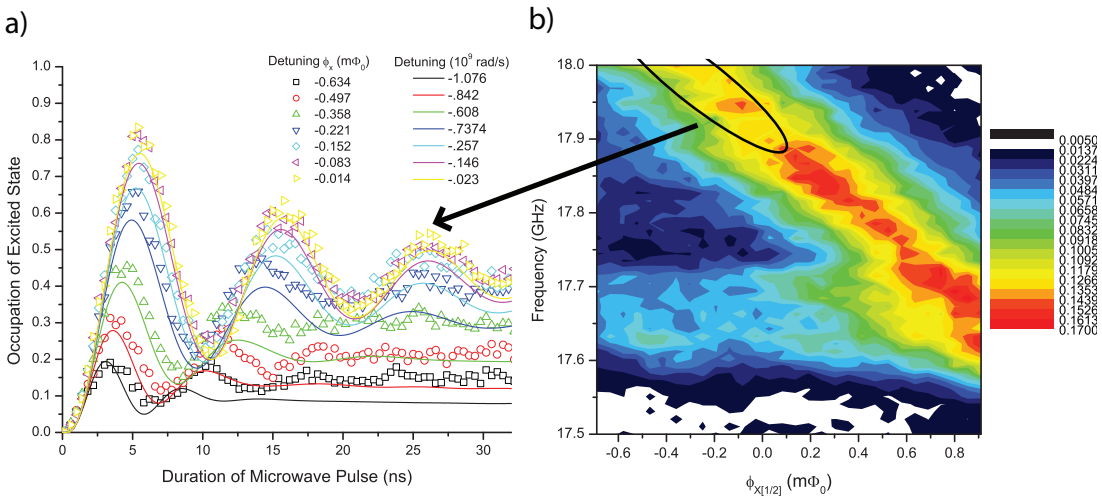


Figure 4.10: a) Rabi oscillations for various detunings in the direction of negative $\phi_x$ with the corresponding fits using $\Gamma = 7.5\times10^7 s^{-1}$ and $\sigma = 2.2\times10^8 s^{-1}$. b) The spectroscopy depicted as color contours in the region of the detuned Rabi oscillations. Zero detuning for a) is close to $\phi_x = 0$ in b).

The lines in Figure 4.9 correspond calculations with an initial Rabi frequency of $590 \times 10^6 s^{-1}$, $\Gamma = 7.5 \times 10^7 s^{-1}$ and $\sigma = 2.2 \times 10^8 s^{-1}$. The detuning frequency is taken from $\phi_x$ using the conversion from Fig. 4.5. For these parameters there is good agreement between the measurement and the calculations further supporting the idea of low frequency noise with a cutoff frequency much less than either $\Gamma_1$ or $\Omega_{Rabi}$.

The range of detuning in Fig. 4.9 is in a region with relatively few splittings. If the frequency is detuned the other direction, the spectrum is not nearly as clean. Figure 4.10a shows the detuning in the direction of increased splittings (shown in Fig. 4.10b). The equilibrium values do not fall off with detuning at the rate expected. The apparent Rabi frequency is inconsistent with the equilibrium value. The lines are calculations for the detunings using the parameters used in Fig. 4.9. The agreement is poor and suggest the splittings have a strong effect on the coherence

### 4.4.3 Rabi Oscillations Near an Avoided Crossing

Figure 4.11 shows a contour plot of the Rabi oscillations as a function of tilt with the microwave frequency compensated to stay on resonance with the energy spacing between the ground and excited state in the same fluxoid state. The occupation of the excited state is proportional to the color scale contours

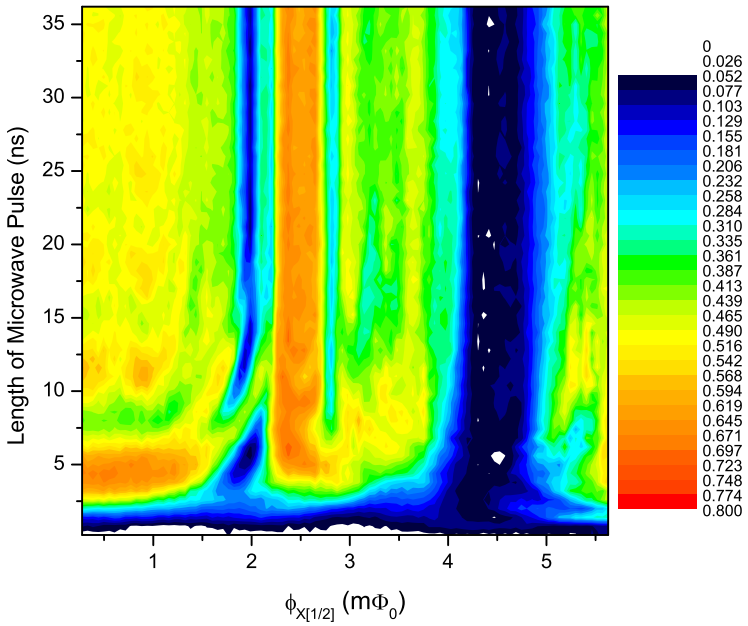


Figure 4.11: The measured occupation of the excited state after a long microwave pulse expressed as color contours (blue being lowest and red being the highest) as function $\phi_x$ and the length of the microwave pulse. The microwave frequency is adjusted to stay on resonance with the energy level separation.

with the lowest occupation as dark blue and the highest as red. The Rabi oscillations occur vertically and manifest themselves as peaks (bright spots) and valleys (dark spots). They are most obvious in the left portion of the plot at $\phi_x$ values less then 1.25 $m\Phi_0$. Many of the splittings observed in the spectroscopy are visible as valleys when moving horizontally across the plot. There are still oscillations in these regions of the plot but they do not have exponential decay and the second peak is often bigger then the first. This is the most obvious for the splitting near 2 $m\Phi_0$ where there is a small initial peak around 2.5 ns followed by a larger second peak moving diagonally between 5 and 10 ns.

## 4.5 Ramsey Pulse Sequence

The dephasing time is typically measured by observing the transverse decay ($T_2$) during free evolution of the qubit. The most straight forward way of observing this decay is by using the Ramsey pulse sequence explained in Sec

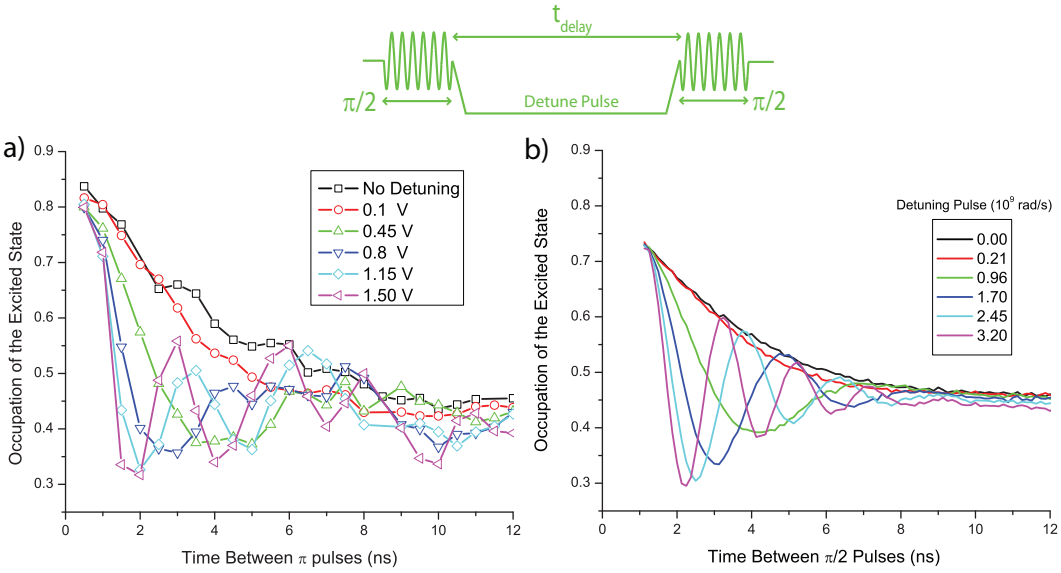


Figure 4.12: a) Measured occupation of the excited state after a series of 3ns microwave pulses as a function of delay between the two pulses. The different lines correspond to different amplitudes of a detuning pulse in $\phi_{xp}$ that occurs during the delay between the microwave pulses. b) Calculations including noise for the pulse sequence by numerically solving the Bloch equations for the parameters corresponding to the measurement.

1.4.3. Observing Ramsey fringes in this system is complicated by the short lifetime of the excited state. In order to be able to observe oscillations there must be significant detuning, i.e. 50 MHz, in order to have a period of the oscillation within the lifetime (20 ns). However at this detuning, the Rabi frequency at powers large enough to get significant population in the excited state is too fast to produce accurate $\pi/2$ pulses. Also, when the microwaves are off, there is no sweet spot with respect to $\phi_x$ and the flux noise will wash out any small oscillations.

An alternative approach is used in which the $\pi/2$ pulses are applied on resonance and the detuning occurs in between the pulses, using an additional $\phi_x$ pulse to tilt the potential. The microwave and pulsing sequence is shown in the inset of Fig. 4.12. In the Bloch sphere picture, the $\pi/2$ pulse sends the system into the equatorial plane, where it sits until the $\phi_x$ detuning causes the Bloch vector to rotate at the corresponding detuning frequency. Relaxation causes the Bloch vector to decay toward the ground state while rotating around the z axis. The result is a phase dependent oscillation due to the detuning, superimposed on the exponential decay.

Figure 4.12a shows the measured occupation of the excited state as a function of delay between 3 ns microwave pulses (17.9 GHz) for several different values of detuning. The data shown is for microwave pulses at power corresponding to $\Omega_{Rabi} = 590 \times 10^6 s^{-1}$. The lines are provided to help guide the eye between the points. Due to the limitations of the pulse generator, when more then one pulse is sent on the same channel in a given period, the step size of the pulse length and delay between pulses is limited to 0.5 ns steps. After careful analysis, it was found that a 3 ns pulse was slightly longer than a $\pi/2$ pulse but the next step down, 2.5 ns, was too short. This can be solved in future experiments by tuning the applied microwave power to change the Rabi frequency in order to make the $\pi/2$ pulse occur at one of the multiples of 1/2 ns.

The Ramsey fringes can be calculated by numerically solving the Bloch equations, using a time dependent detuning along with the time dependent driving amplitude. As in previous sections, the resulting oscillations are convoluted with static Gaussian distributed noise. Figure 4.12b shows the calculated occupation of the excited state for the parameters corresponding to the data in Fig. 4.12a. The scale factor for the amplitude of the detuning pulses was used as a fitting parameter but is consistent with the calibration of the detuning pulses from the ratio of the voltages between the measurement flux pulse and the detuning pulse. The rise times for the detuning pulse was assumed to be the same as was found for the measurement pulse. The rms value of the low frequency noise observed in Sec. 4.3 is also used for this calculation. The relaxation rate that gave the best fit to the data is $\Gamma = 3.0 \times 10^7 s^{-1}$ compared to $5.0 \times 10^7 s^{-1}$ measured in Sec. 4.2. The calculation show qualitative agreement with the data. There appears to be some additional modulation of the Ramsey fringes, possibly caused by different rise times or reflections from the various pulses. Due to the low frequency noise, it is not possible to extract a meaningful $T_2$ from this data.

The quality of this data could be significantly improved with increased control over the length of the microwave pulses and the delay between them. One possibly solution would be to get more output modules for the pulse generator and combine pulses from different channels. This would allow the pulse generator to be operated in pulse generator mode, allowing sub-nanosecond tunability of the timing. Extra modules could also be useful for spin echo type measurements that require three microwave pulses.

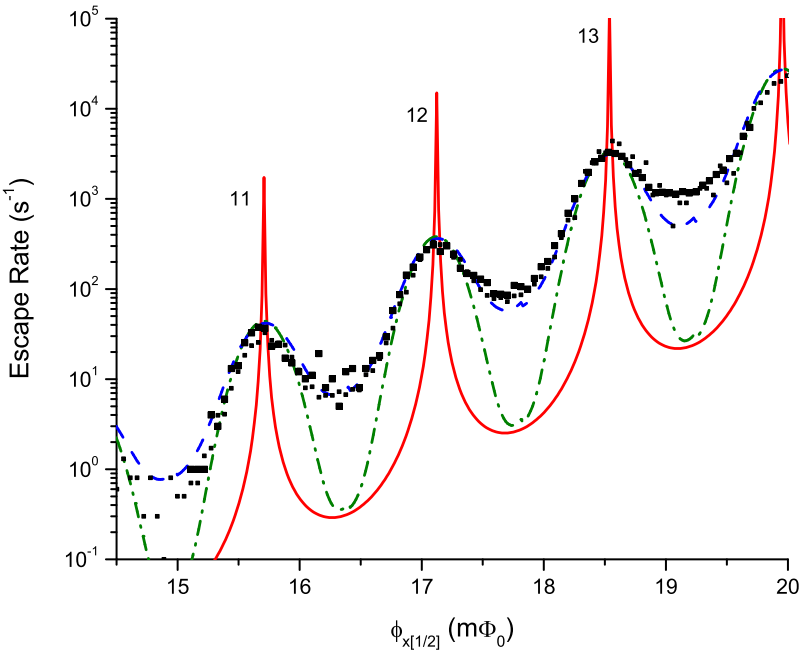


Figure 4.13: Measured escape rates from the ground state in the left well as a function of $\phi_x$ at a $\beta = 1.412$. The solid red line is a calculation for $\Gamma_{12} = 6.8 \times 10^8 s^{-1}$. The green dash dot line corresponds to the solid line with the addition of static Gaussian noise with $\sigma = .23 \times 10^9 s^{-1}$. The blue dashed line has the same level of Gaussian noise but with $\Gamma_{12} = 1.05 \times 10^{10} s^{-1}$.

## 4.6 Comparison with Resonant Tunneling Peaks

The position of resonant tunneling peaks was used in Chapter 3 to verify the qubit parameters. The amplitude and shape of the tunneling peaks can also be used to estimate the amount of decoherence. Due to the short lifetime of the excited states compared to the oscillation frequency between coupled states in this device, at a $\beta_L = 1.4$, the tunneling process consists of incoherent jumps from the ground state in the left well to successive excited states in the right well.

The measured escape rates are shown in Fig. 4.13 as a function of $\phi_x$. The resonant tunneling peaks are labeled with an index which indicate which level in the right well is aligned with the ground state in the left well. The solid line is a calculation of the escape rate assuming ohmic damping using the increase in escape rates between peaks from the qubit parameters found in Chapter 5 and Equ. 1.16 for the line shape of the resonant tunneling peaks. The level separation between crossings is approximated as the sine of the tilt

squared. The decay rate, $\Gamma_{12} = 6.8 \times 10^8 s^{-1}$ is the product of the decay rate directly measured in Section 4.2 and the level number [77] ($n = 12$). The calculation gives peaks much narrower then the measured peaks. The green dash dot lines are these same peaks convoluted with Gaussian flux noise with an rms value ($0.14\ m\Phi_0$) corresponding to the level of detuning noise used to fit the spectroscopy in Sec. 4.3. These parameters fit the peaks of the resonant tunneling peak, but does not reproduce the valleys between them. In order to make the both the peaks and valleys fit, the relaxation rate must be increased to $\Gamma_{12} = 1.05 \times 10^{10} s^{-1}$.

The combination of low frequency flux noise and relaxation rate used to fit the data involving intrawell dynamics does not fit the valleys between the macroscopic resonant tunneling peaks. It is unclear if this is a result of a noise source not included in the analysis, a different scaling of relaxation rates to higher levels or an incomplete knowledge of the tunneling process.

# Chapter 5

# Discussion and Future Work

The results in Chapter 4 paint a consistent picture for the decoherence of the qubit. There is a large amount of low frequency flux noise, 0.14 $m\Phi_0$, and a short lifetime for the first excited state, 20 ns. It is a tougher question to speculate on the cause or causes of the decoherence. The most common and obvious sources of decoherence have been ruled out. This chapter will describe other measurements used to rule out some of these possible sources of decoherence. Other clues can be obtained by comparing the results of Chapter 4 with the results of other groups.

For simple comparison of samples with similar parameters a measurement of the resonant tunneling peaks is sufficient since the peaks are sensitive to both the low frequency noise and the lifetime of the excited state. The resonant tunneling peaks are easier to measure than Rabi oscillations and microwave spectroscopy since the tunneling peaks can be measured without microwaves or fast flux pulses. A detailed analysis is not necessary to compare the resonant peak widths of different samples.

## 5.1 External Noise

The most obvious source of extra noise is the noise coupled from the external control lines. This is not likely the cause of the observed noise for a number of reasons. First, there was never any change in the peaks widths as a result of any change in the room temperature electronics. The level of white noise that was needed to have an effect on the tunneling peaks was well above anything that could possibly be generated in the electronics.

As an additional check on the external noise, a superconducting aluminum shunt was added to the bias circuit that allowed flux to be trapped in a superconducting loop that included the shunt. By setting the current in the

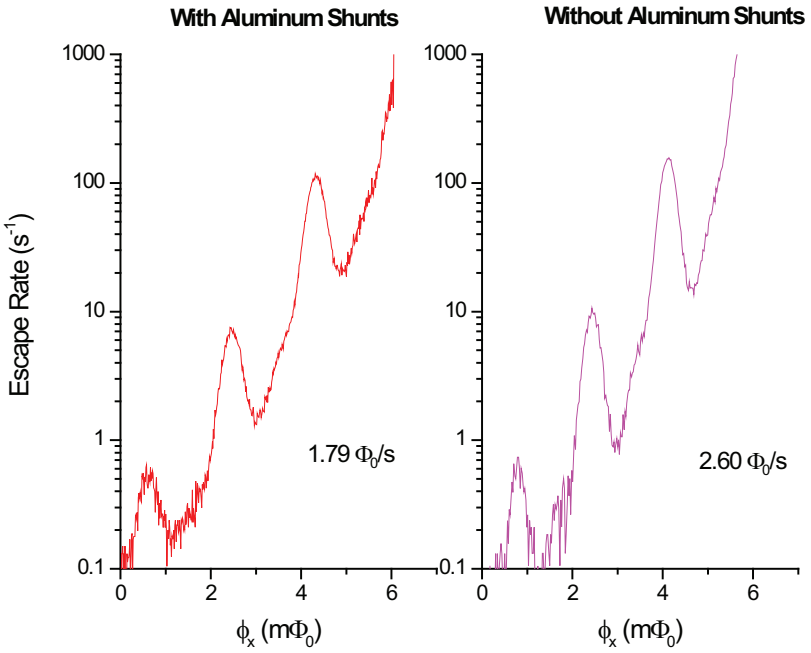


Figure 5.1: Measured escape rates as a function of $\phi_x$ with (left) and without (right) an aluminum wire bind shunt.

loop while cooling through the critical temperature of the Al, approximately 1 K, the amount of flux trapped in the loop is set close to the desired working point. Once the shunt is superconducting, most of the applied current along with most of the current noise, will travel through the shunt and therefore is not coupled to the qubit. The shunt was made by wire bonding across the leads of the bias coil. Fig. 5.1 shows resonant tunneling peaks with and without the shunt. There is no obvious change in widths of the peaks, indicating that external bias noise is not a problem. Longobardi et al. [78] have developed an integrated thin film shunt on chip with a dedicated resistor to heat the shunt past its transition temperature. This allows shunting of the noise similar to the wire bond, but with the ability to control the current level without warming up the sample cell.

Back action from the magnetometer is another potential source of decoherence. However, the magnetometer is operated in a switching current mode in that it is "silent" until it is time to perform the measurement. When the measurement is performed a voltage is established across the junctions creating quasiparticles which destroy the state of the qubit. However, for the technique used to measure the lifetime and the Rabi oscillations, the magnetometer is left in the superconducting state until well after the state of the qubit was fixed.

After the measurement the magnetometer's bias current is ramped back to zero and left there long enough that the quasiparticles disperse. Appendix A describes a design of the magnetometer such that the only current that couples strongly to the qubit is the circulating current. The flux and current biases can be set at a point where the derivative of circulating current with respect to the bias current goes to zero. At this point, fluctuations in the bias current do not be couple to the qubit to first order. However, there is no difference between operating at the optimum bias point and away from the optimum bias point in the measurements of the lifetime of the excited state. This implies that the magnetometer is not the major source of decoherence.

## 5.2 The Local Environment

The evidence seems to point towards something in the local environment as the source of the decoherence. This is corroborated by observations of flux noise of unknown origin in SQUIDs [79–81] and persistent current qubits [82]. The local environment consists mostly of the Josephson junctions, the superconducting Nb films and various insulating layers.

The major sources of decoherence in Josephson junction are predicted to be quasiparticle dissipation and critical current fluctuations. The dissipation is quantified through the subgap resistance of the junctions. Patel et al. [53] have found that the subgap resistance in junctions cofabricated with our qubit devices have a subgap resistance of a 1 $G\Omega$ or greater at 400 mK. This level of dampening would give coherence times much longer than the values measured in Chapter 4. Josephson junctions usually show low frequency fluctuations with a 1/f spectrum. These critical current fluctuations have the effect of modulating the barrier height of the rf SQUID potential resulting in fluctuations of the energy spacing between coupled states. Pottorf et al. [83] have measured the level of 1/f critical current fluctuations in junctions co-fabricated with our qubit devices. Within the model of Van Harligen et al. [84], the critical current fluctuations in these devices are orders of magnitude to small to explain the level of decoherence measured in our sample.

The thin film Nb could potentially have loss despite it superconducting state. The Nb films have the expected values of transitions temperature implying no apparent damage at low frequencies. However due to the kinetic inductance of the Cooper pairs, superconducting films can show losses at high frequencies usually quantified in terms of the surface resistance. The losses at high frequencies (10's of GHz) were tested by measuring the Q's of coplanar waveguide resonators and is explained in further detail in Appendix C. The process for fabricating these resonators is similar to the process used to

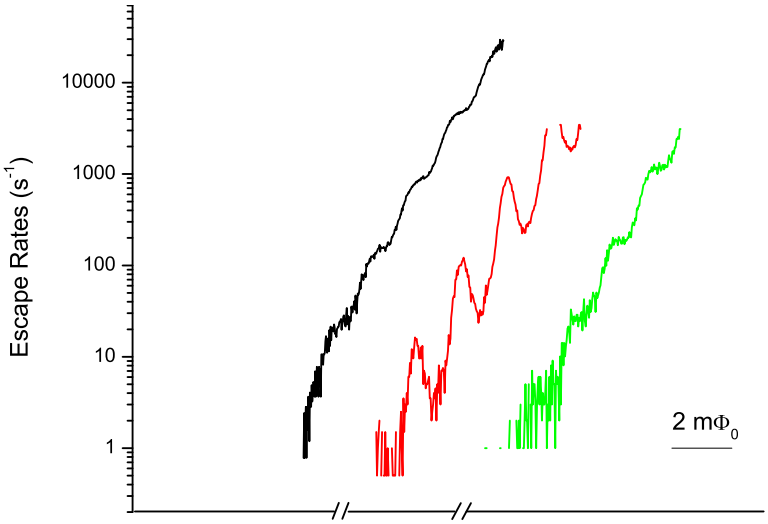


Figure 5.2: Measured escape rates as a function of $\phi_x$ on sapphire (black), 20 $\Omega cm$ silicon (red) and 15 $k\Omega cm$ silicon (green) substrates.

fabricate the qubit samples. Despite discovering losses at these frequencies that seem to depend on the fabrication process, the Q's were sufficiently high to rule out losses in the Nb films as the major source of decoherence.

We currently do not have a direct test of the quality of the insulating layers at low frequencies for the qubit samples. There is evidence [49, 68, 72] that some of the common insulating materials used for qubit fabrication have defects which affect the coherence times of superconducting qubits. The mostly likely candidates in our qubits are the substrate and the insulation under the wiring layer.

Koch et al. [85] have suggested a model for 1/f flux noise in SQUIDS and qubits where the noise is generated by magnet moments of electrons in the defects of the insulating materials. Due to thermal effects, unpaired electrons hop on and off defect centers in which the electron orientation is locked while in one of the two Kramers-degenerate ground state. The orientation is random from trap to trap and the time an electron resides in a given trap varies over orders of magnitude. The uncorrelated spin orientations sum up to give a $1/f$ power spectrum. When applied to qubits loops, this model results in scaling of the noise amplitude as the fourth root of the area. An alternate source for the decoherence has been proposed due to the non-exponential spin-lattice relaxation of paramagnetic dangling-bonds at the amorphous semiconductor-oxide interface [86]. The scaling of the flux noise with size is similar to the previous theory but since it is an effect of the interface the flux noise is not a function of defects in the substrate.

The effect of the substrate on decoherence can be studied by fabricating and measuring qubits on different substrates. However when the substrate is changed it can have other effects on the fabrication process. In general, the resistivity of the silicon substrate should indicate the level of defects and a sapphire substrate should have fewer defects than a silicon substrate. Fig. 5.2 shows measured escape rates as a function of $\phi_x$ for qubits fabricated on sapphire (black), 20 $\Omega - cm$ silicon (red) and 15 $k\Omega - cm$ silicon (green) wafers. All though there is a difference in the widths of MRT peaks for different substrates, the better substrates seem to have wider peaks. Further investigation is necessary to check if the increased width is caused by the substrate and not by some unforeseen effect on the fabrication process.

The $SiO_2$ layer between the junction layer and wiring layer is also a potential source of the observed decoherence. Most superconducting qubits with longer decoherence times are made using $Al/AlO_x/Al$ junctions [76, 87] using a two angle shadow evaporation process that has a thin layer $AlO_x$ for insulation. The NIST group uses a process the includes a deposited insulation layer. When they switched from $SiO_2$ to $SiN_x$ [72] they saw a significant increase in the decay time for their Rabi oscillations.

There are a number of possible design changes that could be used to evaluate the insulation layers. It is possible to move most of the SQUID loop from the base electrode, between the substrate and the wiring insulation layer, to the wiring layer. If the origin of the flux noise is the substrate then this should reduce the overall flux noise. Another important step is to design a sample either using a different material for the wiring insulation layer or removing most this layer near the qubit. The substrate studies should be continued in order to separate fabrication changes from materials changes. Another potentially useful study would be to fabricate rf SQUIDs with different size loops providing an experimental check on the scaling of noise with loop size suggested by Koch et al.

## 5.3 Other Future Improvements

There are a few experimental upgrades that would enhance the characterization of these devices. An improved pulsing system with the ability to send multiple pulses without sacrificing timing control would improve the measurements using the Ramsey pulse sequence and open up the possibility of more elaborate time domain measurements such as spin echo. This would also be of benefit in future studies of coupled qubits and multi-qubit gates.

Also extending the ability to couple rapid pulses to $\phi_{xdc}$ would allow time domain measurement similar to the ones demonstrated here but between levels

of different fluxoid states. The energy difference between these levels can be adjusted to much lower frequencies, potentially away from the frequencies associated with the two level fluctuators. These additional measurements could also allow for careful comparison between coherence times and flux noise in the flux and phase basis. Coherence between flux states in the time domain could also be studied using a rapidly pulsed magnetometer. This requires further studies into the flux pulsing of the magnetometer or potential a change in the setup that would allow current pulsing the magnetometer.

## 5.4 Summary

With careful design of the measurement setup and a suitable fabrication process, it is possible to observe coherent oscillations between two energy levels in a rf SQUID. Since the quantum coherence is extremely sensitive to external noise, extensive steps were taken to protect the rf SQUID. It was fabricated using a flexible, well characterized fabrication process capable of producing high quality Josephson junctions. The flux readout, a hysteretic dc SQUID magnetometer, was optimized to minimize the back action on the rf SQUID. Also the filtering and electronics were carefully designed to reduce the amount external noise reaching the rf SQUID. Finally a setup for very fast pulsing of the bias flux and coupled microwaves was instituted to allow measurement of the coherent oscillations on a nanosecond time scale.

The coherence times of the superposition between the ground and first excited state in the same flux state were measured and analyzed within the context of the known noise sources and calculations based on the parameters of the rf SQUID. There exists low frequency flux noise and a short lifetime for the excited state that are not consistent with known noise sources. The coherence times are currently too short to be useful for quantum computation. However, it is likely that the decoherence is caused by a materials or fabrication issues and could be improved through a carefully comparative study.

# Appendix A

# Low Back Action Magnetometers for Qubit Readout

Low back action measurement of the state of the qubit is critical to the success of any potential quantum computing implementation. The coupling between the readout and the qubit needs to be strong enough to distinguish between the two macroscopic states while not causing significant decoherence of the qubit. Recently two groups have shown improvements in coherence times when their measurement device is operated at an optimum bias point, where to first order the readout does not couple to the qubit [82, 87]. This appendix describes an implementation of a low back action magnetometer to measure a superconducting flux qubit.

The readout for our rf SQUID qubit is a hysteretic dc SQUID magnetometer integrated on chip. When appropriately biased with current and flux, such a magnetometer can be used for single shot measurement of the flux state of the qubit. The layout of the biasing circuitry is designed such that there is no direct inductive coupling to the qubit. However, applying a bias current causes the circulating current to change in the magnetometer loop, which directly couples to the qubit. This indirect coupling of external biases to the qubit through the circulating current provides a path for external noise to couple to the qubit. By designing an asymmetry in the critical currents of the two Josephson junctions of the magnetometer, the dynamics of the dc SQUID can be manipulated such that at the required bias current, the derivative of the circulating current vanishes. Thus at this sensitive bias point, to first order, fluctuations in the current bias are not coupled to the qubit. Subsequently, fast external flux pulses can be used to probe the switching current and detect the state of the qubit.

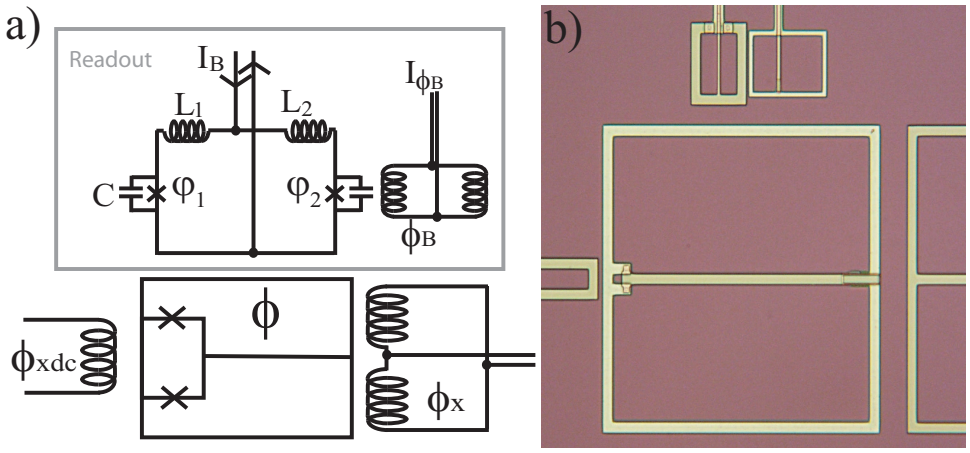


Figure A.1: a) Schematic and b) photograph of rf SQUID qubit and the readout magnetometer.

A dc SQUID, shown schematically in Fig. A.1a, consists of two Josephson junctions in a superconducting ring with leads to provide current bias. The junctions are modeled as ideal Josephson currents with phase differences across the junctions $\varphi_1$ and $\varphi_2$ in parallel with capacitance $C$. The maximum critical current $2I_{c0}$ is the sum of the critical currents $I_{c1}$ and $I_{c2}$ of the two junctions. The junction asymmetry is defined as $\delta i = (I_{c1} - I_{c2})/2I_{c0}$ . The junctions are coupled by two ideal inductors $L = L_1 + L_2$ with their asymmetry parameter defined as $\delta L = (L_2 - L_1)/L$. The loop is biased by current $i_B$ in units of $2I_{c0}$ and external flux $\varphi_B$ in units of a flux quantum $\Phi_0/2\pi$.

The phase of the junctions can be rewritten as the average $\varphi = (\varphi_1 + \varphi_2)/2$ and the difference $\varphi_{dc} = (\varphi_1 - \varphi_2)$ of the phases across the junctions. The equations of motion for a dc SQUID are analogous to that of a particle of mass $C$ moving in a two-dimensional potential given by [88]

$$\begin{aligned} U(\varphi, \varphi_{dc}) &= \frac{1}{4\beta}(\varphi - \varphi_B)^2 - \frac{i_b}{2}\varphi - \cos(\frac{\varphi_{dc}}{2})\cos(\varphi) \\ &\quad -\delta i \sin(\varphi)\sin(\varphi_{dc}) - \frac{\delta L i_b}{2} \end{aligned} \tag{A.1}$$

where $E_J = 2I_{c0}\Phi_0/2\pi$ and where $\beta = 2\pi L I_{c0}/\Phi_0$. The circulating current in the magnetometer can be calculated by finding the minimum of the two dimensional potential as a function of bias current and external bias flux. The values of $\varphi$ and $\varphi_{dc}$ at the local minimum are used to find the total current circulating in the loop as $i_{circ} = (\varphi_{dc} - \varphi_B)/\beta$ in units of $I_{c0}$. The magnetometer back-action is $Mi_{circ}$, the effective flux coupled into the qubit,

where $M$ is the mutual inductance between the qubit and the magnetometer. At the local minima in $i_{circ}(i_B)$ the first derivative with respect to $i_B$ is zero hence to first order, fluctuations in the bias current do not couple into the qubit. When the junctions are identical ($\delta i = 0$) this local minimum is at zero bias current. However, the magnetometer is not sensitive to the flux of the qubit at this point because it is far from the switching current. By introducing an asymmetry in the size, and therefore the critical current of the junctions, the minimum is shifted closer to the switching current. If the minimum is close enough to the switching current, a fast flux pulse or current pulse can be coupled to the magnetometer, allowing to read-out the state of the qubit before the induced fluctuations can effect the quantum coherence.

## A.1 Design and Fabrication

In our setup, fast flux pulses are inductively coupled to the magnetometer from another chip which contains the other high frequency pulse lines for the experiment, see Sec 2.2.2, and is suspended 25 $\mu m$ above the qubit chip. In a region above the magnetometer these pulse lines are microstrips with a hole in the ground plane. When the pulse chip and the qubit chip are carefully aligned the hole in the ground plane is positioned over the top of one of the arms of the dc SQUID magnetometer thus coupling flux only to the magnetometer. The coupling between the pulse lines and the magnetometer was measured to be 0.5 $pH$ in good agreement with simulations using 3D-MLSI software [54]. We have measured the state of the qubit with flux pulses as short as $10ns$.

The magnetometer biasing circuitry is carefully designed so that the level of fluctuations coupling to the qubit is minimized. Both the magnetometer and the flux bias loop are gradiometric (Fig. A.1a) so that direct coupling due to geometric inductances is minimized. By designing a small asymmetry in the gradiometric flux bias loop, the direct coupling to the qubit is compensated by the coupling via the magnetometer. With this design, the residual couplings to the bias leads can be made less than 1 $fH$ hence the circulating current is the only part of the readout with significant coupling to the qubit.

The devices were fabricated using the Stony Brook SAL-EBL process [52, 53]. The process yields high quality deep-submicron junctions with dimensions as small as 0.15 x 0.15 $\mu m^2$. The high area uniformity of the junctions allow us to accurately program junction asymmetry. The junctions of the magnetometer are designed to be 2.15 x 2.15 $\mu m^2$ and 2.85 x 2.85 $\mu m^2$ in size ($\delta i = 0.19$).

The value of the maximum critical current of the magnetometer, $2I_{c0} = 10.8\ \mu A$, was extracted from fits to the switching distribution taken at 10 mK

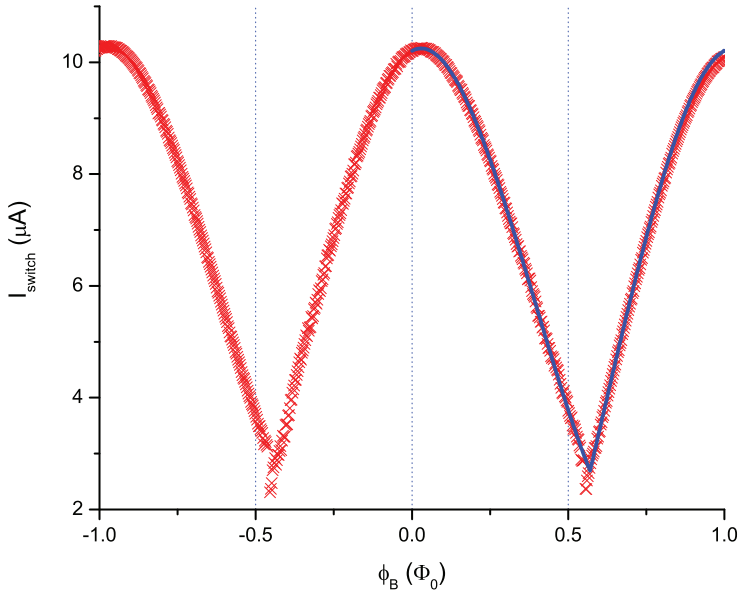


Figure A.2: Switching current ($I_{switch}$) of the magnetometer as a function of flux applied by external bias ($\phi_B$). X's are measured values at 10 mK for a ramp rate of 2 mA/s and the line is the calculated $I_{switch}$ for $\delta i = .19$ and $2I_{c0} = 10.8\ \mu A$

and at 1.1 K [89]. The measured mean switching current as a function of $\phi_B = \varphi/2\pi$ is shown in Fig. A.2 along with mean switching current calculated by solving Equ. A.1. The junction asymmetry causes the maximum switching current as a function of $\phi_B$ to shift from zero by $28 \pm 2\ m\Phi_0$ consistent with the designed asymmetry $(\delta i)LI_{c0} = 30\ m\Phi_0$ [90]. The modulation of the magnetometer's switching current measured as a function of the external flux is in good agreement with critical currents calculated from the 2d potential, Eq. A.1, for $\delta i = 0.19$ and $2I_{c0} = 10.8\ \mu A$.

## A.2 Measurement

The effect of the magnetometer on the qubit is determined by measuring the amount of additional flux $i_{circ}$ adds to the qubit. The additional flux is seen as a shift of tunneling rates as a function of the external flux bias of the qubit ($\phi_x$). The additional flux from the $i_{circ}$ is measured as a function of $I_B$ and compared with calculations using Eq. A.1. Fig. A.3 shows typical data for the escape rate as a function of potential tilt for five different values of $I_B$. The peaks correspond to the lowest energy level in the left well crossing an

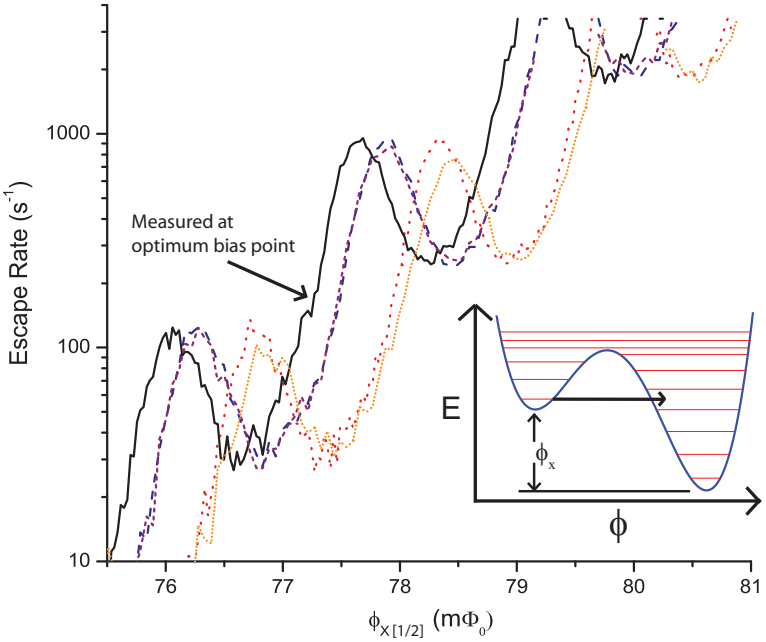


Figure A.3: Measured value of escape rate out of the left well as a function of the qubit's flux bias ($\phi_x$) for various values of $I_B$ (from right to left 0.0, 7.0, 2.0, 6.0, 4.5 $\mu A$). Inset shows the potential energy of the qubit as a function of flux showing the quantum levels.

excited state in the right well (see inset in Fig. A.3). Since these peaks are a function of the tilt of the potential, they can be used to determine the amount of flux coupled to the qubit by the magnetometer.

Fig. A.4 shows $i_{circ}$ as a function of $I_B$ for two different values of the external flux bias of the magnetometer ($\phi_B$). The points represent the measured flux shifts of the qubit divided by the mutual inductance (M). The solid lines are fits to the data using Eq. A.1 with M as a fitting parameter. The data shows clear minima in the $i_{circ}$ as a function of $I_B$ for all $\phi_B$ on this branch of the modulation curve. These minima are the optimum current bias values for reducing the back-action to the qubit. The peaks in the tunneling rates do not narrow up near the optimum bias point, implying noise from the magnetometer bias is not the dominant source of decoherence.

The fits to the data give a critical current asymmetry of $\delta i = 0.19$. This is consistent with the asymmetry of $\delta i = 0.18 \pm 0.03$ found by fitting the switching current as a function of external flux bias and also in agreement with the designed geometrical asymmetry. The 5 pH mutual inductance obtained from the fits is consistent with a value of 4.9 pH obtained from the measured separation of the qubit's flux states and the qubit parameters, measured

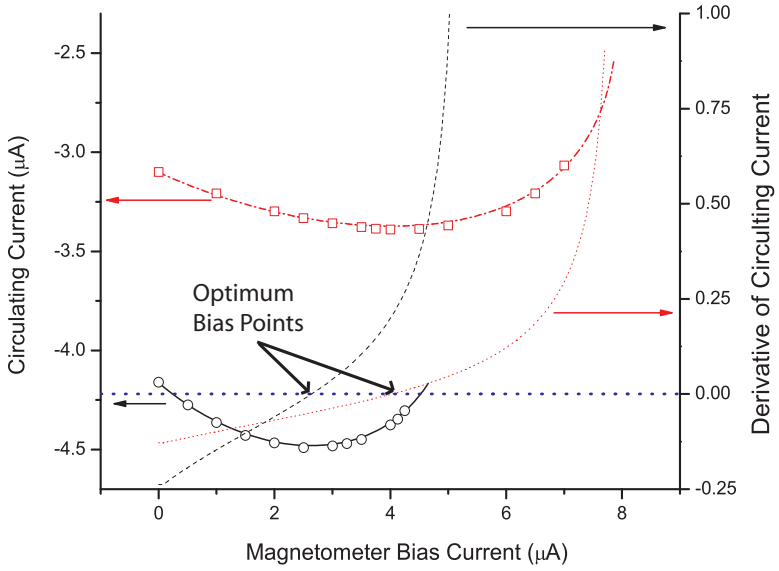


Figure A.4: Circulating current in the magnetometer as a function of the magnetometer's current bias. The squares and circles are measurements at $\phi_B = .300$ and $.436\ \Phi_0$ respectively. The solid and dashed lines are fits to the data from solving Equ. A.1 with $\delta i = 0.19$. The dashed lines are derivatives of the fits as a function of $I_B$ (right axis).

independently from macroscopic quantum tunneling (MQT) [91] and thermal escape rates above the crossover temperature [22**?** ]. Simulations using [54] yield a value of 4.3 pH.

At the optimal bias point the amount of noise coupling to the qubit is a function of the second order terms in $i_{circ}$ and the shift in $I_B$ relative to the optimum bias point. Figure A.4 shows $\partial i_{circ}/\partial i_B$ for both values of $\phi_B$. The noise in the magnetometer's bias current in our setup, dominated by the thermal noise of the filters, is predicted to be 300 $fA/\sqrt{Hz}$ below 2 MHz and 20 $fA/\sqrt{Hz}$ above 10 MHz. At these noise levels, for the second order terms to be relevant, $I_B$ would have to be much closer to the minimum then the precision in our setup allows. Within our uncertainty in $I_B$, the fluctuations in the circulating current should be reduced by a factor of more then $10^4$ less than the fluctuations in $I_B$.

Fluctuations in the external flux bias of the magnetometer can also couple through the magnetometer to the qubit. We measured the flux added to the qubit as a function of $\phi_B$ while the magnetometer is biased at the optimum bias point. This data, shown in Fig. A.5 was fit with a line to extract the mutual inductance between the external flux bias and the qubit. The measured value of 32 fH is close to the design value and too small to couple significant noise

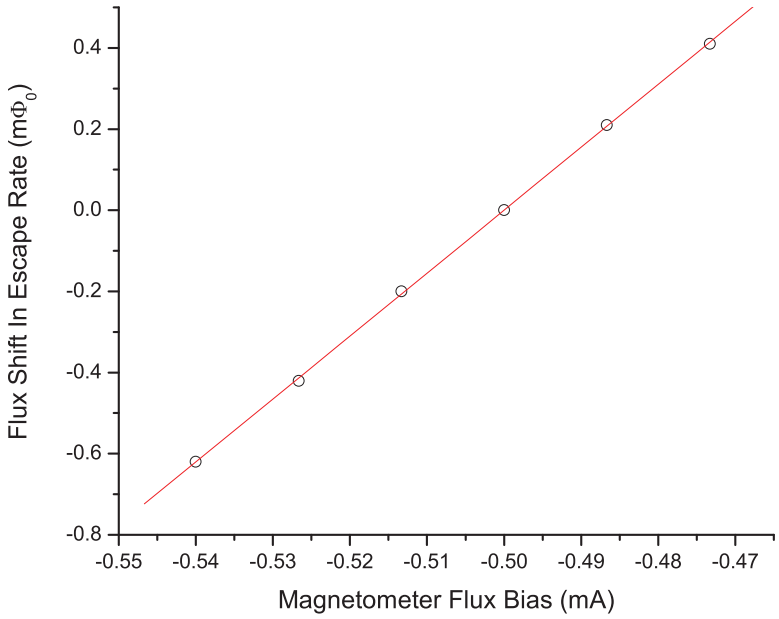


Figure A.5: Coupling between $\phi_B$ and the qubit measured at the magnetometer's sweet spot.

to the qubit for the predicted values of noise at this bias. It is also possible to reduce noise from $\phi_B$ using a superconducting shunt similar to the type demonstrated by Longobardi et al. [78].

In summary, we have fabricated asymmetric dc SQUID magnetometers for use in low back action measurements of superconducting flux qubits. These magnetometers show a minimum in the circulating current as a function of bias current at bias currents close to an operating point sensitive to the state of the qubit. At this point there should be a reduction of noise from the bias circuitry by a factor greater than $10^4$. The widths of the peaks in the tunneling rate does not change at the optimum bias point implying some other noise source is the dominant source of decoherence. Recent experiments on flux qubits by other groups have shown improved decoherence times when the magnetometers, with a small unintentional asymmetry, are operated at the minimum of the circulating current [82, 87]. Our design allows fast measurement of the qubit state while still operating at this optimum bias point.

# Appendix B

# High Frequency Filters for Measurement and Control of Qubits

The observation of coherence between quantum states requires extensive filtering to protect against noise coupled from room temperature electronics. Section 2.3.2 describes some of the different stages of filters. Common RC filters only work up to a resonant frequency due to the parasitic inductance of the capacitor [61]. The parasitic inductance of the capacitor is modeled as a lumped inductance in series with the capacitance. In an RC circuit the capacitor shorts high frequency signals to ground. However when the parasitic inductance is included the high frequency signal is blocked from traveling through the series combination. The frequency where the impedance due to the inductance is greater then the impedance due to the capacitance is given by

$$f_{res} = \frac{1}{2\pi\sqrt{L_{para}C}} \tag{B.1}$$

Good high frequency chip capacitors usually have a parasitic inductance of around 500 pH [61, 92]. If a 1 nF capacitor is used for a low pass filter then the resonant frequency is around 225 MHz. So this type of filter does not work well to filter high frequency noise in the GHz range and above.

Transmission line filters are used to avoid the problem with parasitic inductance in RC filters. A lossy transmission line can be modeled as series inductance (L) and resistance (R) per unit length and shunt capacitance (C) and conductance (G) per unit length. The voltage transmitted through the

transmission line goes as [93]

$$V = V_0 e^{-2\alpha z} \tag{B.2}$$

where $V_0$ is the initial voltage, z is the propagation distance and $\alpha = \mathrm{Re}(\gamma)$ is the attenuation constant. The propagation constant ($\gamma$) is defined as

$$\gamma = \sqrt{(R + j\omega L)(G + j\omega C)} \tag{B.3}$$

where $\omega$ is the frequency of the signal. For all of the cases discussed here it can be assumed that $G = 0$. At high frequencies when $R \ll \omega L$ using the binomial expansion and taking the real part

$$\alpha = \frac{1}{2}\frac{R}{Z_0} \tag{B.4}$$

where $Z_0$ is the characteristic impedance and is given by $Z_0 = \sqrt{\frac{L}{C}}$. In the frequency range when $\omega L \ll R$ then the propagation constant becomes $\gamma = \sqrt{j\omega R}$ and taking the real part is

$$\alpha = \frac{\sqrt{2\omega RC}}{2} \tag{B.5}$$

Finally when $\frac{\sqrt{2\omega RC}}{2} * z \ll 1$ which can be rewritten as $\omega \ll \frac{2}{\ell^2}\frac{1}{RC}$ where $\ell$ is the length of the transmission line, then the frequency dependent term in Equ. B.2 is approximately constant and the transmission line can be treated as a lumped resistance.

There are a number of distributed filters that can filter in this frequency range including copper powder filters, thermocoax and microstrip filters [94]. Copper powder filters work by using the skin effect in the individual copper grains to attenuate high frequencies [95]. Thermocoax uses the resistance of the cable to form a lossy transmission line [96]. For this setup, lossy microstrip filters were developed that roll off faster than copper powder filters and do not require all the space that is necessary for thermocoax lines.

## B.1 Design and Fabrication

Our microstrip filters were designed to be compact, attenuate strongly at high frequencies and constructed to be microwave tight. They consist of a thin film of chromium deposited on a substrate and diced into long narrow chips. When the chips are placed in a brass housing, which acts as a ground plane,

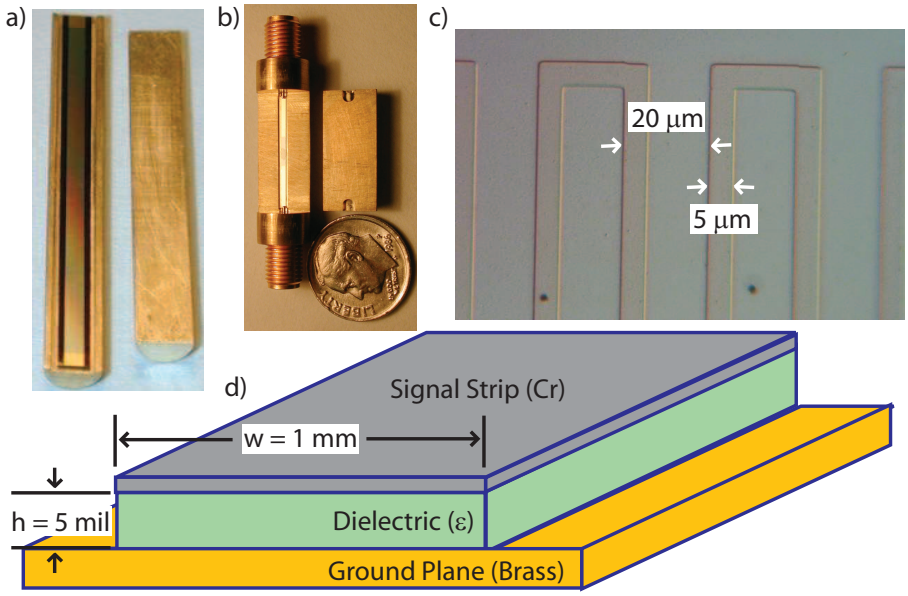


Figure B.1: Pictures of the lossy microstrip filter a) with and b) without the Nb meander line, inside their respective housings. c) A picture of the Nb meander line on top of the chromium. d) A schematic representation showing the structure of a microstrip filter.

they form a lossy microstrip transmission line. Some of the bias currents for our qubit require milli-amps of current. At these currents, any non-negligible resistance could cause heating of the filters and the sample. To avoid heating in the filters that need to pass dc currents, a superconducting shunt is deposited on top of the chromium microstrip. The shunt is patterned as a meander line to give it a large enough inductance that it blocks high frequency signals while allowing dc currents to pass through without resistance. At high frequencies above the cutoff off the meander line, the current must pass through the chromium microstrip and is filtered.

The characteristics of this lossy transmission line can be estimated from the structure of the microstrip, see Fig. B.1d. $Z_0$ of the microstrip is dominated by the width of the strip (w), the height of the strip above the ground plane (h) and the dielectric constant of the substrate material ($\epsilon_r$). Approximate values of $Z_0$ can be found in the literature [55, 93].

The filters were fabricated in our thin film fabrication facility. The chromium thickness can be varied to change the resistance per square of the film. The thickness was changed from wafer to wafer depending on the desired parameters and was usually between 10 and 40 nm giving a corresponding resistance of 10 to 110 Ω per square. The chromium was evaporated on 5 mil glass or

sapphire wafers. The Nb meander is patterned using electron beam lithography and then etched using our standard process (Sec. 2.1) [53]. The meander line has a thickness of 5 $\mu m$ and a pitch of 20 $\mu m$ to obtain an inductance of approximately 1.3 $\mu H$. The meanders were 1 mm wide and in some filters were as long as 30 mm, so the 2 mm electron beam fields were stitched together to make the meander. A 250 nm layer of $SiO_2$ is deposited on top of the niobium to protect it from scratching and breaking which was a problem in the original batches of filters. The filters are diced to the necessary length and width to reach the desired response and glued to the housings using GE varnish.

Originally 60 nm thick gold solder pads were added to allow wires to be soldered directly to the filters. However these connections were inconsistent and showed resistances on the order of 1 $\Omega$. The resistance was most likely caused by the thin layer of chromium deposited on top of the Nb to help the gold adhere to the structure. Instead of soldering directly to the chips, the wires were soldered to pc boards attached to the housing using GE varnish. Al wire bonds were used to connect the pc board directly to the Nb meanders.

Microwaves can propagate in waveguide modes in the filter housing if their frequency exceeds the cutoff frequency. The cutoff frequency for the transverse electric modes , $TE_{m,n}$, and transverse magnetic modes, $TM_{m,n}$ is given by [93]

$$f_{m,n} = \frac{1}{2\pi}\sqrt{\frac{1}{\mu\epsilon}\left[\left(\frac{m\pi}{W}\right)^2 + \left(\frac{n\pi}{H}\right)^2\right]} \tag{B.6}$$

where W and H are the width and height of the cavity respectively and m and n are indices identifying the number of nodes perpendicular to the direction of propagation, where for $TE_{m,n}$ either $m \neq 0$ or $n \neq 0$ and for $TM_{m,n}$ both $m \neq 0$ and $n \neq 0$. In all of our filter housing designs, Fig. B.1a-b, the height of the cavity is much smaller then the width. For this geometry, Equ. B.6 shows the cutoff frequency for all the modes are increased by reducing the height except the $TE_{1,0}$ which is, independent of this dimension. For the low frequency control lines, the filter housings have dimensions $W = 2.38$ mm and $H = 0.30$ mm, the lowest order waveguide cutoff is $f_{1,0} = 62.7$ GHz and the next lowest mode has a cutoff of $f_{1,1} = 496$ GHz. For the pulse lines, the filter housings have dimensions $W = 1.60$ mm and $H = 0.46$ mm, the waveguide cutoff is $f_{1,0} = 93.7$ GHz and the next lowest mode has a cutoff of $f_{1,0} = 341$ GHz.

## B.2 Testing

Figure B.2 shows the power transmitted through the filter to a detector with a 50 Ω load at room temperature (blue squares) and at 4.2 K (red circles). At high frequencies the rf signal was generated using a HP 83731B synthesized signal generator or a HP 8620C sweep oscillator using a HP 435A power meter and HP 8484A diode power sensor to detect the signal. At lower frequencies, a SRS DS345 synthesized function generator was used to create the signal and a standard oscilloscope was used to measure its rms amplitude. The black triangles show the background of the power sensor. The high and low frequency data sets do not exactly overlap since the power sensor was outside its calibrated range. The room temperature data shows 16 dB of attenuation below 10 MHz due to the current primarily traveling though the resistive chromium. The Nb meander line is not superconducting and gives a resistance larger than the chromium. The cutoff, 71 MHz, is consistent with the designed cutoff of the lossy microstrip line. When the Nb goes superconducting the low frequency current is shunted through the meander line and the attenuation is that of the cables alone. The first cutoff at 15 MHz corresponds to the cutoff of the meander line while the second kink is the cutoff of the microstrip. The data shows that after the cutoff the attenuation quickly increases beyond what can be measured using the current setup and stays below the detection threshold to frequencies at least as high as 20 GHz. The Nb meander lines were tested using four point measurements and are superconducting for currents up to 10 mA.

The lossy microstrip filters provide a flexible way to effectively filter many signals over a wide ranges of frequencies. They are very flexible since the cutoff and attenuation level of the filters can be controlled using the dimensions and the resistivity of the microstrip. The filters are easy to fabricate and install making them useful for careful measurements of quantum behavior.

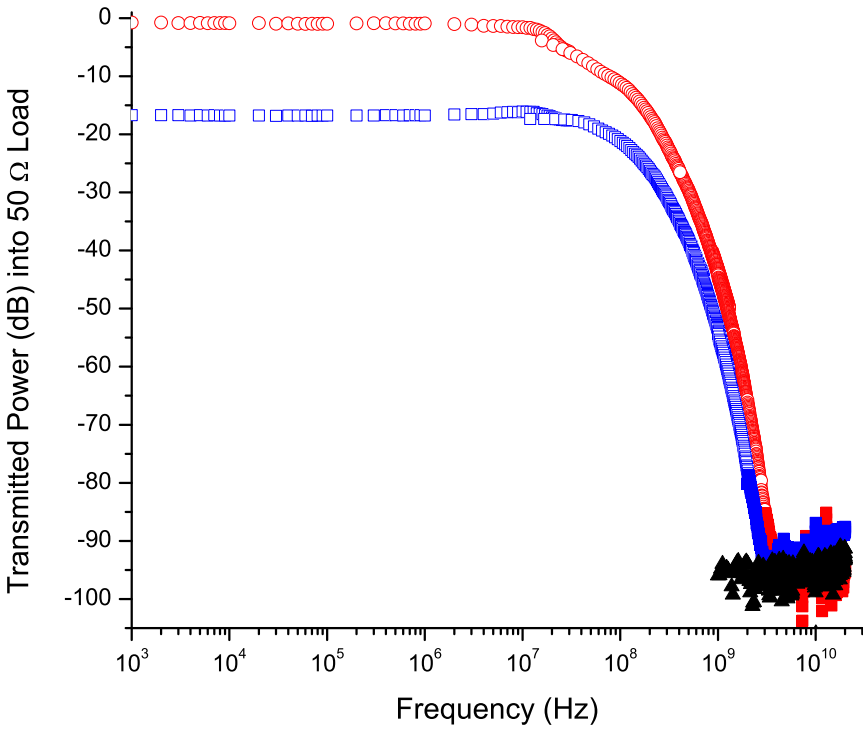


Figure B.2: The power transmitted though the lossy microstrip filter into a 50 Ω load as a function of frequency, measured at room temperature (blue squares)and 4.2 K (red circles)

# Appendix C

# Materials and Process Characterization using Coplanar Waveguide Resonators

Most of the significant progress in improving the coherence times of superconducting qubits has been based on existing fabrication technologies utilizing standard materials. However, recently many groups have found that it is precisely these materials and fabrication technologies that are the limiting factors to further increases in coherence times [49, 68, 72]. Careful studies and solutions to these issues are vital to the future progress of quantum computation using superconducting qubits. The time and resources necessary to measure coherence times of superconducting qubits make it impractical to use these measurements alone to investigate changes in materials or the fabrication process. This appendix gives details on how coplanar waveguide resonators were used to investigate how the substrate and fabrication steps affect the loss at high frequencies of our rf SQUID qubit.

The Q of any resonant structure is a function of the inherent loss mechanisms associated with the electromagnetic fields in the resonator and the coupling of the resonator to losses in the rest of the circuit. The inherent loss mechanisms for a planar transmission line resonator are made up of the conductor loss ($Q_c$), the dielectric loss ($Q_d$) and the radiative loss ($Q_r$) and hence the intrinsic Q ($Q_0$) is [55]

$$\frac{1}{Q_0} = \frac{1}{Q_c} + \frac{1}{Q_d} + \frac{1}{Q_r} \tag{C.1}$$

$Q_d = 1/\tan(\delta)$ where $\tan(\delta)$ is the loss tangent of the dielectric substrate [55]. The $Q_c$ is dependent on the the geometry of the coplanar waveguide but is in

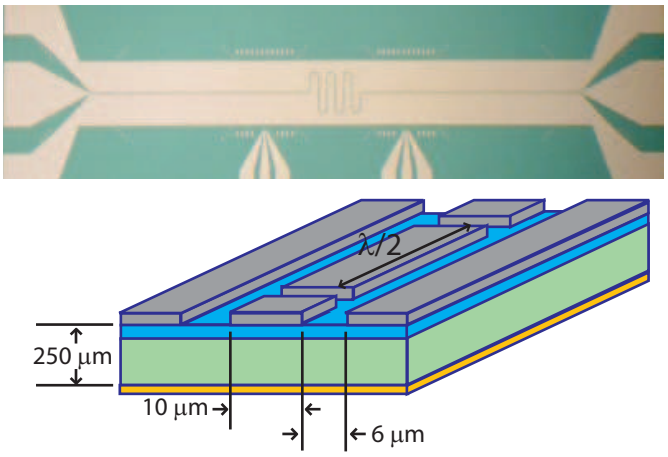


Figure C.1: A co-planar waveguide resonator made of Nb on an oxidized Si substrate. The electrical length of the resonator is about 8 mm. The center conductor is 10 $\mu m$ wide and the gap between the center conductor and ground plane is 6 $\mu m$. Coupling gaps between 2 $\mu m$ and 6 $\mu m$ are used in our study.

general $Q_c \propto f_0/R_s$ where $R_s$ is the surface resistance of the conducting film [97]. $Q_r$ is determined by the distribution of the fields in the structure and is dominated by radiation leaking out the ends of the resonator. The loaded Q is given by

$$\frac{1}{Q_L} = \frac{1}{Q_0} + \frac{1}{Q_{ext}} \tag{C.2}$$

where $Q_{ext}$ is the external Q due to coupling to the rest of the circuit. The coplanar waveguide resonator is useful since it is easier to fabricate because the ground and signal conductors are in the same layer. The resonator is realized by coplanar waveguide gaps at each end of the half wavelength resonant portion. The external Q is set by the size of these gaps, the microwave frequency and the impedance of the resonator and input ports [98]. For a linear coplanar waveguide resonator $Q_r$ increases with decreases in the width of the center strip [99] and should not effect $Q_0$ for the $10\mu m$ wide strip . If $Q_{ext}$ and the $Q_r$ are large enough, than the resonator can be used to measure the smaller of $Q_d$ and $Q_c$. Thus the coplanar waveguide resonator is a suitable structure to study loss from the superconducting films and various dielectrics of the rf SQUID qubit.

Table C.1: Effect of Oxide Layer on Z and $\epsilon_{eff}$

| Oxide thickness (nm) | Z ($\Omega$) | $\epsilon_{eff}$ | $f_0$ (GHz) |
|---|---|---|---|
| 0 | 50.0 | 6.45 | 7.32 |
| 100 | 51.6 | 6.06 | 7.55 |
| 250 | 53.4 | 5.66 | 7.81 |
| 470 | 55.5 | 5.24 | 8.12 |

## C.1 Design and Fabrication

The coplanar waveguide resonator is designed to be of dimensions that are suitable for fabrication, within the frequency range of the sample cell and similar to that of our rf SQUID qubits. As shown in Fig. C.1 the center conductor is $s = 10\mu m$ with a $w = 6\mu m$ gap between it and the ground plane. These dimension give an impedance of approximately 50 $\Omega$ for silicon substrates. The resonant frequency of a coplanar waveguide resonator is mostly determined by the length of the resonator and the effective dielectric constant ($\epsilon_{eff}$). There are various small frequency shifts in the resonant frequency including a shift due to coupling to the external circuit. $\epsilon_{eff}$ is a property of the geometry of the coplanar structure taking into account how the electromagnetic fields are distributed between the substrate with a dielectric constant of $\epsilon_r$ and the vacuum above the substrate $\epsilon_r = 1$. There are approximate formulas [97] and compiled tables [55] that give Z and $\epsilon_{eff}$ as a function of the geometry and $\epsilon_r$. However many of the resonators used in this study have a thermal oxide layer on top the substrate directly underneath the metal films where a large percentage of the field is concentrated. Despite the films being thin, they can have a large effect on the effective dielectric constant and resonant frequency $f_0$. $\epsilon_{eff}$ can be calculated using Sonnet. Sonnet [56] is a a suite of programs that can perform electromagnetic analysis on 3-D planar structures embedded in a multilayered dielectric. Table C.1 shows $Z_0$, $\epsilon_{eff}$ and $f_0$ for different thicknesses of silicon oxide ($\epsilon_r = 3.8$) on top of a silicon substrate ($\epsilon_r = 11.9$) with $s = 10\ \mu m$, $w = 6\ \mu m$ and a resonator length of 8.063 mm.

The capacitance of the coupling gaps are calculated for the actual geometry and dielectric using Sonnet. The response data from Sonnet in the range between 1 and 20 GHz is fit with the response for a series capacitance assuming a $\pi$ model. The capacitance as a function of gap size is shown in Fig. C.2 for a coplanar waveguide geometry with $s = 10\mu m$, $w = 6\mu m$ and a silicon dielectric. Each wafer has resonators with a range of coupling gaps; $2\mu m$, $4\mu m$ and $6\mu m$. The gaps were chosen to give $Q_{ext}$ [98] large enough to measure a

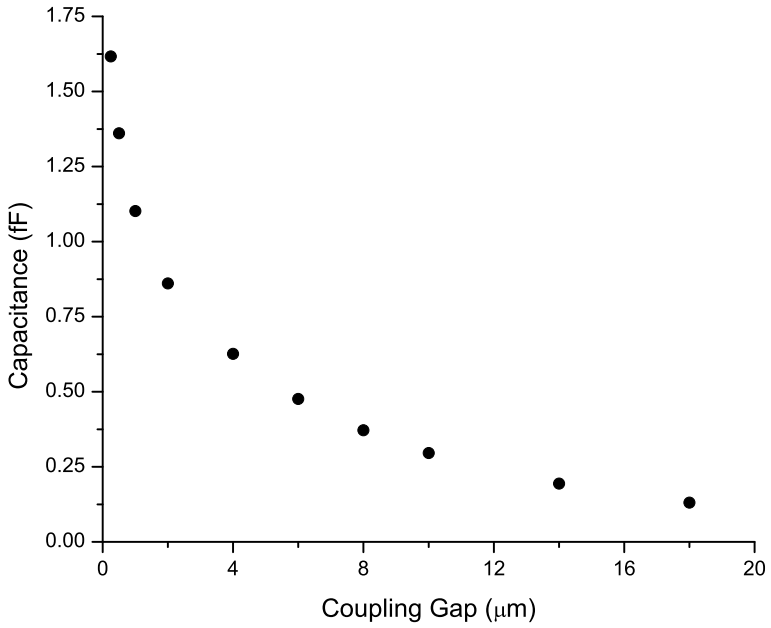


Figure C.2: Effective capacitance of a gap in the center conductor of coplanar waveguide as a function of the size of the gap with $s = 10\mu m$, $w = 6\mu m$ and a silicon dielectric.

$Q_0$ as large as $10^6$ while the gap is small enough to produce a significant transmitted signal. The coplanar waveguide was patterned using an optical mask with space for the coupling gaps to be patterned using electron beam lithography.

The changes in materials and fabrication process of the resonators are designed to focus on potential issues with the Stony Brook SAL-EBL qubit fabrication process [53]. The resistivities of the oxidized silicon substrates vary from $0.05\ \Omega - cm$ to $2.0 \times 10^4\ \Omega - cm$ to study the effect of substrate quality on loss. The Nb film deposition uses DC magnetron sputtering in Ar at a rate of 100 nm/min at a pressure of 10 mTorr and RF power of 600W. For comparison, both lift-off and reactive ion etching (RIE) are used to fabricate resonators. Two different positive photo resists, PMMA from Microchem Inc. and ZEP520A from Neon Corp, are used for the lift-off mask. A negative resist, UVN-30 from Shipley Inc., is used for the etch mask for RIE. The RIE uses a SF6 gas at a flow rate of 11.2 sccm, a pressure of 25 mTorr and an etch power of 20 W giving a etch rate of approximately 100 nm/min. The UVN-30 is then removed in Shipley Resist Remover 1165.

Resonators are also patterned from $Nb/AlO_x/Nb$ trilayers to study the effect of the additional materials and processing. First a 150 nm thick Nb

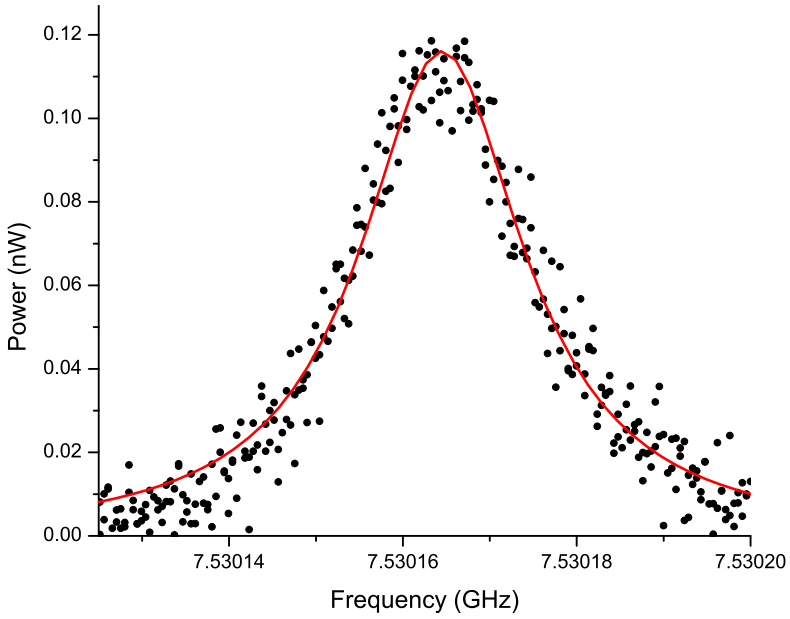


Figure C.3: Transmitted power spectrum measured at 1.2 K for a resonator made on a high resistive oxidized Si substrate. The quality factor is about $327 \times 10^3$ for a resonant frequency of 7.530165 GHz at an input power of -40 dBm.

layer is deposited. Then an 8nm thick Al film is deposited using DC magnetron sputtering at 150 W power and 5 mTorr processing pressure in Ar and oxidized in oxygen atmosphere. This followed by another 150 nm Nb layer after the chamber is pumped down to base pressure.

## C.2 Measuring the Q

The finished resonators mount inside a brass sample cell which inserts into a pumpable liquid helium cryostat capable of cooling to 1.2K. Aluminum wire bonds connect the coplanar waveguide on chip to coplanar waveguides on PC boards that are then soldered to semi-rigid Cu coaxial cables. Copper-nickel coaxial cables pass the signal to room temperature while thermally isolating the sample from the source and detector. The attenuation of the setup, dominated by the loss in the CuNi cables, is 33 dB at 7.5 GHz. A synthesized signal generator creates the microwave signal and an Agilent E4416A power meter with an Agilent 8487D power sensor measures the power transmitted through the resonator. At input powers greater then -40dBm the resonant peak shows some distortion. The $Q_c$ of the resonator is predicted to increase

with a decrease in temperature approximately proportional to $\exp(T_c/T)$ [98] below $T_c$. All experimental results shown here were measured at 1.2K.

Figure C.3 shows a typical measurement of the power transmitted though the resonator as a function of frequency. This sample was fabricated with 4 $\mu m$ coupling gaps on a high resistance silicon wafer ($2 \times 10^4 \Omega cm$) using the ZEP520A resist. The red line is a Lorentzian fit to the data with a resonant frequency of 7.530165 GHz and a Q of $327 \times 10^3$. The resonant frequency of the sample shown in Fig. C.3 is consistent with the simulations of the coplanar waveguide structure. The second harmonic is within the frequency range of the experimental apparatus and gives a quality factor consistent with the fundamental resonance. A resonator fabricated on the same wafer but with 6 $\mu m$ coupling gaps has a measured $Q = 666 \times 10^3$. The increase in measured Q when the resonator is further decoupled implies that $Q_{ext}$ is of similar magnitude to $Q_0$ and that $Q_0$ should be calculated using Equ. C.2. The calculated $Q_c$ for 6 $\mu m$ coupling gaps is $2 \times 10^6$ giving a $Q_0 = 1 \times 10^6$. For a qubit with this level of damping, the decoherence time would be hundreds of microseconds, much longer than what has been measured in qubits fabricated using a similar fabrication process (Chapter 4).

## C.3 Results

The coplanar waveguide resonators are useful for studying many of the different materials and fabrication techniques common in superconducting qubits. This section will review results of studies of the resistivity of the substrate, the effect of different resists used for liftoff and the effect of plasma etching. These aspects are not independent of each other and the results must be analyzed within the overall context of the fabrication process.

The substrate makes up a good portion of the local environment of both the coplanar waveguide resonators and superconducting qubits. They interact with the substrate, including impurities, via electric and magnetic fields. This interaction provides a mechanism of loss that can cause decoherence in a qubit and reduce the Q of the coplanar waveguide resonator. The loss of the substrate is proportional to the number of impurities and hence related to the resistivity of the substrate. Fig. C.4 shows the measured Q as function of substrate resistivity for a few different resist conditions with the black squares corresponding to the ZEP520A resist. The Q increases and hence the loss decreases with increasing resistivity. However the Q value begins to saturate when it starts to approach $Q_{ext}$. The Q was measured with the thermal oxide removed which gave a difference in the resonant frequency due to the change in $\varepsilon_{eff}$ but no difference in the Q.

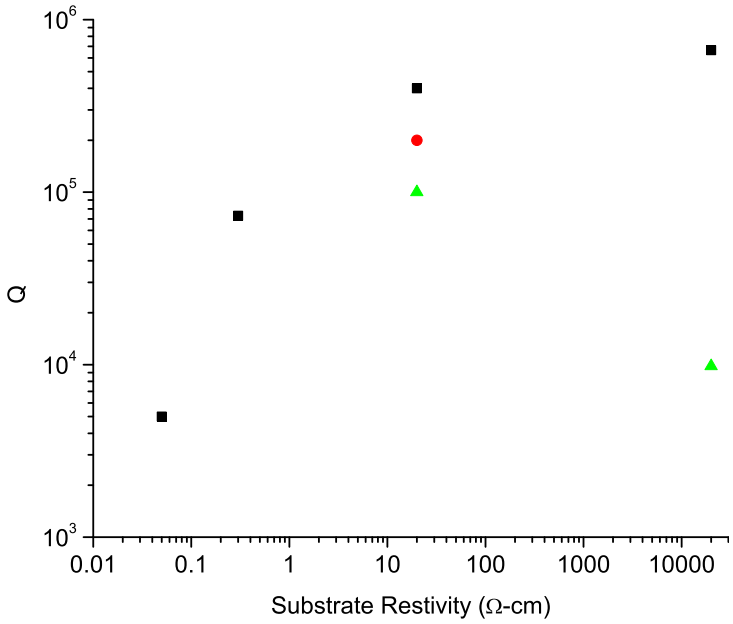


Figure C.4: Quality factors measured for resonators made on substrates of different resistivity. The quality factor is proportional to the resistivity of the substrates for resistivity less than 20 cm.

Figure C.4 also shows a Q measurement where the ZEP520A is baked at 120°C (red circles) instead of the 180°C used in previous measurements (black squares) and measurements at two different resistivities using PMMA (green triangles). The PMMA, baked at 140°C, shows the most loss of the measurements at 20 $\Omega - cm$. The cause is presumed to be outgassing of the lift-off mask during the Nb deposition when the plasma used for the deposition can heat up the resist. This is consistent with resist outgassing known to degrade deposited Nb films when PMMA is used as a lift-off mask [100–102]. The ZEP520A shows higher Q values than the PMMA and shows improvement with increased bake temperature. The increased bake temperature reduces the chance of the resist outgassing during deposition. The measured Q for the sample fabricated using PMMA on a $2.0 \times 10^4$ $\Omega - cm$ substrate is much lower than for ZEP520A on the same resistivity substrate. This is most likely due to the outgassing of the PMMA being worse on the high resistivity silicon, which has lower thermal conductivity, allowing more heat to build up in the wafer.

Our qubit fabrication process requires at least one reactive ion etch (RIE) and is based on liftoff of a $Nb/AlO_x/Nb$ trilayer instead of a single 300 nm layer of Nb. The two Nb layers of the trilayer are 300 nm thick. Table C.2 compares measured Q values of resonators from wafers processed under

Table C.2: Effect of Processing on Q

| **Sample** | Process | Nb Thickness | 4 $\mu m$ gap | 6 $\mu m$ gap |
|---|---|---|---|---|
| Single Layers | | | | |
| 1 | lift-off | 300 nm | $3.6 \times 10^5$ | $4.0 \times 10^5$ |
| 2 | etch | 300 nm | $1.0 \times 10^5$ | $3.2 \times 10^5$ |
| 3 | lift-off | 150 nm | $7.3 \times 10^4$ | $2.5 \times 10^5$ |
| 4 | etch | 150 nm | $2.5 \times 10^3$ | |
| Tri-Layers | | | | |
| 5 | lift-off | 300 nm | $1.4 \times 10^5$ | $2.5 \times 10^5$ |
| 6 | etch | 300 nm | | $2.0 \times 10^4$ |

different conditions for both 4 and 6 $\mu m$ coupling gaps. For the single layer resonators, the 150 nm thick samples show lower Qs than the 300 nm thick layers. This is possibly due to the superconducting penetration depth or surface damage making up a larger percentage of the film. The trilayer resonators compare favorably with the similarly fabricated single layer samples. Finally, the resonators defined using a RIE show consistently lower Q's than resonators defined using a liftoff which was especially the case for the 150 nm thick samples. This is consistent with earlier findings that a RIE can damage Nb films [103].

# Bibliography


[1] The international technology roadmap for semiconductors. Technical report, ITRS Working Group, 2005. URL http://public.itrs.net.

[2] Thomas J. Walls, Victor A. Sverdlov, and Konstantin K. Likharev. Nanoscale SOI MOSFETs: a comparison of two options. *Solid-State Electronics*, 48(6):857, Jun 2004.

[3] R. Cleve, A. Ekert, C. Macchiavello, and M. Mosca. Quantum algorithms revisited. *Proceedings of the Royal Society of London Sseies A*, 454:339, 1998.

[4] R. P. Feynman. Simulating physics with computers. *Ineternatoional Journal of Theoretical Physics*, 21:467, 1982.

[5] D. Deutsch. Quantum-theory, the church-turing principle and the universal quantum computer. *Proceedings of the Royal Society of London Sseies A*, 400:97, 1985.

[6] P. W. Shor. Algorithms for quantum computation: Discrete logarithms and factoring. In S. Godwasse, editor, *Proc. 35th Annual Symposium on Foundations of Computer Science*, pages 124–134, Los Alamitos, CA, 1994. IEEE Computer Society Press.

[7] Peter W. Shor. Polynomial-time algorithms for prime factorization and discrete logarithms on a quantum computer. *SIAM Journal on Computing*, 26(5):1484–1509, 1997. doi: 10.1137/S0097539795293172. URL http://link.aip.org/link/?SMJ/26/1484/1.

[8] Lov K. Grover. Quantum mechanics helps in searching for a needle in a haystack. *Phys. Rev. Lett.*, 79(2):325–328, Jul 1997. doi: 10.1103/PhysRevLett.79.325.

[9] David P. DiVincenzo. The physical implementation of quantum computation. *Fortschritte der Physik*, 48:9, 2000.

[10] Y. S. Weinstein, M. A. Pravia, E. M. Fortunato, S. Lloyd, and D. G. Cory. Implementation of the quantum fourier transform. *Phys. Rev. Lett.*, 86(9):1889–1891, Feb 2001. doi: 10.1103/PhysRevLett.86.1889.

[11] L.M.K. Vandersypen, M.Steffen, G.Breyta, C.S.Yannoni, M.H.Sherwood, and I.L. Chuang. Experimental realization of Shor's quantum factoring algorithm using nuclear magnetic resonance. *Nature*, 414:883–887, 2001.

[12] W.S. Warren. The usefulness of NMR quantum computing. *Science*, 277:1688, 1997.

[13] Dieter Suter and Kyungwon Lim. Scalable architecture for spin-based quantum computers with a single type of gate. *Phys. Rev. A*, 65(5): 052309, Apr 2002. doi: 10.1103/PhysRevA.65.052309.

[14] J. I. Cirac and P. Zoller. Quantum computations with cold trapped ions. *Phys. Rev. Lett.*, 74(20):4091–4094, May 1995. doi: 10.1103/PhysRevLett.74.4091.

[15] C. Monroe, D. M. Meekhof, B. E. King, W. M. Itano, and D. J. Wineland. Demonstration of a fundamental quantum logic gate. *Phys. Rev. Lett.*, 75(25):4714–4717, Dec 1995. doi: 10.1103/PhysRevLett.75.4714.

[16] C. Monroe. Quantum information processing with atoms and photons. *Nature*, 416:238, 2002.

[17] A quantum information science and technology roadmap part 1: Quantum computation. ARDA report, Quantum Information Science and Technology Experts Panel, April 2004. URL http://qist.lanl.gov.

[18] Michael Tinkham. *Introduction to Superconductivity*. Dover Publications, 2004.

[19] Konstantin Likharev. *Dynamics of Josephson Junctions and Circuits*. Gordon Breach Science Publishers, 1986.

[20] Jonathan R Friedman, Vijay Patel, Wei Chen, S. K Tolpygo, and James E. Lukens. Quantum superposition of distinct macroscopic states. *Nature*, 406:43–46, 2000.

[21] Richard P. Rouse. *Macroscopic Quantum Phenomenia in an rf SQUID*. PhD dissertation, Stony Brook University, Department of Physics and Astronomy, August 1996.

[22] Siyuan Han, J. Lapointe, and J. E. Lukens. Effect of a two-dimensional potential on the rate of thermally induced escape over the potential barrier. *Phys. Rev. B*, 46(10):6338–6345, Sep 1992. doi: 10.1103/PhysRevB.46.6338.

[23] S. Han, J. Lapointe, and J. E. Lukens. Thermal activation in a two-dimensional potential. *Phys. Rev. Lett.*, 63(16):1712–1715, Oct 1989. doi: 10.1103/PhysRevLett.63.1712.

[24] Jean Lapointe. *Study of barrier crossing in a macroscopic double-well potetnial*. PhD dissertation, Stony Brook University, Department of Physics and Astronomy, May 1993.

[25] R. Rouse, Siyuan Han, and J. E. Lukens. Observation of resonant tunneling between macroscopically distinct quantum levels. *Phys. Rev. Lett.*, 75(8):1614–1617, Aug 1995. doi: 10.1103/PhysRevLett.75.1614.

[26] David J. Griffiths. *Introduction to Quantum Mechanics*. Prentice Hall, 1995.

[27] J. Lapointe, R. P. Rouse, S. Y. Han, and J. E. Lukens. Energy-levels for an rf SQUID potential and their effect on the mean flux. *Physica B*, 194:1645, 1994.

[28] J. J. Sakurai. *Modern Quantum Mechanics*. Addison Wesley Longman, 1994.

[29] Michel H. Devoret, John M. Martinis, and John Clarke. Measurements of macroscopic quantum tunneling out of the zero-voltage state of a current-biased Josephson junction. *Phys. Rev. Lett.*, 55(18):1908–1911, Oct 1985. doi: 10.1103/PhysRevLett.55.1908.

[30] John M. Martinis, Michel H. Devoret, and John Clarke. Experimental tests for the quantum behavior of a macroscopic degree of freedom: The phase difference across a Josephson junction. *Phys. Rev. B*, 35(10):4682–4698, Apr 1987. doi: 10.1103/PhysRevB.35.4682.

[31] Hermann Grabert, Peter Olschowski, and Ulrich Weiss. Quantum decay rates for dissipative systems at finite temperatures. *Phys. Rev. B*, 36(4): 1931–1951, Aug 1987. doi: 10.1103/PhysRevB.36.1931.

[32] Hermann Grabert and Ulrich Weiss. Quantum tunneling rates for asymmetric double-well systems with ohmic dissipation. *Phys. Rev. Lett.*, 54 (15):1605–1608, Apr 1985. doi: 10.1103/PhysRevLett.54.1605.

[33] Paolo Silvestrini, Berardo Ruggiero, and Yuri N. Ovchinnikov. Resonant macroscopic quantum tunneling in squid systems. *Phys. Rev. B*, 54(2): 1246–1250, Jul 1996. doi: 10.1103/PhysRevB.54.1246.

[34] A. 0. Caldeira and A. J. Leggett. Quantum tunnelling in a dissapative system. *Annals of Physcis*, 149:374–456, 1983.

[35] D. V. Averin, Jonathan R. Friedman, and J. E. Lukens. Macroscopic resonant tunneling of magnetic flux. *Phys. Rev. B*, 62(17):11802–11811, Nov 2000. doi: 10.1103/PhysRevB.62.11802.

[36] C. P. Slichter. *Principles of Magnetic Resonace*. Springer-Verlag, 1978.

[37] L. Allen and J. H. Eberly. *Optical Resonance and Two-Level Atoms*. Dover Publications Inc., 1987.

[38] Karl Blum. *Density Matrix Theory and Applications*. Plenum Press, 1996.

[39] Y. Nakamura, Y.A. Pashkin, and J.S. Tsai. Coherent control of macroscopic quantum states in a single-cooper-pair box. *Nature*, 398:6730, 1999.

[40] I. Chiorescu, Y. Nakamura, C.J.P.M. Harmans, and J.E. Mooij. Coherent quantum dynamics of a superconducting flux qubit. *Science*, 299: 5614, 2003.

[41] D. Vion, A. Aassime, A. Cottet, P. Joyez, H. Pothier, C. Urbina, D. Esteve, and M.H. Devoret. Manipulating the quantum state of an electrical circuit. *Science*, 296:886, 2002.

[42] John M. Martinis, S. Nam, J. Aumentado, and C. Urbina. Rabi oscillations in a large Josephson-junction qubit. *Phys. Rev. Lett.*, 89(11): 117901, Aug 2002. doi: 10.1103/PhysRevLett.89.117901.

[43] A. Wallraff, D. I. Schuster, A. Blais, L. Frunzio, J. Majer, M. H. Devoret, S. M. Girvin, and R. J. Schoelkopf. Approaching unit visibility for control of a superconducting qubit with dispersive readout. *Physical Review Letters*, 95(6):060501, 2005. doi: 10.1103/PhysRevLett.95.060501. URL http://link.aps.org/abstract/PRL/v95/e060501.

[44] Y. Nakamura, Yu. A. Pashkin, T. Yamamoto, and J. S. Tsai. Charge echo in a cooper-pair box. *Phys. Rev. Lett.*, 88(4):047901, Jan 2002. doi: 10.1103/PhysRevLett.88.047901.

[45] D. Vion, A. Aassime, A. Cottet, P. Joyez, H. Pothier, C. Urbina, D. Esteve, and M.H. Devoret. Rabi oscillations, ramsey fringes and spin echoes in an electrical circuit. *Fortschritte der Physik*, 51(4-5):462, 2003.

[46] Y. Nakamura, Y. A. Pashkin, and J. S. Tsai. Coherent control of macroscopic quantum states in a single-cooper-pair box. *Nature.*, 398:786, 1999.

[47] C.H. van der Wal, A.C.J. ter Haar, F.K. Wilhelm, R.N. Schouten, C.J.P.M. Harmans, T.P. Orlando, S. Lloyd, and J.E. Mooij. Quantum superposition of macroscopic persistent-current states. *Science*, 290:773, 2000.

[48] K.M. Lang, S. Nam, J. Aumentado, C. Urbina, and J.M. Martinis. Banishing quasiparticles from Josephson-junction qubits: Why and how to do it. *IEEE Transactions on Applied Superconductivity*, 13:989, 2003.

[49] R. W. Simmonds, K. M. Lang, D. A. Hite, S. Nam, D. P. Pappas, and John M. Martinis. Decoherence in Josephson phase qubits from junction resonators. *Physical Review Letters*, 93(7):077003, 2004. doi: 10.1103/PhysRevLett.93.077003. URL http://link.aps.org/abstract/PRL/v93/e077003.

[50] V Patel and JE Lukens. Self-shunted $Nb/AlO_x/Nb$ Josephson junctions. *IEEE Transactions Applied Superconductivity*, 9:3247–3250, 1999.

[51] D. Nakada, K.K. Berggren, E. Macedo, V. Liberman, and T.P. Orlando. Improved critical-current-density uniformity by using anodization. *IEEE Transactions on Applied Superconductivity*, 13:111, 2003.

[52] Wei Chen, Vijay Patel, and James E. Lukens. Fabrication of high-quality Josephson junctions for quantum computation using a self-aligned process. *Microelectronic Engineering*, 73-74:767, 2004.

[53] Vijay Patel, Wei Chen, Shawn Pottorf, and James E. Lukens. A fast turn-around time process for fabrication of qubit circuits. *IEEE Transactions on Apllied Superconductivity*, 15:117, 2005.

[54] M.M. Khapaev, A.Yu. Kidiyarova-Shevchenko, P. Magnelind, and M.Yu. Kupriyanov. 3D-MLSI: software package for inductance calculation in multilayer superconducting integrated circuits. In *IEEE Transactions on Apllied Superconductivity*, pages 1090–1093, 2001.

[55] K.C. Gupta, Ramesh Garg, and I.J. Bahl. *Microstrip Lines and Slotlines*. Artech House Inc., 1979.

[56] James C. Rautio. Application of electromagnetic analysis software to 3-d planar high frequency design. In *International Multilayer Circuits Symposium*, pages B2–1–B2–17, March 1999.

[57] James C. Rautio. A conformal mesh for efficient planar electromagnetic analysis. In *IEEE Transactions on Microwave Theory and Techniques*, volume 52, pages 257–264, January 2004.

[58] Henry W. Ott. *Noise Reduction Techniques in Electronic Systems*. Wiley Interscience, 1988.

[59] Ralph Morrison. *Groundin and Shielding Techniques*. Wiley Interscience, 1998.

[60] Low noise precision difet operational amplifier. Technical report, Burr-Brown, 1984.

[61] Jeffery Cain. Parasitic inductance of multilayer ceramic capacitors. Technical report, AVX Corporation.

[62] T. Kutsuzawa, H. Tanaka, S. Saito, H. Nakano, K. Semba, and H. Takayanagi. *Applied Physics Letters*, 87:073501, 2005.

[63] Mixer application information. Technical report, WJ Communications.

[64] A. Lupascu, C. J. M. Verwijs, R. N. Schouten, C. J. P. M. Harmans, and J. E. Mooij. Nondestructive readout for a superconducting flux qubit. *Physical Review Letters*, 93(17):177006, 2004. doi: 10.1103/PhysRevLett.93.177006. URL http://link.aps.org/abstract/PRL/v93/e177006.

[65] Theodore Van Duzer and Charles W. Turner. *Principles of Superconductive Devices and Circuits*. Prentice Hall, 1999.

[66] Antonio Barone and Gianfranco Paternò. *Physics and Applications of the Josephson Effect*. John Wiley and Sons, 1982.

[67] Matthias Steffen, M. Ansmann, R. McDermott, N. Katz, Radoslaw C. Bialczak, Erik Lucero, Matthew Neeley, E. M. Weig, A. N. Cleland, and John M. Martinis. State tomography of capacitively shunted phase qubits with high fidelity. *Physical Review Letters*, 97(5):050502, 2006.

doi: 10.1103/PhysRevLett.97.050502. URL http://link.aps.org/abstract/PRL/v97/e050502.

[68] K. B. Cooper, Matthias Steffen, R. McDermott, R. W. Simmonds, Seongshik Oh, D. A. Hite, D. P. Pappas, and John M. Martinis. Observation of quantum oscillations between a Josephson phase qubit and a microscopic resonator using fast readout. *Physical Review Letters*, 93(18):180401, 2004. doi: 10.1103/PhysRevLett.93.180401. URL http://link.aps.org/abstract/PRL/v93/e180401.

[69] J. Claudon, F. Balestro, F. W. J. Hekking, and O. Buisson. Coherent oscillations in a superconducting multilevel quantum system. *Physical Review Letters*, 93(18):187003, 2004. doi: 10.1103/PhysRevLett.93.187003. URL http://link.aps.org/abstract/PRL/v93/e187003.

[70] H. A. Kramers. Brownian motion in a field of force and the diffusion model of chemical reactions. *Physica*, 7:284, 1940.

[71] H. Paik, B. K. Cooper, S. K. Dutta, R. M. Lewis, R. C. Ramos, T. A. Palomaki, A. J. Przybysz, A. J. Dragt, J. R. Anderson, C. J. Lobb, and F. C. Wellstood. Measurements of decoherence in three dc squid phase qubits. *IEEE Transactions on Applied Superconductivity*, 17(2):120–123, June 2007. ISSN 1051-8223. doi: 10.1109/TASC.2007.898124.

[72] John M. Martinis, K. B. Cooper, R. McDermott, Matthias Steffen, Markus Ansmann, K. D. Osborn, K. Cicak, Seongshik Oh, D. P. Pappas, R. W. Simmonds, and Clare C. Yu. Decoherence in Josephson qubits from dielectric loss. *Physical Review Letters*, 95(21):210503, 2005. doi: 10.1103/PhysRevLett.95.210503. URL http://link.aps.org/abstract/PRL/v95/e210503.

[73] T.A. Palomaki, S. K. Dutta, R. M. Lewis, A. J. Przybysz, Hanhee Paik, B. K. Cooper, H. Kwon, E. Tiesinga, A. J. Dragt, J. R. Anerson, C. J. Lobb, and F. C. Wellstood. Evidence of microstates in dc SQUID phase qubits. In *Extended Abstatracts of the 11th International Superconductive Electronics Conference*, 2007.

[74] Philip R. Johnson, William T. Parsons, Frederick W. Strauch, J. R. Anderson, Alex J. Dragt, C. J. Lobb, and F. C. Wellstood. Macroscopic tunnel splittings in superconducting phase qubits. *Physical Review Letters*, 94(18):187004, 2005. doi: 10.1103/PhysRevLett.94.187004. URL http://link.aps.org/abstract/PRL/v94/e187004.

[75] Michael Nielsen and Isaac Chuang. *Quantum Computation and Quantum Information*. Cambridge Press, 2000.

[76] G. Ithier, E. Collin, P. Joyez, P. J. Meeson, D. Vion, D. Esteve, F. Chiarello, A. Shnirman, Y. Makhlin, J. Schriefl, and G. Schön. Decoherence in a superconducting quantum bit circuit. *Physical Review B (Condensed Matter and Materials Physics)*, 72(13):134519, 2005. doi: 10.1103/PhysRevB.72.134519. URL http://link.aps.org/abstract/PRB/v72/e134519.

[77] Claude Cohen-Tannoudji, Jacques Dupont-Roc, and Gilbert Grynberg. *Atom-Photon Interactions*. John Wiley and Sons Inc., 1992.

[78] L. Longobardi, S. Pottorf, V. Patel, and J. E. Lukens. Development and testing of a persistent flux bias for qubits. *IEEE Transactions on Applied Superconductivity*, 17:88, 2007.

[79] V. Foglieitti, W.J. Gallagher, M.B. Ketchen, A.W. Kleinsasser, R.H. Koch, S.I. Raider, and R.L. Sandstrom. Low-frequency noise in low 1/f noise dc SQUIDs. *Applied Physics Letters*, 49:1393, 1986.

[80] C. Tesche, K. Brown, A. Callegari, M. Chen, J. Greiner, H. Jones, M. Ketchen, K. Kim, A. Kleinsasser, H. Notarys, G. Proto, R. Wang, and T. Yogi. Practical dc SQUIDs with extremely low 1/f noise. *IEEE Transactions on Magnetics*, 21:1032, 1985.

[81] F.C. Wellstood, C. Urbina, and J. Clarke. Low-frequency noise in dc superconducting quantum interference devices below 1-K. *Applied Physics Letters*, 50:772, 1987.

[82] F. Yoshihara, K. Harrabi, A. O. Niskanen, Y. Nakamura, and J. S. Tsai. Decoherence of flux qubits due to 1/f flux noise, June 2006.

[83] Shawn Pottorf, Vijay Paterl, and J. E. Lukens. $Nb/AlO_x/Nb$ junction quality measurments for flux qubits. Poster presented at 11 th International Superconductive Electronics Conference, June 2007.

[84] D. J. Van Harlingen, T. L. Robertson, B. L. T. Plourde, P. A. Reichardt, T. A. Crane, and John Clarke. Decoherence in Josephson-junction qubits due to critical-current fluctuations. *Physical Review B (Condensed Matter and Materials Physics)*, 70(6):064517, 2004. doi: 10.1103/PhysRevB.70.064517. URL http://link.aps.org/abstract/PRB/v70/e064517.

[85] Roger H. Koch, David P. DiVincenzo, and John Clarke. Model for l/f flux noise in SQUIDs and qubits, 2007. URL http://arXiv.org/abs/cond-mat/0702025.

[86] Rogerio de Sousa. Dangling-bond spin relaxation and magnetic 1/f noise from the amorphous semiconductor interface, 2007. URL http://arxiv.org/abs/0705.4088.

[87] P. Bertet, I. Chiorescu, G. Burkard, K. Semba, C. J. P. M. Harmans, D. P. DiVincenzo, and J. E. Mooij. Dephasing of a superconducting qubit induced by photon noise. *Physical Review Letters*, 95(25):257002, 2005. doi: 10.1103/PhysRevLett.95.257002. URL http://link.aps.org/abstract/PRL/v95/e257002.

[88] Valérie Lefevre-Seguin, Emmanuel Turlot, Cristian Urbina, Daniel Esteve, and Michel H. Devoret. Thermal activation of a hysteretic dc superconducting quantum interference device from its different zero-voltage states. *Phys. Rev. B*, 46(9):5507–5522, Sep 1992. doi: 10.1103/PhysRevB.46.5507.

[89] J. Männik, S. Li, W. Qiu, W. Chen, V. Patel, S. Han, and J. E. Lukens. Crossover from Kramers to phase-diffusion switching in moderately damped Josephson junctions. *Physical Review B (Condensed Matter and Materials Physics)*, 71(22):220509, 2005. doi: 10.1103/PhysRevB.71.220509. URL http://link.aps.org/abstract/PRB/v71/e220509.

[90] C. D. Tesche and J. Clarke. dc SQUID: Noise and optimization. *Journal of Low Temp. Phys.*, 29:301, 1977.

[91] D. B. Schwartz, B. Sen, C. N. Archie, and J. E. Lukens. Quantitative study of the effect of the environment on macroscopic quantum tunneling. *Phys. Rev. Lett.*, 55(15):1547–1550, Oct 1985. doi: 10.1103/PhysRevLett.55.1547.

[92] Chip monolithic ceramic capacitors catalog. Technical report, Murata Manufacturing Company, 2001.

[93] Simon Ramo, John R. Whinnery, and Theodore Van Duzer. *John Wiley and Sons*. Fiels and Waves in Communication Electronics, 1994.

[94] K. Bladh, D. Gunnarsson, E. Hurfeld, S. Devi, C. Kristoffersson, B. Smalander, S. Pehrson, T. Claeson, P. Delsing, and M. Taslakov. *Reviews of Scientific Instruments*, 74:1323, 2003.

[95] Akio Fukushima, Akira Sato, Akio Iwasa, Yasuhiro Nakamura, Takeshi Komatsuzkai, and Yasuhiko Sakamoto. *IEEE Transactions on Instrumentation and Measurement*, 46:289, 1997.

[96] A. B. Zorin. *Reviews of Scientific Instruments*, 66:4296, 1995.

[97] Hoton How, Randall G. Seed, C. Vittoria, D. B. Chrisey, J. S. Horwitz, C. Corosella, and V. Folen. Microwave characteristics of high $T_c$ superconducting coplanar waveguide resonator. *IEEE Transactions on Microwave Theory and Techniques*, 40:1668, 1992.

[98] Luigi Frunzio, Andreas Wallraff, David Schuster, Johannes Majer, and Robert Schoelkopf. Fabrication and characterization of superconducting circuit qed devices for quantum computation. *IEEE Transactions on Apllied Superconductivity*, 15:860, 2005.

[99] Xiangying Wu and Ikuo Awai. Numerical and experimental investigation on quality factors of coplanar waveguide resonators. *IEICE Transactions on Electronics E Series C*, 83:1923, 2000.

[100] N. Kim et al. Fabrication of Nb-based superconducting single electron transistor. *Physica B-Condensed Matter*, 329:1519, 2003.

[101] P. Dubos et al. Thermostable trilayer resist for niobium lift-off. *Journal of Vacuum Science and Technology B*, 18:122, 2000.

[102] T. Hoss, C. Strunk, and C. Schonenberger. Nonorganic evaporation mask for superconducting nanodevices. *Microelectronic Engineering*, 46:149, 1999.

[103] W. Chen et al. Development toward high-speed integrated circuits and SQUID qubits with $Nb/AlO_x/Nb$ Josephson junctions. *IEEE Transactions on Applied Superconductivity*, 13:103, 2003.